SOME APPLICATIONS OF THE GENERALIZED MULTISCALE FINITE ELEMENT METHOD

A Dissertation

by

SHUBIN FU

Submitted to the Office of Graduate and Professional Studies of
Texas A&M University
in partial fulfillment of the requirements for the degree of

DOCTOR OF PHILOSOPHY

Chair of Committee,	Yalchin Efendiev
Co-Chair of Committee,	Richard Gibson Jr.
Committee Members,	Raytcho Lazarov
	Jianxin Zhou
Head of Department,	Emil Straube

August 2017

Major Subject: Mathematics

ABSTRACT

Many materials in nature are highly heterogeneous and their properties can vary at different scales. Direct numerical simulations in such multiscale media are prohibitively expensive and some types of model reduction are needed. Typical model reduction techniques include upscaling and multiscale methods. In upscaling methods, one upscales the multiscale media properties so that the problem can be solved on a coarse grid. In multiscale method, one constructs multiscale basis functions that capture media information and solves the problem on the coarse grid.

Generalized Multiscale Finite Element Method (GMsFEM) is a recently proposed model reduction technique and has been used for various practical applications. This method has no assumption about the media properties, which can have any type of complicated structure. In GMsFEM, we first create a snapshot space, and then solve a carefully chosen eigenvalue problem to form the offline space. One can also construct online space for the parameter dependent problems. It is shown theoretically and numerically that the GMsFEM is very efficient for the heterogeneous problems involving high-contrast, no-scale separation.

In this dissertation, we apply the GMsFEM to perform model reduction for the steady state elasticity equations in highly heterogeneous media though some of our applications are motivated by elastic wave propagation in subsurface. We will consider three kinds of coupling mechanism for different situations. For more practical purposes, we will also study the applications of the GMsFEM for the frequency domain acoustic wave equation and the Reverse Time Migration (RTM) based on the time domain acoustic wave equation.

DEDICATION

To my parents

ACKNOWLEDGMENTS

First of all, I would like to express my deepest gratitude to my supervisor Dr. Yalchin Efendiev, who guides me patiently, encourages me constantly, and supports me financially. I am grateful to him for the chance of participating in his wonderful research projects, which makes this work possible. I must thank all the unique opportunities he provided me with, such as attending AMS and SEG annual meetings and research visits. Without him, I can not arrive at this point.

I am also very thankful to Dr. Rick Gibson, who serves as my co-advisor, provides me much useful background in Geophysics related to my research and wrote reference letters.

I am really grateful to Dr. Eric Chung, for his generous support for my visits to the Chinese University of Hong Kong during my graduate study. The discussions with him help me a lot in academic development. Moreover, I want to thank Dr. Raytcho Lazarov and Dr. Jianxin Zhou for taking time serving on my dissertation committee.

I also appreciate the Department of Mathematics for providing me the amazing opportunity to study here and the continuous financial support. I intend to thank my friends and fellow students for inspiring and encouraging me in the past 6 years.

Last but not least, I want to thank my parents and brother for the unconditional love they have been giving me all these years. That always incents me to strive towards my goal.

CONTRIBUTORS AND FUNDING SOURCES

Contributors

This work was supported by a thesis committee consisting of my advisor Professor Yalchin Efendiev and Professors Raytcho Lazarov, Jianxin Zhou of the Department of Mathematics and my co-advisor Professor Richard Gibson Jr. of the Department of Geology and Geophysics.

The research for Chapter II was conducted in part by Professor Yalchin Efendiev and Eric Chung and was published in 2014 in the Journal Int J Geomath.

The research for Chapter V was conducted in part by Professor Richard Gibson Jr. and was published in 2015 in the Proceedings of the 2015 SEG Annual Meeting.

The research for Chapter IV was conducted in part by Dr. Kai Gao and was published in 2015 in the Proceedings of the 2015 SEG Annual Meeting.

All other work conducted for the thesis was completed by the student independently.

Funding Sources

Graduate study was supported by a scholarship from Texas A&M University and Professor Yalchin's grant from U.S. Department of Energy Office of Science, Office of Advanced Scientific Computing Research, Applied Mathematics program under Award Number DE-FG02-13ER26165.

TABLE OF CONTENTS

Page

LIST OF FIGURES

FIGURE Page

LIST OF TABLES

I. INTRODUCTION

I.1 Motivation

Many science and engineering problems encounter heterogeneous media with multiple scales and high-contrast, e.g., wave propagation in heterogeneous subsurface, modeling of composite materials, and flows in porous media. In practical simulations, one cannot ignore the small scale features because they can affect the macroscopic response of the problems. However, it can be prohibitively expensive to resolve all the scales in these problems and therefore some types of model reduction techniques are needed.

Typically, there are two types of model reduction techniques: upscaling and multiscale methods. Upscaling approaches such as homogenization and numerical homogenization [69, 3, 87, 35, 22, 34, 1, 73, 20, 41, 67, 80, 59] have been routinely used to model macroscopic properties and macroscopic behaviors of media. These approaches compute the effective media properties based on representative volume simulations. These properties are further used to solve macroscale equations. However, upscaling is limited by the assumption on media properties (e.g. periodicity) and the geometry of the problems studied. Another direction is the multiscale method which was extensively investigated in the past two decades. These methods include variational multiscale method [53, 54], multiscale finite element method [33, 37, 5], mixed multiscale finite element method [23], the multiscale finite volume method [55], mortar multiscale finite element method [85, 84, 6], multiscale hybrid-mixed finite element methods [4, 49], the heterogeneous multiscale methods [83, 2]. However, like the upscaling techniques, all these methods have very strict requirements about the media properties.

In 2013, Efendiev et al. proposed the generalized multiscale finite element methods (GMsFEM) [36], which is a generalization of the multiscale finite element method by en-

riching local basis function space. The initial version of GMsFEM can also be viewed as a type of the generalized finite element method (GFEM) [10] since the basis functions are also the products of shape functions and the partition of unity functions [9]. Therefore, this method was instantly extended to other scenarios, like the DG-GMsFEM [28, 43], the mixed GMsFEM [27] and the HDG-GMsFEM [38]. The construction of multiscale basis functions in GMsFEM consists of three stages: the snapshot space, the offline space, and the online stage. The core part of the GMsFEM is the design of appropriate spectral problems that can yield accurate eigenfunctions to obtain a good reduced coarse system. The coarse space enriched by eigenfunctions renders GMsFEM to yield solutions with a significantly improved accuracy for a more general class of problems (e.g. media properties without scale separation) with a slightly increased computational cost.

The GMsFEM was initially introduced to solve second-order elliptic type of high-contrast flow problems, the applications of the GMsFEM for other partial differential equations are reported in [26, 27, 30, 43, 21, 29]. The goal of this dissertation is to study the application of GMsFEM for static linear elasticity equations, frequency domain acoustic equation and the reverse time migration (RTM) based on the time domain acoustic equation. The organization of this dissertation is as follows. In Chapter II, we first study the GMsFEM for second-order static elasticity equations in highly heterogeneous media, we will discuss the construction of snapshot and offline space for both the continuous Galerkin and discontinuous Galerkin. We will also study the effects of oversampling. Convergence analysis will be provided. The hybridizable discontinuous Galerkin GMsFEM (HDG-GMsFEM) for the first-order linear elasticity system will be discussed in Chapter III. We will introduce three ways of constructing the edge-based multiscale basis. Comprehensive numerical study of these methods along with the oversampling, randomized snapshot techniques will be presented, we will also show the performance of applying HDG-GMsFEM for the nearly incompressible elasticity problem. In Chapter IV, we consider the appli-

cation of GMsFEM for the Helmholtz equations, we will show that the eigenfunctions are better than the polynomial functions in reducing the dispersion error. In Chapter V, we develop a fast RTM algorithm with GMsFEM. A brief introduction to each chapter is provided.

I.2 Outline of the dissertation

In Chapter II, we design a multiscale model reduction techniques using GMsFEM for steady state elasticity equation in heterogeneous media

$$\frac{\partial}{\partial x_i}(c_{ijkl}(x)e_{kl}(u)) = f_j(x), \tag{I.1}$$

where $e_{kl}(u) = \frac{1}{2}(\frac{\partial u_k}{\partial x_l} + \frac{\partial u_l}{\partial x_k})$ and $c_{ijkl}(x)$ is a multiscale field with a high contrast. In particular, we design (1) a snapshot space (2) an offline space for each coarse patch. The offline space consists of multiscale basis functions that are coupled in a global formulation. We will consider several choices for snapshot spaces, offline spaces, and global coupling. The main idea of the snapshot space in each coarse patch is to provide an exhaustive space where an appropriate spectral decomposition is performed. This space contains local functions that can mimic the global solution behavior in the coarse patch for all right hand sides or boundary conditions. We consider two choices for the snapshot space. The first one consists of all fine-grid functions in each coarse patch and the second one consists of harmonic extensions. Next, we propose a local spectral decomposition in the snapshot space which allows selecting multiscale basis functions. This local spectral decomposition is based on the analysis and depends on the global coupling mechanisms. We consider several choices for the local spectral decomposition including oversampling approach where larger domains are used in the eigenvalue problem. The oversampling technique uses larger domains to compute snapshot vectors that are more consistent with local solution space and thus can have much lower dimensions.

To couple multiscale basis functions constructed in the offline space, we consider two methods, conforming Galerkin (CG) approach and discontinuous Galerkin (DG) approach based on symmetric interior penalty method for (I.1). These approaches are studied for linear elliptic equations in [36]. Both approaches provide a global coupling for multiscale basis functions where the solution is sought in the space spanned by these multiscale basis functions. This representation allows approximating the solution with a reduced number of degrees of freedom. The constructions of the basis functions are different for continuous Galerkin and discontinuous Galerkin methods as the local spectral decomposition relies on the analysis. In particular, for continuous Galerkin approach, we use partition of unity functions and discuss several choices for partition of unity functions. We provide an analysis of both approaches. The offline space construction is based on the analysis.

We present numerical results where we study the convergence of continuous and discontinuous Galerkin methods using various snapshot spaces as well as with and without the use of oversampling. We consider highly heterogeneous coefficients that contain high contrast. Our numerical results show that the proposed approaches allow approximating the solution accurately with fewer degrees of freedom. In particular, when using the snapshot space consisting of harmonic extension functions, we obtain better convergence results. In addition, oversampling methods and the use of snapshot spaces constructed in the oversampled domains can substantially improve the convergence.

The Chapter III is devoted to design multiscale model reduction methods for the first-order formulation of the linear elasticity equation. The benefit of approximating the mixed formulation of elasticity equation is it can deal with nearly incompressible materials and preserve energy and mass conservation. We will study the GMsFEM within the framework of hybridizable discontinuous Galerkin (HDG), which allows decomposing the entire problem into a small dimension global problem defined on the coarse grid interfaces and several local problems. The multiscale basis function is supported in coarse edges and we

will construct three types multiscale spaces for the edge-based trace space to yield a much reduced stable coarse system. The efficiency of the proposed methods is demonstrated on a set of numerical experiments for high-contrast media. We are particular interested in the the convergence behavior of the multiscale solution with more basis added, the effects of applying oversampling randomized snapshot techniques, and the media contrast. We will also show the results of applying our methods for the nearly incompressible material.

In Chapter IV, we discuss GMsFEM for the Helmholtz equation in media with variable mass density. Traditional numerical methods for Helmholtz equation like finite-difference methods (FDM) [75, 70, 68, 24, 25, 60, 61], finite-element methods (FEM) [48] will lead to a huge dimension ill conditioned non-positive definite system and thus extremely hard to solve. In [10, 9], Babuška proposed the GFEM for the Helmholtz equation, which uses the products of partition of unity functions and the polynomial or trigonometric functions to form the finite element space. This method shows better accuracy and solvability than the conventional method. However, to our knowledge, it is only suitable for the homogeneous media since the basis functions they use depend on the fixed wavenumber. We will consider using the eigenfunctions from local spectral problem to form the finite element space defined on coarse grid, which enables us to accurately solve the Helmholtz equation without directly touching the large discrete system formed on the fine mesh. We will design adaptive GMsFEM based on the velocity distribution of the media to sample different numbers of basis functions for different local basis space. Numerical tests on both homogeneous and heterogeneous media show using eigenfunctions is much better than the polynomials in terms of accuracy and resistance to the numerical dispersion.

In Chapter V, we consider the GMsFEM for the RTM, a seismic imaging method that heavily relies on repeatedly solving wave equation with different sources. Wave equation migration methods provide accurate and detailed subsurface images by incorporating the influence of complex wave arrivals and features that are not included in solutions based

on ray theory. However, the computational cost of these methods is significant. In [28], the GMsFEM was proved to be an efficient solver for the acoustic equation. Based on this research, we further explore the application of GMsFEM for the RTM that based on the acoustic wave equation. The basis functions are computed only once for an earth model and are used for all source positions. Applications to a test model show that the multiscale RTM produces accurate images with a significant reduction in computation time. Using fewer basis functions provides faster results, though additional numerical artifacts may result. However, the results still capture the spatial structure in images, so this is useful when testing various velocity models because many trial velocities can be tested in much less computational time.

II. GENERALIZED MULTISCALE FINITE ELEMENT METHODS FOR SECOND-ORDER LINEAR ELASTICITY EQUATIONS *

II.1 Introduction

In this chapter, we discuss the application of GMsFEM to elasticity equation in heterogeneous media. We consider steady state elasticity equations though some of our applications are motivated by elastic wave propagation in subsurface where the subsurface properties can be highly heterogeneous and have high contrast. We present the construction of main ingredients for GMsFEM such as the snapshot space and offline spaces. The latter is constructed using local spectral decomposition in the snapshot space. The spectral decomposition is based on the analysis which is provided in the chapter. We consider both continuous Galerkin and discontinuous Galerkin coupling of basis functions. Both approaches have their strengths and weaknesses. Continuous Galerkin methods allow avoiding penalty parameters though they involve partition of unity functions which can alter the properties of multiscale basis functions. On the other hand, discontinuous Galerkin techniques allow gluing multiscale basis functions without any modification. Because basis functions are constructed independently from each other, this approach provides an advantage. We discuss the use of oversampling techniques that use snapshots in larger regions to construct the offline space. We provide numerical results to show that one can accurately approximate the solution using reduced number of degrees of freedom.

The chapter is organized as follows. In Section II.2, we state the problem and the notations for coarse and fine grids. In Section II.3, we give the construction of multiscale basis functions, snapshot spaces and offline spaces, as well as global coupling via CG and

*This chapter is reprinted with permission from "Generalized multiscale finite element method for elasticity equations" by Chung, Eric T., Yalchin Efendiev, and Shubin Fu, 2014. GEM-International Journal on Geomathematics, 5(2), pp.225-254. Copyright [2017] by Springer.

DG. In Section II.4, we present numerical results. Sections II.5-II.6 are devoted to the analysis of the methods.

II.2 Preliminaries

In this section, we will present the general framework of GMsFEM for linear elasticity in high-contrast media. Let $D \subset \mathbb{R}^2$ (or $\mathbb{R}^3$) be a bounded domain representing the elastic body of interest, and let $u = (u_1, u_2)$ be the displacement field. The strain tensor $\epsilon(u) = (\epsilon_{ij}(u))_{1\leq i,j\leq 2}$ is defined by

$$\epsilon(u) = \frac{1}{2}(\nabla u + \nabla u^T),$$

where $\nabla u = (\frac{\partial u_i}{\partial x_j})_{1\leq i,j\leq 2}$. In the component form, we have

$$\epsilon_{ij}(u) = \frac{1}{2}\Big(\frac{\partial u_i}{\partial x_j} + \frac{\partial u_j}{\partial x_i}\Big), \quad 1 \leq i, j \leq 2.$$

In this dissertation, we assume the medium is isotropic. Thus, the stress tensor $\sigma(u) = (\sigma_{ij}(u))_{1\leq i,j\leq 2}$ is related to the strain tensor $\epsilon(u)$ in the following way

$$\sigma = 2\mu\epsilon + \lambda\nabla \cdot u\, I,$$

where $\lambda > 0$ and $\mu > 0$ are the Lamé coefficients. We assume that λ and μ have highly heterogeneous spatial variations with high contrasts. Given a forcing term $f = (f_1, f_2)$, the displacement field u satisfies the following

$$-\nabla \cdot \sigma = f, \quad \text{in } D \tag{II.1}$$

or in component form

$$-\Big(\frac{\partial \sigma_{i1}}{\partial x_1}+\frac{\partial \sigma_{i2}}{\partial x_2}\Big)=f_i, \quad \text{in } D, \quad i=1,2. \tag{II.2}$$

For simplicity, we will consider the homogeneous Dirichlet boundary condition $u=0$ on ∂D.

Let $\mathcal{T}^H$ be a standard triangulation of the domain D where $H>0$ is the mesh size. We call $\mathcal{T}^H$ the coarse grid and H the coarse mesh size. Elements of $\mathcal{T}^H$ are called coarse grid blocks. The set of all coarse grid edges is denoted by $\mathcal{E}^H$ and the set of all coarse grid nodes is denoted by $\mathcal{S}^H$. We also use N_S to denote the number of coarse grid nodes, N to denote the number of coarse grid blocks. In addition, we let $\mathcal{T}^h$ be a conforming refinement of the triangulation $\mathcal{T}^H$. We call $\mathcal{T}^h$ the fine grid and $h>0$ is the fine mesh size. We remark that the use of the conforming refinement is only to simplify the discussion of the methodology and is not a restriction of the method.

Let V^h be a finite element space defined on the fine grid. The fine-grid solution u_h can be obtained as

$$a(u_h,v)=(f,v), \quad \forall v\in V^h, \tag{II.3}$$

where

$$a(u,v)=\int_D \Big(2\mu\epsilon(u):\epsilon(v)+\lambda\nabla\cdot u\,\nabla\cdot v\Big)\,dx, \quad (f,v)=\int_D f\cdot v\,dx \tag{II.4}$$

and

$$\epsilon(u):\epsilon(v)=\sum_{i,j=1}^{2}\epsilon_{ij}(u)\epsilon_{ij}(v), \quad f\cdot v=\sum_{i=1}^{2}f_i v_i. \tag{II.5}$$

Now, we present GMsFEM. The discussion consists of two main steps, namely, the construction of local basis functions and the global coupling. In this chapter, we will de-

velop and analyze two types of global coupling, namely, the continuous Galerkin coupling and the discontinuous Galerkin coupling. These two couplings will require two types of local basis functions. In essence, the CG coupling will need vertex-based local basis functions and the DG coupling will need element-based local basis functions.

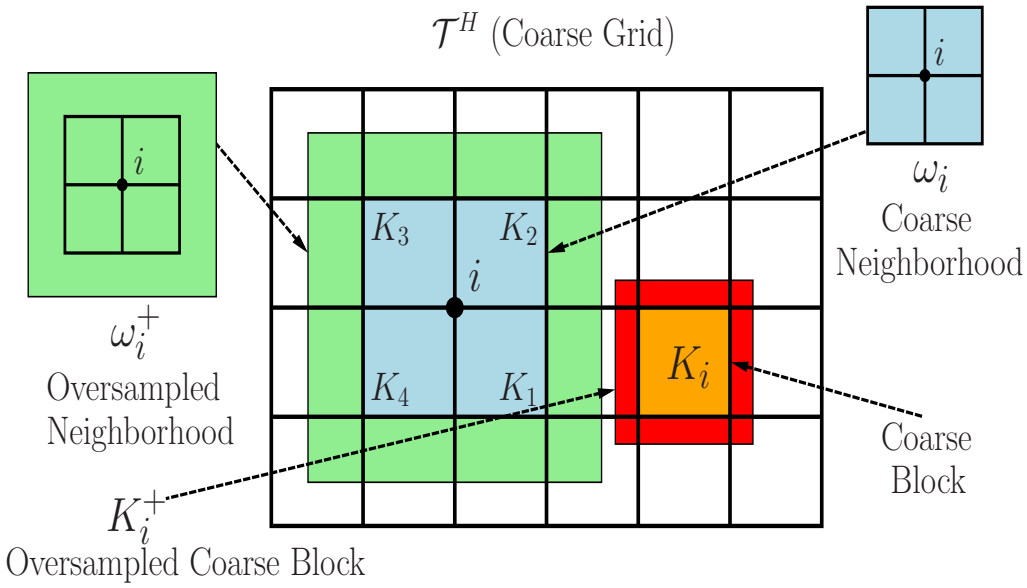

Figure II.1: Illustration of a coarse neighborhood, oversampled coarse neighborhood, coarse block and oversampled coarse block.

For each vertex $x_i \in \mathcal{S}^H$ in the coarse grid, we define the coarse neighborhood ω_i by

$$\omega_i = \bigcup \{K_j \ : \ K_j \subset \mathcal{T}^H, \ x_i \in K_j\}.$$

That is, ω_i is the union of all coarse grid blocks K_j having the vertex x_i (see Figure II.1). A snapshot space $V^{i,\text{snap}}$ is constructed for each coarse neighborhood ω_i. The snapshot space contains a large set that represents the local solution space. A spectral problem is then constructed to get a reduced dimensional space. Specifically, the spectral problem

is solved in the snapshot space and eigenfunctions corresponding to dominant modes are used as the final basis functions. To obtain conforming basis functions, each of these selected modes will be multiplied by a partition of unity function. The resulting space is denoted by $V^{i,\text{off}}$, which is called the offline space for the i-th coarse neighborhood ω_i. The global offline space V^{off} is then defined as the linear span of all these $V^{i,\text{off}}$, for $i = 1, 2, \cdots, N_S$. The CG coupling can be formulated as to find $u_H^{\text{CG}} \in V^{\text{off}}$ such that

$$a(u_H^{\text{CG}}, v) = (f, v), \quad \forall v \in V^{\text{off}}. \tag{II.6}$$

The DG coupling can be constructed in a similar fashion. A snapshot space $V^{i,\text{snap}}$ is constructed for each coarse grid block K_i. A spectral problem is then solved in the snapshot space and eigenfunctions corresponding to dominant modes are used as the final basis functions. This space is called the offline space $V^{i,\text{off}}$ for the i-th coarse grid block. The global offline space V^{off} is then defined as the linear span of all these $V^{i,\text{off}}$, for $i = 1, 2, \cdots, N$. The DG coupling can be formulated as: find $u_H^{\text{DG}} \in V^{\text{off}}$ such that

$$a_{\text{DG}}(u_H^{\text{DG}}, v) = (f, v), \quad \forall v \in V^{\text{off}}, \tag{II.7}$$

where the bilinear form a_{DG} is defined as

$$\begin{aligned} a_{\text{DG}}(u, v) =& a_H(u, v) - \sum_{E \in \mathcal{E}^H} \int_E \Big(\{\sigma(u)\, n_E\} \cdot [\![v]\!] + \{\sigma(v)\, n_E\} \cdot [\![u]\!] \Big)\, ds \\ &+ \sum_{E \in \mathcal{E}^H} \frac{\gamma}{h} \int_E \{\lambda + 2\mu\} [\![u]\!] \cdot [\![v]\!]\, ds \end{aligned} \tag{II.8}$$

with

$$a_H(u, v) = \sum_{K \in \mathcal{T}_H} a_H^K(u, v), \quad a_H^K(u, v) = \int_K \Big(2\mu \epsilon(u) : \epsilon(v) + \lambda \nabla \cdot u \nabla \cdot v \Big)\, dx, \tag{II.9}$$

where $\gamma > 0$ is a penalty parameter, n_E is a fixed unit normal vector defined on the coarse edge E and $\sigma(u)\, n_E$ is a matrix-vector product. Note that, in (II.8), the average and the jump operators are defined in the classical way. Specifically, consider an interior coarse edge $E \in \mathcal{E}^H$ and let K^+ and K^- be the two coarse grid blocks sharing the edge E. For a piecewise smooth function G, we define

$$\{G\} = \frac{1}{2}(G^+ + G^-), \qquad [\![G]\!] = G^+ - G^-, \qquad \text{on } E,$$

where $G^+ = G|_{K^+}$ and $G^- = G|_{K^-}$ and we assume that the normal vector n_E is pointing from K^+ to K^-. For a coarse edge E lying on the boundary ∂D, we define

$$\{G\} = [\![G]\!] = G, \qquad \text{on } E,$$

where we always assume that n_E is pointing outside of D. For vector-valued functions, the above average and jump operators are defined component-wise. We note that the DG coupling (II.7) is the classical interior penalty discontinuous Galerkin (IPDG) method with our multiscale basis functions.

Finally, we remark that, we use the same notations $V^{i,\text{snap}}$, $V^{i,\text{off}}$ and V^{off} to denote the local snapshot, local offline and global offline spaces for both the CG coupling and the DG coupling to simplify notations.

II.3 Construction of multiscale basis functions

This section is devoted to the construction of multiscale basis functions.

II.3.1 Basis functions for CG coupling

We begin by the construction of local snapshot spaces. Let ω_i be a coarse neighborhood, $i = 1, 2, \cdots, N_S$. We will define two types of local snapshot spaces. The first type

of local snapshot space is

$$V_1^{i,\text{snap}} = V^h(\omega_i),$$

where $V^h(\omega_i)$ is the restriction of the conforming space to ω_i. Therefore, $V_1^{i,\text{snap}}$ contains all possible fine scale functions defined on ω_i. The second type of local snapshot space contains all possible harmonic extensions. Next, let $V^h(\partial\omega_i)$ be the restriction of the conforming space to $\partial\omega_i$. Then we define the fine-grid delta function $\delta_k \in V^h(\partial\omega_i)$ on $\partial\omega_i$ by

$$\delta_k(x_l) = \begin{cases} 1, & l = k \\ 0, & l \neq k, \end{cases}$$

where $\{x_l\}$ are all fine grid nodes on $\partial\omega_i$. Given δ_k, we find u_{k1} and u_{k2} by

$$\begin{aligned} -\nabla \cdot \sigma(u_{k1}) &= 0, \quad \text{in } \omega_i \\ u_{k1} &= (\delta_k, 0)^T, \quad \text{on } \partial\omega_i \end{aligned} \tag{II.10}$$

and

$$\begin{aligned} -\nabla \cdot \sigma(u_{k2}) &= 0, \quad \text{in } \omega_i \\ u_{k2} &= (0, \delta_k)^T, \quad \text{on } \partial\omega_i. \end{aligned} \tag{II.11}$$

The linear span of the above harmonic extensions is our second type of local snapshot space $V_2^{i,\text{snap}}$. To simplify the notations, we will use $V^{i,\text{snap}}$ to denote $V_1^{i,\text{snap}}$ or $V_2^{i,\text{snap}}$ when there is no need to distinguish the two type of spaces. Moreover, we write

$$V^{i,\text{snap}} = \text{span}\{\psi_k^{i,\text{snap}}, \quad k = 1, 2, \cdots, M^{i,\text{snap}}\},$$

where $M^{i,\text{snap}}$ is the number of basis functions in $V^{i,\text{snap}}$.

We will perform a dimension reduction on the above snapshot spaces by the use of

a spectral problem. First, we will need a partition of unity function χ_i for the coarse neighborhood ω_i. One choice of a partition of unity function is the coarse grid hat functions Φ_i, that is, the piecewise bi-linear function on the coarse grid having value 1 at the coarse vertex x_i and value 0 at all other coarse vertices. The other choice is the multiscale partition of unity function, which is defined in the following way. Let K_j be a coarse grid block having the vertex x_i. Then we consider

$$\begin{aligned} -\nabla \cdot \sigma(\zeta_i) &= 0, \quad \text{in } K_j \\ \zeta_i &= (\Phi_i, 0)^T, \quad \text{on } \partial K_j. \end{aligned} \tag{II.12}$$

Then we define the multiscale partition of unity as $\widetilde{\Phi}_i = (\zeta_i)_1$. The values of $\widetilde{\Phi}_i$ on the other coarse grid blocks are defined similarly.

Based on our analysis to be presented in the next sections, we define the spectral problem as

$$\int_{\omega_i} \Big(2\mu\epsilon(u) : \epsilon(v) + \lambda \nabla \cdot u \, \nabla \cdot v \Big) \, dx = \xi \int_{\omega_i} \tilde{\kappa} u \cdot v \, dx, \tag{II.13}$$

where ξ denotes the eigenvalue and

$$\tilde{\kappa} = \sum_{i=1}^{N_S} (\lambda + 2\mu) |\nabla \chi_i|^2. \tag{II.14}$$

The above spectral problem (II.13) is solved in the snapshot space. We let (ϕ_k, ξ_k) be the eigenfunctions and the corresponding eigenvalues. Assume that

$$\xi_1 \leq \xi_2 \leq \cdots \leq \xi_{M^{i,\text{snap}}}.$$

Then the first L_i eigenfunctions will be used to construct the local offline space. We define

$$\psi_l^{i,\text{off}} = \sum_{k=1}^{M^{i,\text{snap}}} \phi_{lk} \psi_k^{i,\text{snap}}, \qquad l = 1, 2, \cdots, L_i, \tag{II.15}$$

where ϕ_{lk} is the k-th component of ϕ_l. The local offline space is then defined as

$$V^{i,\text{off}} = \text{span}\{\chi_i \psi_l^{i,\text{off}}, \quad l = 1, 2, \cdots, L_i\}.$$

Next, we define the global continuous Galerkin offline space as

$$V^{\text{off}} = \text{span}\{V^{i,\text{off}}, \quad i = 1, 2, \cdots, N_S\}.$$

II.3.2 Basis functions for DG coupling

We will construct the local basis functions required for the DG coupling. We also provide two types of snapshot spaces as in CG case. The first type of local snapshot space is all possible fine grid bi-linear functions defined on K_i. The second type of local snapshot space $V^{i,\text{snap}}$ for the coarse grid block K_i is defined as the linear span of all harmonic extensions. Specifically, given δ_k, we find u_{k1} and u_{k2} by

$$\begin{aligned} -\nabla \cdot \sigma(u_{k1}) &= 0, \quad \text{in } K_i \\ u_{k1} &= (\delta_k, 0)^T, \quad \text{on } \partial K_i \end{aligned} \tag{II.16}$$

and

$$\begin{aligned} -\nabla \cdot \sigma(u_{k2}) &= 0, \quad \text{in } K_i \\ u_{k2} &= (0, \delta_k)^T, \quad \text{on } \partial K_i. \end{aligned} \tag{II.17}$$

The linear span of the above harmonic extensions is the local snapshot space $V^{i,\text{snap}}$. We also write

$$V^{i,\text{snap}} = \text{span}\{\psi_k^{i,\text{snap}}, \quad k = 1, 2, \cdots, M^{i,\text{snap}}\},$$

where $M^{i,\text{snap}}$ is the number of basis functions in $V^{i,\text{snap}}$.

We will perform a dimension reduction on the above snapshot spaces by the use of a spectral problem. Based on our analysis to be presented in the next sections, we define the spectral problem as

$$\int_{K_i} \big(2\mu\epsilon(u) : \epsilon(v) + \lambda\nabla \cdot u\nabla \cdot v\big)dx = \frac{\xi}{H}\int_{\partial K_i} \langle\lambda + 2\mu\rangle\, u \cdot v\; ds, \tag{II.18}$$

where ξ denotes the eigenvalues and $\langle\lambda + 2\mu\rangle$ is the maximum value of $\{\lambda + 2\mu\}$ on ∂K_i. The above spectral problem (II.18) is again solved in the snapshot space $V^{i,\text{snap}}$. We let (ϕ_k, ξ_k), for $k = 1, 2, \cdots, M^{i,\text{snap}}$ be the eigenfunctions and the corresponding eigenvalues. Assume that

$$\xi_1 \leq \xi_2 \leq \cdots \leq \xi_{M^{i,\text{snap}}}.$$

Then the first L_i eigenfunctions will be used to construct the local offline space. Indeed, we define

$$\psi_l^{i,\text{off}} = \sum_{k=1}^{M^{i,\text{snap}}} \phi_{lk}\psi_k^{i,\text{snap}}, \qquad l = 1, 2, \cdots, L_i, \tag{II.19}$$

where ϕ_{lk} is the k-th component of ϕ_l. The local offline space is then defined as

$$V^{i,\text{off}} = \text{span}\{\psi_l^{i,\text{off}}, \quad l = 1, 2, \cdots, L_i\}.$$

The global offline space is also defined as

$$V^{\text{off}} = \text{span}\{V^{i,\text{off}}, \quad i = 1, 2, \cdots, N\}.$$

II.3.3 Oversampling technique

In this section, we present an oversampling technique for generating multiscale basis functions. The main idea of oversampling is to solve local spectral problem in a larger domain. This allows obtaining a snapshot space that has a smaller dimension since snapshot vectors contain solutions oscillating near the boundaries. In our previous approaches, we assume that the snapshot vectors can have an arbitrary value on the boundary of coarse blocks which yield to large dimensional coarse spaces.

For the harmonic extension snapshot case, we solve equation (II.10) and (II.11) in ω_i^+ (see Figure II.1) instead of ω_i for CG case, and solve the equation (II.16) and (II.17) in K_i^+ instead of K_i for DG case. We denote the solutions as $\psi_i^{+,\text{snap}}$, and their restrictions on ω_i or K_i as ψ_i^{snap}. We reorder these functions according to eigenvalue behavior and write

$$R_{\text{snap}}^{+} = \left[\psi_1^{+,\text{snap}}, \ldots, \psi_{M_{\text{snap}}}^{+,\text{snap}}\right] \quad \text{and} \quad R_{\text{snap}} = \left[\psi_1^{\text{snap}}, \ldots, \psi_{M_{\text{snap}}}^{\text{snap}}\right].$$

where M_{snap} denotes the total number of functions kept in the snapshot space.

For CG case we define the following spectral problems in the space of snapshot:

$$R_{\text{snap}}^{T} A R_{\text{snap}} \Psi_k = \zeta (R_{\text{snap}}^{+})^{T} M^{+} R_{\text{snap}}^{+} \Psi_k, \tag{II.20}$$

or

$$(R_{\text{snap}}^{+})^{T} A^{+} R_{\text{snap}}^{+} \Psi_k = \zeta (R_{\text{snap}}^{+})^{T} M^{+} R_{\text{snap}}^{+} \Psi_k, \tag{II.21}$$

where

$$A = [a_{kl}] = \int_{\omega_i} \left(2\mu\epsilon(\psi_k^{\text{snap}}) : \epsilon(\psi_l^{\text{snap}}) + \lambda\nabla\cdot\psi_k^{\text{snap}}\,\nabla\cdot\psi_l^{\text{snap}}\right) dx,$$
$$A^+ = [a_{kl}^+] = \int_{\omega_i^+} \left(2\mu\epsilon(\psi_k^{+,\text{snap}}) : \epsilon(\psi_l^{+,\text{snap}}) + \lambda\nabla\cdot\psi_k^{+,\text{snap}}\,\nabla\cdot\psi_l^{+,\text{snap}}\right) dx,$$
$$M^+ = [m_{kl}^+] = \int_{\omega_i^+} \tilde{\kappa}\psi_k^{+,\text{snap}}\cdot\psi_l^{+,\text{snap}}\, dx,$$

where $\tilde{\kappa}$ is defined through (II.14).

The local spectral problem for DG coupling is defined as

$$(R_{\text{snap}}^+)^T A^+ R_{\text{snap}}^+ \Psi_k = \zeta (R_{\text{snap}}^+)^T M_1^+ R_{\text{snap}}^+ \Psi_k \tag{II.22}$$

or

$$(R_{\text{snap}}^+)^T A^+ R_{\text{snap}}^+ \Psi_k = \zeta (R_{\text{snap}}^+)^T M_2^+ R_{\text{snap}}^+ \Psi_k \tag{II.23}$$

in the snapshot space, where

$$A^+ = [a_{kl}^+] = \int_{K_i^+} \left(2\mu\epsilon(\psi_k^{+,\text{snap}}) : \epsilon(\psi_l^{+,\text{snap}}) + \lambda\nabla\cdot\psi_k^{+,\text{snap}}\,\nabla\cdot\psi_l^{+,\text{snap}}\right) dx,$$
$$M_1^+ = [m_{1,kl}^+] = \frac{1}{H}\int_{K_i^+} \{\lambda + 2\mu\}\psi_k^{+,\text{snap}}\cdot\psi_l^{+,\text{snap}}\, dx,$$
$$M_2^+ = [m_{2,kl}^+] = \frac{1}{H}\int_{\partial K_i^+} \{\lambda + 2\mu\}\psi_k^{+,\text{snap}}\cdot\psi_l^{+,\text{snap}}\, ds.$$

After solving above local spectral problems, we form the offline space as in the no oversampling case, see Section II.3.1 for CG coupling and Section II.3.2 for DG coupling.

II.4 Numerical result

In this section, we present numerical results for CG-GMsFEM and DG-GMsFEM with two models. We consider different choices of snapshot spaces such as local-fine grid

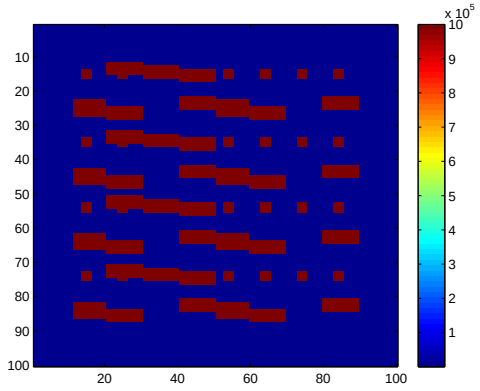

Figure II.2: Young's modulus (Model 1)

functions and harmonic functions and use different local spectral problems such as no-oversampling and oversampling described in the previous section. For the first model, we consider the medium that has no-scale separation and features such as high conductivity channels and isolated inclusions. The Young's modulus $E(x)$ is depicted in Figure II.2, $\lambda(x) = \frac{\nu}{(1+\nu)(1-2\nu)}E(x)$, $\mu(x) = \frac{1}{2(1+\nu)}E(x)$, the Poisson ratio ν is taken to be 0.20. For the second example, we use the model that is used in [43] for the simulation of sub-surface elastic waves (see Figure II.3). In all numerical tests, we use constant force and homogeneous Dirchlet boundary condition. In all tables below, Λ_* represent the minimum discarded eigenvalue of the corresponding spectral problem. We note that the first three eigenbasis (that correspond to the first three smallest eigenvalues) are constant and linear functions, therefore we present our numerical results starting from fourth eigenbasis in all cases. In the below, dimension of a solution represents the total number of basis used for the finite element space.

Before presenting the numerical results, we summarize our numerical findings.

- We observe a fast decay in the error as more basis functions are added in both CG-GMsFEM and DG-GMsFEM

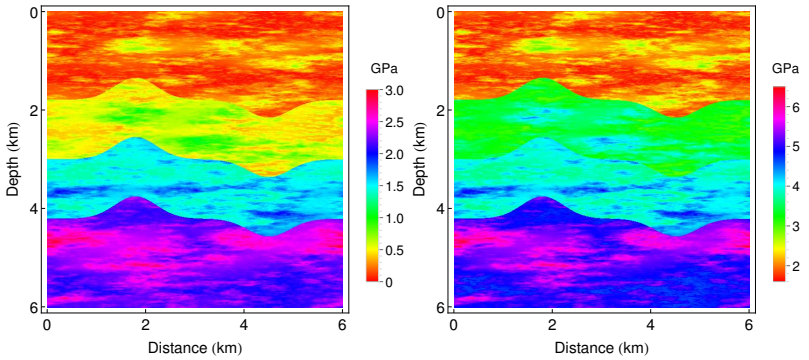

Figure II.3: Left: λ Right: μ (Model 2)

- We observe the use of multiscale partition of unity improves the accuracy of CG-GMsFEM compared to the use of piecewise bi-linear functions

- We observe an improvement in the accuracy (a slight improvement in CG case and a large improvement in DG case) when using oversampling for the examples we considered and the decrease in the snapshot space dimension

II.4.1 Numerical results for Model 1 with conforming GMsFEM (CG-GMsFEM)

For the first model, we divide the domain $D = [0, 1] \times [0, 1]$ into 10×10 coarse grid blocks, inside each coarse block we use 10×10 fine scale square blocks, which results in a 100×100 fine grid blocks. The number of basis functions used to get the reference solution is 20402. We will show the performance of CG-GMsFEM with the use of local fine-scale snapshots and harmonic extension snapshots. Both bi-linear and multiscale partition of unity functions (see Section II.3.1) will be considered. For each case, we will provide the comparsion using oversampling and no-oversampling. For the error measure, we use relative weighted L^2 norm error and weighted H^1 norm error to compare the accuracy of

CG-GMsFEM, which is defined as

$$e_{L^2} = \frac{\|(\lambda + 2\mu)(u_H - u_h)\|_{L^2(D)}}{\|(\lambda + 2\mu)u_h\|_{L^2(D)}}, \quad e_{H^1} = \sqrt{\frac{a(u_H - u_h, u_H - u_h)}{a(u_h, u_h)}}$$

where u_H and u_h are CG-GMsFEM defined in (II.6) and fine-scale CG-FEM solution defined in (II.3) respectively.

Tables II.1 and II.2 show the numerical results of using local fine-scale snapshots with piecewise bi-linear function and multiscale functions as partition of unity respectively. As we observe, when using more multiscale basis, the errors decay rapidly, especially for multiscale partition of unity. For example, we can see that the weighted L^2 error drops from 24.1% to 1.1% in the case of using bi-linear function as partition of unity with no oversampling, while the dimension increases from 648 to 2592. If we use multiscale partition of unity, the corresponding weighted L^2 error drops from 8.2% to 0.5%, which demonstrates a great advantage of multiscale partition of unity. Oversampling can help improve the accuracy as our results indicate. The local eigenvalue problem used for oversampling is Eq.(II.21).

Next, we present the numerical results when harmonic extensions are used as snapshots in Tables II.3 and II.4. We can observe similar trends as in the local fine-scale snapshot case. The errors decrease as the number of basis functions increase. The L^2 error is less than 1% when about 13% of degrees of freedom is used. Similarly, the oversampling method helps to improve the accuracy. In this case, the local eigenvalue problem used for oversampling is Eq.(II.20).

II.4.2 Numerical results for Model 1 with DG-GMsFEM

In this section, we consider numerical results for DG-GMsFEM discussed in Section II.3.2. To show the performance of DG-GMsFEM, we use the same model (see Figure

Dimension	$1/\Lambda_*$		e_{H^1}		e_{L^2}	
	without oversampling	with oversampling	without oversampling	with oversampling	without oversampling	with oversampling
648	2.61e+05	2.77e+05	4.36e-01	4.47e-01	2.41e-01	2.60e-01
1134	9.56e+04	1.20e+05	2.20e-01	2.18e-01	4.82e-02	4.77e-02
1620	2.11e+04	5.83e+04	1.61e-01	1.57e-01	2.65e-02	2.49e-02
2106	8.28e-01	2.08e+04	1.32e-01	1.29e-01	1.78e-02	1.70e-02
2592	5.32e-01	4.38e+00	1.05e-01	1.06e-01	1.13e-02	1.15e-02

Table II.1: Relative errors between CG-MsFEM solution and the fine-scale CG-FEM solution, piecewise bi-linear partition of unity functions are used. The case with local fine-scale snapshots.

Dimension	$1/\Lambda_*$		e_{H^1}		e_{L^2}	
	without oversampling	with oversampling	without oversampling	with oversampling	without oversampling	with oversampling
648	1.62e+05	1.81e+05	2.52e-01	2.76e-01	8.23e-02	8.23e-02
1134	2.11e+00	7.88e+04	1.67e-01	1.65e-01	3.11e-02	3.03e-02
1620	1.08e+00	3.75e+04	1.11e-01	1.11e-02	1.44e-02	1.34e-02
2106	6.37e-01	8.25e+00	8.78e-02	8.82e-02	8.33e-03	8.16e-02
2592	4.98e-01	1.81e+00	7.08e-02	7.13e-02	5.49e-03	5.27e-03

Table II.2: Relative errors between CG-MsFEM solution and the fine-scale CG-FEM solution, multiscale partition of unity functions are used. The case with local fine-scale snapshots.

Dimension	$1/\Lambda_*$		e_{H^1}		e_{L^2}	
	without oversampling	with oversampling	without oversampling	with oversampling	without oversampling	with oversampling
648	2.59e+05	9.95e+05	4.44e-01	4.41e-01	2.52e-01	2.53e-01
1134	5.42e+04	4.90e+05	2.18e-01	2.15e-01	4.72e-02	4.62e-02
1620	4.94e+03	3.57e+04	1.54e-01	1.48e-01	2.39e-02	2.22e-02
2106	5.08e-01	1.75e+04	1.25e-01	1.24e-01	1.60e-02	1.55e-02
2592	2.97e-01	9.82e+00	1.03e-01	1.04e-01	1.09e-02	1.10e-02

Table II.3: Relative errors between CG-MsFEM solution and the fine-scale CG-FEM solution, piecewise bi-linear partition of unity functions are used. The case with hamonic snapshots.

Dimension	$1/\Lambda_*$		e_{H^1}		e_{L^2}	
	without oversampling	with oversampling	without oversampling	with oversampling	without oversampling	with oversampling
648	1.62e+05	5.19e+05	2.57e-01	2.95e-01	8.48e-02	1.16e-01
1134	1.78e+00	2.68e+05	1.73e-01	1.70e-01	3.38e-02	3.07e-02
1620	8.21e-01	1.85e+05	1.15e-01	1.11e-02	1.52e-02	1.28e-02
2106	4.89e-01	1.00e+04	9.01e-02	8.89e-02	8.89e-03	8.30e-02
2592	3.96e-01	5.57e+04	7.57e-02	7.45e-02	6.51e-03	6.04e-03

Table II.4: Relative errors between CG-MsFEM solution and the fine-scale CG-FEM solution, multiscale partition of unity functions are used. The case with hamonic snapshots.

II.2) and the coarse and fine grid settings as in the CG case. We will also present the result of using both harmonic extension and eigenbasis (local fine-scale) as snapshot space. To measure the error, we define broken weighted L^2 norm error and H^1 norm error

$$e_{H^1} = \sqrt{\frac{\sum_{K\in\mathcal{T}_H}\int_K \sigma(u_H - u_h)) : \varepsilon(u_H - u_h))\, dx}{\sum_{K\in\mathcal{T}_H}\int_K \sigma(u_h) : \varepsilon(u_h)\, dx}}$$

where u_H and u_h are DG-GMsFEM defined in (II.7) and fine-scale DG-FEM solution defined in (II.49) respectively. We note that the dimension of the reference solution u_h here is 24200.

In Table II.5, the numerical results of DG-MsFEM with local fine-scale functions as the snapshot space is shown. We observe that DG-MsFEM shows a better approximation compared to CG-MsFEM if oversampling is used. The error decreases more rapidly as we add basis. More specifically, the relative broken L^2 error and H^1 error decrease from 33.6%, 62.8% to 0.7% and 8.1% respectively, while the degrees of freedom of the coarse system increase from 728 to 2696, where the latter is only 13.2% of the reference solution. The local eigenvalue problem used for oversampling is Eq.(II.22).

Table II.6 shows the corresponding results when harmonic functions are used to construct the snapshot space. We observe similar errors decay trend as local fine-scale snapshots are used. Oversampling can help improve the results significantly. Although the error is very large when the dimension of coarse system is 728 (4 multiscale basis is used), the error becomes very small when the dimension reaches 1728 (9 multiscale basis is used). The local eigenvalue problem used for oversampling here is Eq.(II.23). We remark that oversampling can not only help decrease the error, but also decrease the dimension of the snapshot space greatly in periodic case. Increasing the the oversampling domain will decrease the error but will increase the computational time of the offline stage. We also remark that the optimal penalty here depends on the number of basis, in our simulation we

Dimension	$1/\Lambda_*$		e_{H^1}		e_{L^2}	
	without oversampling	with oversampling	without oversampling	with oversampling	without oversampling	with oversampling
728	1.4e-03	1.5e-03	0.628	0.539	0.511	0.336
1184	8.2e-04	2.2e-04	0.437	0.231	0.231	0.056
1728	5.4e-04	1.5e-03	0.387	0.181	0.181	0.407
2184	3.6e-04	8.9e-04	0.356	0.130	0.146	0.021
2696	2.8e-04	7.4e-04	0.311	0.081	0.100	0.007

Table II.5: Relative errors between DG-MsFEM solution and the fine-scale DG-FEM solution. The case with local fine-scale snapshots.

Dimension	$1/\Lambda_*$		e_{H^1}		e_{L^2}	
	without oversampling	with oversampling	without oversampling	with oversampling	without oversampling	with oversampling
728	1.4e-01	2.3e-01	0.640	0.561	0.511	0.363
1184	5.7e-02	9.7e-02	0.520	0.402	0.319	0.180
1728	4.7e-02	8.0e-02	0.405	0.172	0.205	0.031
2184	3.4e-02	5.6e-02	0.307	0.099	0.119	0.012
2696	2.5e-02	4.1e-02	0.235	0.080	0.057	0.006

Table II.6: Relative errors between DG-MsFEM solution and the fine-scale DG-FEM solution. The case with hamonic snapshots

use uniform penalty.

II.4.3 Numerical results for Model 2

The purpose of this example is to test a method for an earth model that is used in [43]. The domain for the second model is $D = (0, 6000)^2$ (in meters) which is divided into $900 = 30 \times 30$ square coarse grid blocks, inside each coarse block we generate 20×20 fine scale square blocks. The reference solution is computed through standard CG-FEM on the resulting 600×600 fine grid. We note that the dimension of the reference solution is 722402. The numerical results for CG-MsFEM and DG-MsFEM are presented in Tables II.7 and II.8 respectively. We observe the relatively low errors compared to the high contrast case and the error decrease with the dimension increase of the offline space. Both coupling methods (CG and DG) show very good approximation ability.

dimension	$\frac{1}{\Lambda_*}$	e_{H^1}	e_{L^2}
6968	4.9e+00	5.4e-02	3.1e-03
8650	4.5e+00	5.2e-02	2.7e-03
10332	3.9e+00	4.9e-02	2.5e-03
12014	3.6e+00	4.7e-02	2.2e-03

Table II.7: Relative errors between CG-MsFEM solution and the fine-scale CG-FEM solution, piecewise bi-linear partition of unity functions are used. The case with local fine-scale snapshots.

dimension	$\frac{1}{\Lambda_*}$	e_{H^1}	e_{L^2}
7200	6.3e-06	7.1e-02	4.1e-03
9000	6.0e-06	6.6e-02	4.0e-03
10800	4.6e-06	6.3e-02	3.8e-03
12600	4.5e-06	5.9e-02	3.1e-03

Table II.8: Relative errors between DG-MsFEM solution and the fine-scale CG-FEM solution. The case with local fine-scale snapshots.

II.5 Error estimate for CG coupling

In this section, we present error analysis for both no oversampling and oversampling cases. In the discussions below, $a \preceq b$ means $a \leq Cb$, where C is a constant independent of the mesh size and the contrast of the coefficient.

II.5.1 No oversampling case

Lemma II.5.1. *Let ω_n be a coarse neighborhood. For any $\psi \in H^1(\omega_n)$, we define $r = -\mathrm{div}(\sigma(\psi))$. Then we have*

$$\int_{\omega_n} 2\mu\chi_n^2\epsilon(\psi) : \epsilon(\psi)\, dx + \int_{\omega_n} \lambda\chi_n^2(\nabla\cdot\psi)^2\, dx \preceq |\int_{\omega_n} \chi_n^2 r\cdot\psi\, dx| + \int_{\omega_n} (\lambda+2\mu)|\nabla\chi_n|^2\psi^2\, dx, \tag{II.24}$$

where χ_n is a scalar partition of unity subordinated to the coarse neighborhood ω_n.

Proof. Multiplying both sides of $-\mathrm{div}(\sigma(\psi)) = r$ by $\chi_n^2\psi$, we have

$$\begin{aligned}
\int_{\omega_n} \chi_n^2 r\cdot\psi\ dx &= \int_{\omega_n} 2\mu\epsilon(\psi):\epsilon(\chi_n^2\psi)\ dx + \int_{\omega_n}\lambda\nabla\cdot\psi\nabla\cdot(\chi_n^2\psi)\ dx \\
&= \int_{\omega_n} 2\mu\chi_n^2\epsilon(\psi):\epsilon(\psi)\ dx + \int_{\omega_n} 2\mu\chi_n\epsilon_{ij}(\psi)(\psi_i\frac{\partial\chi_n}{\partial x_j}+\psi_j\frac{\partial\chi_n}{\partial x_i})\ dx \\
&\quad + \int_{\omega_n}\lambda\chi_n^2(\nabla\cdot\psi)^2\ dx + \int_{\omega_n} 2\lambda\nabla\cdot\psi\chi_n\psi\cdot\nabla\chi_n\ dx \\
&= \int_{\omega_n} 2\mu\chi_n^2\epsilon(\psi):\epsilon(\psi)\ dx + \int_{\omega_n}\lambda\chi_n^2(\nabla\cdot\psi)^2\ dx \\
&\quad + \int_{\omega_n} 2\big(\sqrt{2\mu}\chi_n\epsilon_{ij}(\psi)\big)\big(\sqrt{\mu/2}(\psi_i\frac{\partial\chi_n}{\partial x_j}\ dx+\psi_j\frac{\partial\chi_n}{\partial x_i})\big)\ dx \\
&\quad + \int_{\omega_n} 2\big(\sqrt{\lambda}\chi_n\nabla\cdot\psi\big)\big(\sqrt{\lambda}\psi\cdot\nabla\chi_n\big)\ dx.
\end{aligned} \tag{II.25}$$

Therefore,

$$\begin{aligned}
&\int_{\omega_n} 2\mu\chi_n^2\epsilon(\psi):\epsilon(\psi)\ dx + \int_{\omega_n}\lambda\chi_n^2(\nabla\cdot\psi)^2\ dx \\
&\le |\int_{\omega_n}\chi_n^2 r\cdot\psi\ dx| + |\int_{\omega_n} 2\big(\sqrt{2\mu}\chi_n\epsilon_{ij}(\psi)\big)\big(\sqrt{\mu/2}(\psi_i\frac{\partial\chi_n}{\partial x_j}+\psi_j\frac{\partial\chi_n}{\partial x_i})\big)\ dx \\
&\quad + \int_{\omega_n} 2(\sqrt{\lambda}\chi_n\nabla\cdot\psi)(\sqrt{\lambda}\psi\cdot\nabla\chi_n)\ dx| \\
&\preceq |\int_{\omega_n}\chi_n^2 r\cdot\psi\ dx| + \int_{\omega_n}(2\lambda+4\mu)|\nabla\chi_n|^2\psi^2\ dx \\
&\preceq |\int_{\omega_n}\chi_n^2 r\cdot\psi\ dx| + \int_{\omega_n}(\lambda+2\mu)|\nabla\chi_n|^2\psi^2\ dx.
\end{aligned} \tag{II.26}$$

In the last step, we have used $2ab \le \epsilon a^2 + \frac{1}{\epsilon}b^2 \quad (\epsilon > 0)$, and $(ab+cd)^2 \le (a^2+c^2)(b^2+d^2)$.

□

Next, we will show the convergence of the CG-GMsFEM solution defined in (II.6) without oversampling. We take $I^{\omega_n}u_h$ to be the first L_n terms of spectral expansion of u in terms of eigenfunctions of the problem $-\mathrm{div}(\sigma(\phi_n)) = \xi\tilde{\kappa}\phi_n$ solved in $V^h(\omega_n)$. Applying

Cea's Lemma, Lemma II.5.1 and using the fact that $|\chi_n| \preceq 1$, we can get

$$
\begin{aligned}
&\int_D \left(2\mu\epsilon(u_h - u_H) : \epsilon(u_h - u_H) + \lambda(\nabla \cdot (u_h - u_H))^2\right)\, dx \\
&\preceq \sum_{n=1}^{N_s} \int_{\omega_n} 2\mu\epsilon(\chi_n(u_h - I^{\omega_n} u_h)) : \epsilon(\chi_n(u_h - I^{\omega_n} u_h))\, dx \\
&\quad + \sum_{n=1}^{N_s} \int_{\omega_n} 2\lambda(\nabla \cdot (\chi_n(u_h - I^{\omega_n} u_h)))^2\, dx \\
&\preceq \sum_{n=1}^{N_s} \int_{\omega_n} 2\mu\chi_n^2\epsilon(u_h - I^{\omega_n} u_h) : \epsilon(u_h - I^{\omega_n} u_h)\, dx \\
&\quad + \sum_{n=1}^{N_s} \int_{\omega_n} \lambda\chi_n^2(\nabla \cdot (u_h - I^{\omega_n} u_h))^2\, dx + \sum_{n=1}^{N_s} \int_{\omega_n} (\lambda + 2\mu)|\nabla\chi_n|^2(u_h - I^{\omega_n} u_h)^2\, dx \\
&\preceq \sum_{n=1}^{N_s} \int_{\omega_n} (\lambda + 2\mu)|\nabla\chi_n|^2(u_h - I^{\omega_n} u_h)^2\, dx + \sum_{n=1}^{N_s} \left| \int_{\omega_n} \chi_n^2 g \cdot (u_h - I^{\omega_n} u_h)\right| dx \\
&\preceq \sum_{n=1}^{N_s} \int_{\omega_n} (\lambda + 2\mu)|\nabla\chi_n|^2(u_h - I^{\omega_n} u_h)^2\, dx + \sum_{n=1}^{N_s} \int_{\omega_n} ((\lambda + 2\mu)|\nabla\chi_n|^2)^{-1} g^2\, dx,
\end{aligned}
\tag{II.27}
$$

where $g = f_h + \text{div}(\sigma(I^{\omega_n} u_h))$, f_h is the L^2 projection of f in V^h, f is the right hand side of (II.1).

Using the properties of the eigenfunctions, we obtain

$$
\begin{aligned}
&\int_{\omega_n} (\lambda + 2\mu) \sum_{s=1}^{N_s} |\nabla\chi_s|^2 (u_h - I^{\omega_n} u_h)^2\, dx \\
&\preceq \frac{1}{\xi_{L_n+1}^{\omega_n}} \int_{\omega_n} \left(2\mu\epsilon(u_h - I^{\omega_n} u_h) : \epsilon(u_h - I^{\omega_n} u_h) + \lambda(\nabla \cdot (u_h - I^{\omega_n} u_h))^2\right)\, dx.
\end{aligned}
\tag{II.28}
$$

Then, the first term in the right hand side of (II.27) can be estimated as follows

$$
\begin{aligned}
&\sum_{n=1}^{N_s}\int_{\omega_n}(\lambda+2\mu)|\nabla\chi_n|^2(u_h-I^{\omega_n}u_h)^2\,dx\\
&\preceq\sum_{n=1}^{N_s}\int_{\omega_n}(\lambda+2\mu)\sum_{s=1}^{N_s}|\nabla\chi_s|^2|(u_h-I^{\omega_n}u_h)^2\,dx\\
&\preceq\sum_{n=1}^{N_s}\frac{1}{\xi^{\omega_n}_{L_n+1}}\int_{\omega_n}\left(2\mu\epsilon(u_h-I^{\omega_n}u_h):\epsilon(u_h-I^{\omega_n}u_h)+\lambda(\nabla\cdot(u_h-I^{\omega_n}u_h))^2\right)\,dx\\
&\preceq\sum_{n=1}^{N_s}\frac{\alpha^{\omega_n}_{L_n+1}}{\xi^{\omega_n}_{L_n+1}}\int_{\omega_n}\left(2\mu\chi_n^2\epsilon(u_h-I^{\omega_n}u_h):\epsilon(u_h-I^{\omega_n}u_h)+\lambda\chi_n^2(\nabla\cdot(u_h-I^{\omega_n}u_h))^2\right)\,dx\\
&\preceq\sum_{n=1}^{N_s}\frac{\alpha^{\omega_n}_{L_n+1}}{\xi^{\omega_n}_{L_n+1}}\int_{\omega_n}(\lambda+2\mu)|\nabla\chi_n|^2(u_h-I^{\omega_n}u_h)^2\,dx\\
&\quad+\sum_{n=1}^{N_s}\frac{\alpha^{\omega_n}_{L_n+1}}{\xi^{\omega_n}_{L_n+1}}|\int_{\omega_n}\chi_n^2 g\cdot(u_h-I^{\omega_n}u_h)\,dx|\\
&\preceq\frac{1}{\Lambda_*}\left(\sum_{n=1}^{N_s}\int_{\omega_n}(\lambda+2\mu)|\nabla\chi_n|^2(u_h-I^{\omega_n}u_h)^2\,dx+\sum_{n=1}^{N_s}|\int_{\omega_n}\chi_n^2 g\cdot(u_h-I^{\omega_n}u_h)\,dx|\right),
\end{aligned}
\tag{II.29}
$$

where

$$\Lambda_*=\min_{\omega_n}\frac{\xi^{\omega_n}_{L_n+1}}{\alpha^{\omega_n}_{L_n+1}},$$

and

$$\alpha^{\omega_n}_{L_n+1}=\frac{\int_{\omega_n}2\mu\epsilon(u_h-I^{\omega_n}u_h):\epsilon(u_h-I^{\omega_n}u_h)\,dx+\int_{\omega_n}\lambda(\nabla\cdot(u_h-I^{\omega_n}u_h))^2\,dx}{\int_{\omega_n}2\mu\chi_n^2\epsilon(u_h-I^{\omega_n}u_h):\epsilon(u_h-I^{\omega_n}u_h)\,dx+\int_{\omega_n}\lambda\chi_n^2(\nabla\cdot(u_h-I^{\omega_n}u_h))^2\,dx}.$$

Applying inequality (II.29) m times, we have

$$\begin{aligned}
&\sum_{n=1}^{N_s}\int_{\omega_n}(\lambda+2\mu)|\nabla\chi_n|^2(u_h-I^{\omega_n}u_h)^2\,dx\\
&\preceq\left(\frac{1}{\Lambda_*}\right)^m\sum_{n=1}^{N_s}\int_{\omega_n}(\lambda+2\mu)|\nabla\chi_n|^2(u_h-I^{\omega_n}u_h)^2\,dx\\
&\quad+\sum_{l=1}^{m}\left(\frac{1}{\Lambda_*}\right)^l\sum_{n=1}^{N_s}|\int_{\omega_n}\chi_n^2 g\cdot(u_h-I^{\omega_n}u_h)\,dx| \qquad \text{(II.30)}\\
&\preceq\left(\frac{1}{\Lambda_*}\right)^m\sum_{n=1}^{N_s}\int_{\omega_n}(\lambda+2\mu)|\nabla\chi_n|^2(u_h-I^{\omega_n}u_h)^2\,dx\\
&\quad+(\Lambda_*)^m\left(\frac{1-\Lambda_*^{-m}}{\Lambda_*-1}\right)\sum_{n=1}^{N_s}\int_{\omega_n}((\lambda+2\mu)|\nabla\chi_n|^2)^{-1}g^2\,dx,
\end{aligned}$$

Taking into account that

$$\sum_{n=1}^{N_s}\int_{\omega_n}(\lambda+2\mu)|\nabla\chi_n|^2(u_h-I^{\omega_n}u_h)^2\,dx\preceq\sum_{n=1}^{N_s}\int_{\omega_n}(\lambda+2\mu)\sum_{s=1}^{N_s}|\nabla\chi_s|^2(u_h-I^{\omega_n}u_h)^2\,dx, \qquad \text{(II.31)}$$

and

$$\begin{aligned}
&\sum_{n=1}^{N_s}\int_{\omega_n}\left(2\mu\epsilon(u_h-I^{\omega_n}u_h):\epsilon(u_h-I^{\omega_n}u_h)\,dx+\lambda(\nabla\cdot(u_h-I^{\omega_n}u_h))^2\right)\,dx \qquad \text{(II.32)}\\
&\preceq\int_D\left(2\mu\epsilon(u_h):\epsilon(u_h)+\lambda(\nabla\cdot u_h)^2\right)\,dx.
\end{aligned}$$

inequality (II.27) becomes

$$\begin{aligned}
&\int_D \left(2\mu\epsilon(u_h - u_H) : \epsilon(u_h - u_H) + \lambda(\nabla \cdot (u_h - u_H))^2\right)\, dx \\
&\preceq \left(\frac{1}{\Lambda_*}\right)^{m+1} \sum_{n=1}^{N_s} \int_{\omega_n} \left(2\mu\epsilon(u_h - I^{\omega_n} u_h) : \epsilon(u_h - I^{\omega_n} u_h) + \lambda(\nabla \cdot (u_h - I^{\omega_n} u_h))^2\right)\, dx \\
&\quad + \left(\Lambda_*^m \left(\frac{1 - \Lambda_*^{-m}}{\Lambda_* - 1}\right) + 1\right) \sum_{n=1}^{N_s} \int_{\omega_n} ((\lambda + 2\mu)|\nabla \chi_n|^2)^{-1} g^2\, dx \\
&\preceq \left(\frac{1}{\Lambda_*}\right)^{m+1} \int_D \left(2\mu\epsilon(u_h) : \epsilon(u) + \lambda(\nabla \cdot u_h)^2\right)\, dx + \left((\Lambda_*)^m \left(\frac{1 - (\Lambda_*)^{-m}}{\Lambda_* - 1}\right) + 1\right) R,
\end{aligned} \tag{II.33}$$

where $R = \sum_{n=1}^{N_s} \int_{\omega_n} ((\lambda + 2\mu)|\nabla \chi_n|^2)^{-1} g^2\, dx$. If $|g| \preceq 1$, then we have $\int_{\omega_n} ((\lambda + 2\mu)|\nabla \chi_n|^2)^{-1} g^2\, dx \preceq H^2$, from which we obtain

$$\begin{aligned}
&\int_D \left(2\mu\epsilon(u_h - u_H) : \epsilon(u_h - u_H) + \lambda(\nabla \cdot (u_h - u_H))^2\right)\, dx \\
&\preceq \left(\frac{1}{\Lambda_*}\right)^{m+1} \int_D \left(2\mu\epsilon(u_h) : \epsilon(u) + \lambda(\nabla \cdot u_h)^2\right)\, dx + \left((\Lambda_*)^m \left(\frac{1 - (\Lambda_*)^{-m}}{\Lambda_* - 1}\right) + 1\right) H^2.
\end{aligned} \tag{II.34}$$

Combining results above, we have

Theorem II.5.2. *Let $u_h \in V_{CG}^h$ be the fine-scale CG-FEM solution defined in (II.3) and u_H be the CG-GMsFEM solution defined in (II.6) without oversampling. If $\Lambda_* > 1$ and $\int_D (\lambda + 2\mu)^{-1} g^2\, dx \preceq 1$, let $n = -\frac{\log(H)}{\log \Lambda_*}$, then*

$$\begin{aligned}
&\int_D \left(2\mu\epsilon(u_h - u_H) : \epsilon(u_h - u_H) + \lambda(\nabla \cdot (u_h - u_H))^2\right)\, dx \\
&\preceq \left(\frac{H}{\Lambda_*}\right) \left(\int_D \left(2\mu\epsilon(u_h) : \epsilon(u_h) + \lambda(\nabla \cdot u_h)^2\right)\, dx + 1\right).
\end{aligned}$$

II.5.2 Oversampling case

In this subsection, we will analyze the convergence of CG-GMsFEM solution defined in (II.6) with oversampling. We define $I^{\omega_n^+}u_h$ as an interpolation of u_h in ω_n^+ using the first L_n modes for the eigenvalue problem (II.20). Let χ_n^+ be a partition of unity subordinated to the coarse neighborhood ω_n^+. We require χ_n^+ to be zero on $\partial\omega_n^+$ and

$$|\nabla\chi_n|^2 \preceq |\nabla\chi_n^+|^2.$$

Using the same argument as Lemma II.5.1, it is easy to deduce

$$\begin{aligned}&\int_{\omega_n^+}\left(2\mu|\chi_n^+|^2\epsilon(u_h-I^{\omega_n^+}u_h):\epsilon(u_h-I^{\omega_n^+}u_h)+\lambda|\chi_n^+|^2(\nabla\cdot(u_h-I^{\omega_n^+}u_h))^2\right)\,dx\\ \preceq&|\int_{\omega_n^+}|\chi_n^+|^2g\cdot(u_h-I^{\omega_n^+}u_h)\,dx|+\int_{\omega_n^+}(\lambda+2\mu)|\nabla\chi_n^+|^2(u_h-I^{\omega_n^+}u_h)^2\,dx,\end{aligned}\tag{II.35}$$

where $g=f_h+\mathrm{div}(\sigma(I^{\omega_n}u_h))$, $I^{\omega_n}u_h=I^{\omega_n^+}u_h$ in ω_n.

Applying eigenvalue problem (II.20), we obtain

$$\begin{aligned}&\int_{\omega_n^+}(\lambda+2\mu)|\nabla\chi_n^+|^2(u_h-I^{\omega_n^+}u_h)^2\,dx\\ \preceq&\frac{1}{\xi_{L_n+1}^{\omega_n}}\int_{\omega_n}\left(2\mu\epsilon(u_h-I^{\omega_n}u_h):\epsilon(u_h-I^{\omega_n}u_h)+\lambda(\nabla\cdot(u_h-I^{\omega_n}u_h))^2\right)\,dx.\end{aligned}\tag{II.36}$$

Using the definition of interpolation $I^{\omega_n^+}u_h$ and inequality (II.36), we have

$$
\begin{aligned}
&\sum_{n=1}^{N_s}\int_{\omega_n}(\lambda+2\mu)|\nabla\chi_n|^2(u_h-I^{\omega_n}u_h)^2\,dx\\
\preceq&\sum_{n=1}^{N_s}\int_{\omega_n^+}(\lambda+2\mu)|\nabla\chi_n^+|^2(u_h-I^{\omega_n^+}u_h)^2\,dx\\
\preceq&\sum_{n=1}^{N_s}\frac{1}{\xi_{L_n+1}^{\omega_n}}\int_{\omega_n}\left(2\mu\epsilon(u_h-I^{\omega_n}u_h):\epsilon(u_h-I^{\omega_n}u_h)+\lambda(\nabla\cdot(u_h-I^{\omega_n}u_h))^2\right)\,dx\\
\preceq&\sum_{n=1}^{N_s}\frac{1}{\xi_{L_n+1}^{\omega_n}}\int_{\omega_n^+}2\mu|\nabla\chi_n^+|^2\epsilon(u_h-I^{\omega_n^+}u_h):\epsilon(u_h-I^{\omega_n^+}u_h)\,dx\\
&+\lambda|\nabla\chi_n^+|^2(\nabla\cdot(u_h-I^{\omega_n^+}u_h))^2\,dx\\
\preceq&\sum_{n=1}^{N_s}\frac{1}{\xi_{L_n+1}^{\omega_n}}\int_{\omega_n^+}(\lambda+2\mu)|\nabla\chi_n^+|^2(u_h-I^{\omega_n^+}u_h)^2\,dx\\
&+\sum_{n=1}^{N_s}\frac{1}{\xi_{L_n+1}^{\omega_n}}|\int_{\omega_n^+}|\chi_n^+|^2g\cdot(u_h-I^{\omega_n^+}u_h)\,dx|\\
\preceq&\frac{1}{\Lambda_*^+}\sum_{n=1}^{N_s}\int_{\omega_n^+}(\lambda+2\mu)|\nabla\chi_n^+|^2(u_h-I^{\omega_n^+}u_h)^2\,dx\\
&+\frac{1}{\Lambda_*^+}\sum_{n=1}^{N_s}|\int_{\omega_n^+}|\chi_n^+|^2g\cdot(u_h-I^{\omega_n^+}u_h)\,dx|\\
\preceq&\frac{1}{\Lambda_*^+}\sum_{n=1}^{N_s}\frac{1}{\xi_{L_n+1}^{\omega_n}}\int_{\omega_n}\left(2\mu\epsilon(u_h-I^{\omega_n}u_h):\epsilon(u_h-I^{\omega_n}u_h)\right.\\
&\left.+\lambda(\nabla\cdot(u_h-I^{\omega_n}u_h))^2\right)\,dx+\frac{1}{\Lambda_*^+}\sum_{n=1}^{N_s}|\int_{\omega_n^+}|\chi_n^+|^2g\cdot(u_h-I^{\omega_n^+}u)\,dx|,
\end{aligned}
\tag{II.37}
$$

where $\Lambda_*^+=\min_{\omega_n}\xi_{L_n+1}^{\omega_n}$.

Applying the last inequality m times with (II.36), we get

$$\begin{aligned}
&\sum_{n=1}^{N_s}\int_{\omega_n^+}(\lambda+2\mu)|\nabla\chi_n^+|^2(u_h-I^{\omega_n^+}u_h)^2\ dx\\
\preceq&\big(\frac{1}{\Lambda_*^+}\big)^m\frac{1}{\xi_{L_n+1}^{\omega_n}}\sum_{n=1}^{N_s}\int_{\omega_n}\left(2\mu\epsilon(u_h-I^{\omega_n}u_h):\epsilon(u_h-I^{\omega_n}u_h)+\lambda(\nabla\cdot(u_h-I^{\omega_n}u_h))^2\right)\ dx\\
&+\sum_{l=1}^{m}\big(\frac{1}{\Lambda_*^+}\big)^l\sum_{n=1}^{N_s}|\int_{\omega_n^+}|\chi_n^+|^2g\cdot(u_h-I^{\omega_n^+}u_h)\ dx|\\
\preceq&\big(\frac{1}{\Lambda_*^+}\big)^{m+1}\sum_{n=1}^{N_s}\int_{\omega_n}\left(2\mu\epsilon(u_h-I^{\omega_n}u_h):\epsilon(u_h-I^{\omega_n}u_h)+\lambda(\nabla\cdot(u_h-I^{\omega_n}u_h))^2\right)\ dx\\
&+(\Lambda_*^+)^m\left(\frac{1-(\Lambda_*^+)^{-m}}{\Lambda_*^+-1}\right)\sum_{n=1}^{N_s}\int_{\omega_n^+}((\lambda+2\mu)|\nabla\chi_n^+|^2)^{-1}g^2\ dx.
\end{aligned}\tag{II.38}$$

Using Cea's lemma and inequality (II.32) , we have

$$\begin{aligned}
&\int_D\left(2\mu\epsilon(u_h-u_H):\epsilon(u_h-u_H)+\lambda(\nabla\cdot(u_h-u_H))^2\right)\ dx\\
\preceq&\sum_{n=1}^{N_s}\int_{\omega_n}(\lambda+2\mu)|\nabla\chi_n|^2(u_h-I^{\omega_n}u_h)^2\ dx+\sum_{n=1}^{N_s}|\int_{\omega_n}\chi_n^2g\cdot(u_h-I^{\omega_n}u_h)\ dx|\\
\preceq&\big(\frac{1}{\Lambda_*^+}\big)^{m+1}\int_D\left(2\mu\epsilon(u_h):\epsilon(u_h)+\lambda(\nabla\cdot u_h)^2\right)\ dx+\left((\Lambda_*^+)^m\left(\frac{1-(\Lambda_*^+)^{-m}}{\Lambda_*^+-1}\right)+1\right)R.
\end{aligned}\tag{II.39}$$

where $R=\sum_{n=1}^{N_s}\int_{\omega_n^+}((\lambda+2\mu)|\nabla\chi_n^+|^2)^{-1}g^2\ dx$.

Therefore, similar with the no oversampling case, we have

Theorem II.5.3. *Let $u_h\in V_{CG}^h$ be the fine-scale CG-FEM solution defined in (II.3) and u_H be the CG-GMsFEM solution defined in (II.6) with oversampling. If $\Lambda_*^+>1$ and*

$\int_D (\lambda + 2\mu)^{-1} g^2 \, dx \preceq 1$, *let* $n = -\frac{\log(H)}{\log \Lambda_*^+}$, *then*

$$\begin{aligned} &\int_D \left(2\mu\epsilon(u_h - u_H) : \epsilon(u_h - u_H) + \lambda(\nabla \cdot (u_h - u_H))^2\right) \, dx \\ &\preceq \left(\frac{H}{\Lambda_*^+}\right) \left(\int_D \left(2\mu\epsilon(u_h) : \epsilon(u_h) + \lambda(\nabla \cdot u_h)^2\right) \, dx + 1\right). \end{aligned}$$

II.6 Error estimate for DG coupling

In this section, we will analyze the DG coupling of the GMsFEM (II.7). For any u, we define the DG-norm by

$$\|u\|_{\text{DG}}^2 = a_H(u,u) + \sum_{E \in \mathcal{E}_H} \frac{\gamma}{h} \int_E \{\lambda + 2\mu\} [\![u]\!]^2 \, ds.$$

Let K be a coarse grid block and let $n_{\partial K}$ be the unit outward normal vector on ∂K. We denote $V^h(\partial K)$ by the restriction of the conforming space V^h on ∂K. The normal flux $\sigma(u)\, n_{\partial K}$ is understood as an element in $V^h(\partial K)$ and is defined by

$$\int_{\partial K} (\sigma(u)\, n_{\partial K}) \cdot v \, ds = \int_K \left(2\mu\epsilon(u) : \epsilon(\widehat{v}) + \lambda \nabla \cdot u \nabla \cdot \widehat{v}\right) dx, \quad v \in V^h(\partial K), \tag{II.40}$$

where $\widehat{v}$ is the harmonic extension of v in K. By the Cauchy-Schwarz inequality,

$$\int_{\partial K} (\sigma(u)\, n_{\partial K}) \cdot v \, ds \leq a_H^K(u,u)^{\frac{1}{2}} \, a_H^K(\widehat{v},\widehat{v})^{\frac{1}{2}}.$$

By an inverse inequality and the fact that $\widehat{v}$ is the harmonic extension of v

$$a_H^K(\widehat{v},\widehat{v}) \leq \kappa_K C_{\text{inv}}^2 h^{-1} \int_{\partial K} |v|^2 \, dx, \tag{II.41}$$

where $\kappa_K = \max_K\{\lambda + 2\mu\}$ and $C_{\text{inv}} > 0$ is the constant from inverse inequality. Thus,

$$\int_{\partial K} (\sigma(u)\, n_{\partial K}) \cdot v \; ds \leq \kappa_K^{\frac{1}{2}} C_{\text{inv}} h^{-\frac{1}{2}} \|v\|_{L^2(\partial K)}\, a_H^K(u,u)^{\frac{1}{2}}.$$

This shows that

$$\int_{\partial K} |\sigma(u)\, n_{\partial K}|^2 \; ds \leq \kappa_K C_{\text{inv}}^2 h^{-1} a_H^K(u,u). \tag{II.42}$$

Our first step in the convergence analysis is to establish the continuity and the coercivity of the bilinear form (II.8) with respect to the DG-norm.

Lemma II.6.1. *Assume that the penalty parameter γ is chosen so that $\gamma > 2C_{\text{inv}}^2$. The bilinear form a_{DG} defined in (II.8) is continuous and coercive, that is,*

$$a_{DG}(u,v) \;\leq\; \|u\|_{DG}\, \|v\|_{DG}, \tag{II.43}$$

$$a_{DG}(u,u) \;\geq\; a_0 \|u\|_{DG}^2, \tag{II.44}$$

for all u, v, where $a_0 = 1 - \sqrt{2} C_{\text{inv}} \gamma^{-\frac{1}{2}} > 0$.

Proof. By the definition of a_{DG}, we have

$$\begin{aligned} a_{\text{DG}}(u,v) =& a_H(u,v) - \sum_{E \in \mathcal{E}^H} \int_E \Big(\{\sigma(u)\, n_E\} \cdot [\![v]\!] + \{\sigma(v)\, n_E\} \cdot [\![u]\!] \Big) \; ds \\ &+ \sum_{E \in \mathcal{E}^H} \frac{\gamma}{h} \int_E \{\lambda + 2\mu\} [\![u]\!] \cdot [\![v]\!] \; ds. \end{aligned}$$

Notice that

$$a_H(u,v) + \sum_{E \in \mathcal{E}^H} \frac{\gamma}{h} \int_E \{\lambda + 2\mu\} [\![u]\!] \cdot [\![v]\!] \; ds \leq \|u\|_{\text{DG}}\, \|v\|_{\text{DG}}.$$

For an interior coarse edge $E \in \mathcal{E}^H$, we let $K^+, K^- \in \mathcal{T}^H$ be the two coarse grid blocks

having the edge E. By the Cauchy-Schwarz inequality, we have

$$\int_E \{\sigma(u)\, n_E\} \cdot [\![v]\!]\, ds \le \Big(h \int_E \{\sigma(u)\, n_E\}^2 \{\lambda + 2\mu\}^{-1}\, ds\Big)^{\frac{1}{2}} \Big(\frac{1}{h} \int_E \{\lambda + 2\mu\} [\![v]\!]^2\, ds\Big)^{\frac{1}{2}}. \tag{II.45}$$

Notice that

$$\begin{aligned} & h \int_E \{\sigma(u)\, n_E\}^2 \{\lambda + 2\mu\}^{-1}\, ds \\ & \le h\Big(\int_E (\sigma(u^+)\, n_E)^2 (\lambda^+ + 2\mu^+)^{-1}\, ds + \int_E (\sigma(u^-)\, n_E)^2 (\lambda^- + 2\mu^-)^{-1}\, ds \Big), \end{aligned}$$

where $u^\pm = u|_{K^\pm}$, $\lambda^\pm = \lambda|_{K^\pm}$ and $\mu^\pm = \mu|_{K^\pm}$. So, we have

$$h \int_E \{\sigma(u)\, n_E\}^2 \{\lambda + 2\mu\}^{-1}\, ds \le C_{\text{inv}}^2 \Big(a_H^{K^+}(u^+, u^+) + a_H^{K^-}(u^-, u^-) \Big).$$

Thus (II.45) becomes

$$\int_E \{\sigma(u)\, n_E\} \cdot [\![v]\!]\, ds \le C_{\text{inv}} \Big(a_H^{K^+}(u^+, u^+) + a_H^{K^-}(u^-, u^-) \Big)^{\frac{1}{2}} \Big(\frac{1}{h} \int_E \{\lambda + 2\mu\} [\![v]\!]^2\, ds\Big)^{\frac{1}{2}}. \tag{II.46}$$

When E is a boundary edge, we have

$$\int_E \{\sigma(u)\, n_E\} \cdot [\![v]\!]\, ds \le C_{\text{inv}} a_H^K(u, u)^{\frac{1}{2}} \Big(\frac{1}{h} \int_E \{\lambda + 2\mu\} [\![v]\!]^2\, ds\Big)^{\frac{1}{2}}, \tag{II.47}$$

where K denotes the coarse grid block having the edge E. Summing (II.46) and (II.47) for all edges $E \in \mathcal{E}^H$, we have

$$\sum_{E \in \mathcal{E}^H} \int_E \{\sigma(u)\, n_E\} \cdot [\![v]\!]\, ds \le \sqrt{2} C_{\text{inv}} a_H(u, u)^{\frac{1}{2}} \Big(\sum_{E \in \mathcal{E}^H} \frac{1}{h} \int_E \{\lambda + 2\mu\} [\![v]\!]^2\, ds \Big)^{\frac{1}{2}}.$$

Similarly, we have

$$\sum_{E\in\mathcal{E}^H}\int_E \{\sigma(v)\,n_E\}\cdot[\![u]\!]\,ds \le \sqrt{2}C_{\text{inv}}a_H(v,v)^{\frac{1}{2}}\Big(\sum_{E\in\mathcal{E}^H}\frac{1}{h}\int_E\{\lambda+2\mu\}[\![u]\!]^2\,ds\Big)^{\frac{1}{2}}.$$

Hence

$$\sum_{E\in\mathcal{E}^H}\int_E\Big(\{\sigma(u)\,n_E\}\cdot[\![v]\!]+\{\sigma(v)\,n_E\}\cdot[\![u]\!]\Big)\,ds \le \sqrt{2}C_{\text{inv}}\gamma^{-\frac{1}{2}}\|u\|_{\text{DG}}\,\|v\|_{\text{DG}}. \quad \text{(II.48)}$$

This proves the continuity.

For coercivity, we have

$$a_{\text{DG}}(u,u) = \|u\|^2_{\text{DG}} - \sum_{E\in\mathcal{E}^H}\int_E\Big(\{\sigma(u)\,n_E\}\cdot[\![u]\!]+\{\sigma(u)\,n_E\}\cdot[\![u]\!]\Big)\,ds.$$

By (II.48), we have

$$a_{\text{DG}}(u,u) \ge (1-\sqrt{2}C_{\text{inv}}\gamma^{-\frac{1}{2}})\|u\|^2_{\text{DG}},$$

which gives the desired result.

□

We will now prove the convergence of the method (II.7). Let $u_h \in V^h_{\text{DG}}$ be the fine grid solution which satisfies

$$a_{\text{DG}}(u_h,v) = (f,v), \quad \forall v\in V^h_{\text{DG}}. \quad \text{(II.49)}$$

It is well-known that u_h converges to the exact solution u in the DG-norm as the fine mesh size $h\to 0$. Next, we define a projection $u_S \in V^{\text{snap}}$ of u_h in the snapshot space by the following construction. For each coarse grid block K, the restriction of u_S on K is defined

as the harmonic extension of u_h, that is,

$$\begin{aligned} -\nabla \cdot \sigma(u_S) &= 0, \quad \text{in } K, \\ u_S &= u_h, \quad \text{on } \partial K. \end{aligned} \tag{II.50}$$

Now, we prove the following estimate for the projection u_S.

Lemma II.6.2. *Let $u_h \in V_{DG}^h$ be the fine grid solution defined in (II.49) and $u_S \in V^{snap}$ be the projection of u_h defined in (II.50). Then we have*

$$\|u_h - u_S\|_{DG} \leq CH\Big(\max_{K\in\mathcal{T}^H} \eta_K\Big)\|f\|_{L^2(\Omega)},$$

where $\eta_K = \min_K\{\lambda + 2\mu\}$.

Proof. Let K be a given coarse grid block. Since $u_S = u_h$ on ∂K, the jump terms in the DG-norm vanish. Thus, the DG-norm can be written as

$$\|u_h - u_S\|_{\text{DG}}^2 = \sum_{K\in\mathcal{T}^H} a_H^K(u_h - u_S, u_h - u_S).$$

Since u_S satisfies (II.50) and $u_h - u_S = 0$ on ∂K, we have

$$a_H^K(u_S, u_h - u_S) = 0.$$

So,

$$\|u_h - u_S\|_{\text{DG}}^2 = \sum_{K\in\mathcal{T}^H} a_H^K(u_h, u_h - u_S) = a_{\text{DG}}(u_h, u_h - u_S) = (f, u_h - u_S).$$

By the Poincare inequality, we have

$$\|u_h - u_S\|_{L^2(K)} \leq CH^2\eta_K^2 a_H^K(u_h - u_S, u_h - u_S),$$

where $\eta_K = \min_K\{\lambda + 2\mu\}$. Hence, we have

$$\|u_h - u_S\|_{\text{DG}} \leq CH\Big(\max_{K\in\mathcal{T}^H}\eta_K\Big)\|f\|_{L^2(\Omega)}.$$

□

In the following theorem, we will state and prove the convergence of the GMsFEM (II.7).

Theorem II.6.3. *Let $u_h \in V_{DG}^h$ be the fine grid solution defined in (II.49) and u_H be the GMsFEM solution defined in (II.7). Then we have*

$$\begin{aligned}\|u_h - u_H\|_{DG}^2 \leq & C\Big(\sum_{i=1}^{N_E}\frac{H}{\langle\lambda+2\mu\rangle\,\xi_{L_i+1}}(1+\frac{\gamma H}{h\xi_{L_i+1}})\int_{\partial K_i}(\sigma(u_S)\cdot n_{\partial K})^2\,ds\\ &+ H^2\Big(\max_{K\in\mathcal{T}^H}\eta_K^2\Big)\|f\|_{L^2(\Omega)}^2\Big),\end{aligned}$$

where u_S is defined in (II.50).

Proof. First, we will define a projection $\widehat{u}_S \in V^{\text{off}}$ of u_S in the offline space. Notice that, on each K_i, u_S can be represented by

$$u_S = \sum_{l=1}^{M_i} c_l\psi_l^{i,\text{off}},$$

where $M_i = M^{i,\text{snap}}$ and we assume that the functions $\psi_l^{i,\text{off}}$ are normalized so that

$$\int_{\partial K_i}\langle\lambda+2\mu\rangle\,(\psi_l^{i,\text{off}})^2\,ds = 1.$$

Then the function $\widehat{u}_S$ is defined by

$$\widehat{u}_S = \sum_{l=1}^{L_i} c_l \psi_l^{i,\text{off}}.$$

We will find an estimate of $\|u_S - \widehat{u}_S\|_{\text{DG}}$. Let K be a given coarse grid block. Recall that the spectral problem is

$$\int_K 2\mu\epsilon(u) : \epsilon(v)\, dx + \int_K \lambda \nabla \cdot u \nabla \cdot v\, dx = \frac{\xi}{H} \int_{\partial K} \langle \lambda + 2\mu \rangle\, uv\, ds.$$

By the definition of the flux (II.40), the spectral problem can be represented as

$$\int_{\partial K} (\sigma(u) \cdot n_{\partial K}) v\, ds = \frac{\xi}{H} \int_{\partial K} \langle \lambda + 2\mu \rangle\, uv\, ds.$$

By the definition of the DG-norm, the error $\|u_S - \widehat{u}_S\|_{\text{DG}}$ can be computed as

$$\begin{aligned}\|\widehat{u}_S - u_S\|_{\text{DG}}^2 \leq \sum_K \Big(& \int_K 2\mu\epsilon(\widehat{u}_S - u_S)^2\, ds + \int_K \lambda(\nabla \cdot (\widehat{u}_S - u_S))^2\, ds \\ & + \frac{\gamma}{h} \int_{\partial K} \{\lambda + 2\mu\}(\widehat{u}_S - u_S))^2\, ds \Big).\end{aligned}$$

Note that

$$\begin{aligned}&\int_{K_i} 2\mu\epsilon(\widehat{u}_S - u_S)^2\, ds + \int_{K_i} \lambda(\nabla \cdot (\widehat{u}_S - u_S))^2\, ds \leq \frac{1}{h} \int_{\partial K_i} \langle \lambda + 2\mu \rangle\, (\widehat{u}_S - u_S)^2\, ds \\ &= \sum_{l=L_i+1}^{M_i} \frac{\xi_l}{H} c_l^2 \leq \frac{H}{\xi_{L_i+1}} \sum_{l=L_i+1}^{M_i} (\frac{\xi_l}{H})^2 c_l^2.\end{aligned}$$

Also,

$$\frac{1}{h} \int_{\partial K_i} \{\lambda + 2\mu\}(\widehat{u}_S - u_S)^2\, ds = \frac{1}{h} \sum_{l=L_i+1}^{M_i} c_l^2 \leq \frac{H^2}{h\xi_{L_i+1}^2} \sum_{l=L_i+1}^{M_i} (\frac{\xi_l}{H})^2 c_l^2.$$

Moreover,

$$\sum_{l=L_i+1}^{M_i} (\frac{\xi_l}{H})^2 c_l^2 \leq \sum_{l=1}^{M_i} (\frac{\xi_l}{H})^2 c_l^2 \leq \frac{1}{\langle \lambda + 2\mu \rangle} \int_{\partial K_i} (\sigma(u_S) \cdot n_{\partial K})^2 \, ds.$$

Consequently, we obtain the following bound

$$\|u_S - \widehat{u}_S\|_{\text{DG}}^2 \leq \sum_{i=1}^{N_E} \frac{H}{\langle \lambda + 2\mu \rangle \, \xi_{L_i+1}} (1 + \frac{\gamma H}{h \xi_{L_i+1}}) \int_{\partial K_i} (\sigma(u_S) \cdot n_{\partial K})^2 \, ds.$$

Next, we will prove the required error bound. By coercivity,

$$\begin{aligned} a_0 \|\widehat{u}_S - u_H\|_{\text{DG}}^2 &= a_{\text{DG}}(\widehat{u}_S - u_H, \widehat{u}_S - u_H) \\ &= a_{\text{DG}}(\widehat{u}_S - u_H, \widehat{u}_S - u_S) + a_{\text{DG}}(\widehat{u}_S - u_H, u_S - u_h) \\ &\quad + a_{\text{DG}}(\widehat{u}_S - u_H, u_h - u_H). \end{aligned}$$

Note that $a_{\text{DG}}(\widehat{u}_S - u_H, u_h - u_H) = 0$ since $\widehat{u} - u_H \in V^{\text{off}}$. Using the above results,

$$\begin{aligned} \|\widehat{u}_S - u_H\|_{\text{DG}}^2 \leq C \Big(& \sum_{i=1}^{N_E} \frac{H}{\langle \lambda + 2\mu \rangle \, \xi_{L_i+1}} (1 + \frac{\gamma H}{h \xi_{L_i+1}}) \int_{\partial K_i} (\sigma(u_S) \cdot n_{\partial K})^2 \, ds \\ & + H^2 \Big(\max_{K \in \mathcal{T}^H} \eta_K^2 \Big) \|f\|_{L^2(\Omega)}^2 \Big). \end{aligned} \tag{II.51}$$

Finally, the desired bound is obtained by the triangle inequality

$$\|u_h - u_H\|_{\text{DG}} \leq \|u_h - u_S\|_{\text{DG}} + \|u_S - \widehat{u}_S\|_{\text{DG}} + \|\widehat{u}_S - u_H\|_{\text{DG}}.$$

□

Remark II.6.4. *It is worthwhile to note that (II.41) can be replaced by*

$$a_H^K(\widehat{v}, \widehat{v}) \leq \Lambda_K^{\text{snap}} \, \langle \lambda + 2\mu \rangle \int_{\partial K} |v|^2 \, ds,$$

h	Λ_K^{snap}	$\Lambda_{K^+}^{\text{snap}}$
1/10	3.91e+02	19.3
1/20	7.99e+02	19.2
1/40	1.61e+03	20.4
1/80	3.22e+03	20.4

Table II.9: Largest eigenvalue for no oversampling and oversampling

where Λ_K^{snap} is the largest eigenvalue for the spectral problem (II.18). Therefore, (II.42) becomes

$$\int_{\partial K} |\sigma(u)\, n_{\partial K}|^2 \, ds \leq \Lambda_K^{\text{snap}} \langle \lambda + 2\mu \rangle \, a_H^K(u,u).$$

Repeating above steps, one can choose γ in (II.51) that satisfies

$$\gamma > \tilde{C} h \max_{K \subset \mathcal{T}^H} \Lambda_K^{\text{snap}},$$

where the constant $\tilde{C}$ is defined as

$$\tilde{C} = \max_{K \subset \mathcal{T}^H} \frac{\max_{E \subset \partial K}\{\lambda + 2\mu\}}{\min_{E \subset \partial K}\{\lambda + 2\mu\}}.$$

If we assume every coarse element includes a high contrast region, then $\tilde{C}$ is $O(1)$.

Table II.9 shows Λ_K^{snap} with and without oversampling for different h. We can see that $\Lambda_{K^+}^{\text{snap}}$ is much smaller than Λ_K^{snap}. Besides, the numerical experiments show $\Lambda_{K^+}^{\text{snap}}$ is a very weak function of h, while Λ_K^{snap} is proportional to h^{-1}.

We can get similar error analysis for the case of oversampling by just following steps shown in the above no oversampling case. But we can have better estimate in the oversampling case. If we let $\gamma = \alpha \tilde{C} \max_{K \subset \mathcal{T}^H} \Lambda_{K^+}^{\text{snap}}$, then the term $C_1 = 1 + \frac{\gamma H}{h \xi_{L_i+1}}$ in (II.51) becomes $1 + \frac{\alpha \tilde{C} \max_{K \subset \mathcal{T}^H} \Lambda_{K^+}^{\text{snap}} H}{\xi_{L_i+1}}$. We have numerically shown that $\Lambda_{K^+}^{\text{snap}}$ is almost independent of h, which means C_1 can be controlled. Therefore, the dominated error comes from

$\frac{H}{\langle\lambda+2\mu\rangle\xi_{L_i+1}}$. *We emphasize that this remark is based on our numerical observations while the analytical studies are complicated and it will be the subject of our future research.*

II.7 Concluding remarks

We design a multiscale model reduction method using GMsFEM for second-order formulation of elasticity equations in heterogeneous media. We design a snapshot space and an offline space based on the analysis. We present two approaches that couple multiscale basis functions of the offline space. These are continuous Galerkin and discontinuous Galerkin methods. Both approaches are analyzed. We present oversampling studies where larger domains are used for calculating the snapshot space. Numerical results are presented.

III. GENERALIZED MULTISCALE FINITE ELEMENT METHODS FOR FIRST-ORDER LINEAR ELASTICITY EQUATION

III.1 Introduction

Previous chapters are devoted to reduce the linear elasticity system in the second order formulation. In this chapter, we will study the reduction for the first-order formulation of the linear elasticity system, where the stress tensor is one of the unknowns. The motivation of using a mixed formulation is to preserve energy and mass conservation which is important for elastic wave simulations and geomechanical applications [16, 63]. Another important advantage of mixed formulation is its robustness for nearly incompressible materials. One can also directly compute the stress tensor, which is often the focus of interest in some engineer problems [66].

It is well-known that the solution of second-order displacement formulation of the elasticity system will deteriorate (the so-called locking effect [17, 11]) for the nearly incompressible material. Methods based on mixed formulations provide good alternatives as they can overcome the problem of locking. Classical mixed methods for the linear elasticity problems are reported in [8, 17, 76, 18, 40, 7, 51, 50, 47]. The main disadvantage of these mixed methods is that they have too many degrees of freedom, or the resulting linear system is not symmetric positive definite and thus difficult to solve (see detailed description in [47]). Some of these methods require regular or uniform grids which make them fail to handle the case of irregular domain. Recently proposed Hybridizable Discontinuous Galerkin (HDG) method [31] has shown a promising ability to reduce the degrees of freedom of many problems like the mixed formulation of the elliptic problem, this method also allows non-conforming and irregular grids, and domain decomposition formulation, the resulting linear system is symmetric positive definite or nearly symmetric positive def-

inite. The literature of applying HDG method for the linear elasticity problem can be seen in [72, 32].

Our goal here is to design multiscale model reduction techniques for the linear elasticity problems in highly heterogeneous media within the framework of HDG method. To achieve this, we use the domain decomposition formulation of the HDG method, the entire problem can be decomposed by solving a small dimension global problem and some independent local problems on each coarse element. The global problem are defined on numerical trace space that lives in the coarse elements interface. The standard choice for the numerical trace space is the polynomial functions, however, polynomial only works very well for the case that media property is smooth along the interfaces. It is quite necessary to construct multiscale numerical trace space that can capture the local information of arbitrary heterogeneous media and thus reduce the dimension of the trace space. We will introduce several multiscale spaces for the *numerical trace* that can represent the solution with fewer degrees of freedom. We will show the efficiency and robustness of our methods with various numerical examples.

This chapter is arranged in the following. In Section III.2, we first describe the model problem and the coarse and fine discretizations of the domain, and then present the framework of HDG-GMsFEM for the mixed linear elasticity system, followed by the description of the domain decomposition method. In Section III.3, we introduce three ways of constructing the multiscale basis functions. Numerical examples are given in Section III.4, and conclusions are made in the last section.

III.2 Preliminaries

In this section, we will describe the model problem and gird generation. In addition, we will present the formulations of a fine-scale HDG discretization of the first-order linear elasticity system and its domain decomposition formulation.

III.2.1 Model problem

Let Ω be a polygonal open subset of $\mathbb{R}^2$. Consider the linear elasticity system in the mixed form

$$\mathcal{A}\underline{\sigma} + \underline{\epsilon}(u) = 0 \quad \text{in } \Omega \subset \mathbb{R}^2, \tag{III.1a}$$

$$\nabla \cdot \underline{\sigma} = f \quad \text{in } \Omega, \tag{III.1b}$$

$$u = 0 \quad \text{on } \partial\Omega, \tag{III.1c}$$

Here, u represents the displacement filed, the strain tensor is again represented by $\underline{\epsilon}(u) := \frac{1}{2}(\nabla u + (\nabla u)^\top)$. The stress tensor is represented by $\underline{\sigma} : \Omega \mapsto S$, where S denotes the set of all symmetric matrices in $\mathbb{R}^{2\times 2}$. The compliance tensor $\mathcal{A}$ is assumed to be a bounded, symmetric, positive definite tensor over S. $\mathcal{A}\underline{\sigma} = \overline{\lambda} tr(\underline{\sigma})\delta + \overline{\mu}\underline{\sigma}$, $\overline{\lambda}$ and $\overline{\mu}$ are elastic parameters, their relationships with Lamé parameter λ and μ are

$$\mu = \frac{1}{2\overline{\mu}} \tag{III.2a}$$

$$\lambda = -\frac{\overline{\lambda}}{4\overline{\mu}(\overline{\lambda} + \overline{\mu})} \tag{III.2b}$$

$f \in \boldsymbol{L}^2(\Omega)$, $g \in \boldsymbol{H}^{1/2}(\partial\Omega)$.

III.2.2 Fine and coarse grids

The HDG-GMsFEM method for the system (III.1) relies on a two-scale grid. Let Ω be divided into non-overlapping polygonal coarse blocks K_i with diameter H_i so that $\overline{\Omega} = \cup_{i=1}^{N_E} \overline{K}_i$, where N_E is the total number of coarse blocks. The decomposition of the domain can be nonconforming. We call E_H a coarse edge of the coarse block K_i if $E_H = \partial K_i \cap \partial K_j$ or $E_H = \partial K_i \cap \partial\Omega$. Let $\mathcal{E}_H(K_i)$ be the set of all coarse edges on the boundary of the coarse block K_i, and let $\mathcal{E}_H = \cup_{i=1}^{N} \mathcal{E}_H(K_i)$ be the set of all coarse edges

and $\mathcal{E}_H^0$ be the set of all interior coarse edges. N_v is the total number of coarse grid nodes.

We further partition each each coarse block K_i into a finer mesh with mesh size h_i. Let $\mathcal{T}_h = \cup_{i=1}^N \mathcal{T}_h(K_i)$ be the union of all these triangulations, which is a fine mesh triangulation of the domain Ω. We use $h = \max_{1\leq i\leq n} h_i$ to denote the mesh size of $\mathcal{T}_h$. In addition, we let $\mathcal{E}_h(K_i)$ be the set of all edges of the triangulation $\mathcal{T}_h(K_i)$ and $\mathcal{E}_h^0(K_i)$ be the set of all interior edges of the triangulation $\mathcal{T}_h(K_i)$ and let $\mathcal{E}_h = \cup_{i=1}^N \mathcal{E}_h(K_i)$ be the set of all edges in the triangulation $\mathcal{T}_h$. We also denote $\mathcal{E}_h^0 = \cup_{i=1}^N \mathcal{E}_h^0(K_i)$ as the set of all fine-scale interior edges. Figure III.1 gives an illustration of the constructions of the two grids. The red lines represent the coarse grid, and the black lines represent the fine grid. For each coarse edge E_i, we define a coarse neighborhood ω_i as the union of all coarse blocks having the edge E_i. Figure III.1 shows a coarse neighborhood ω_i in yellow color.

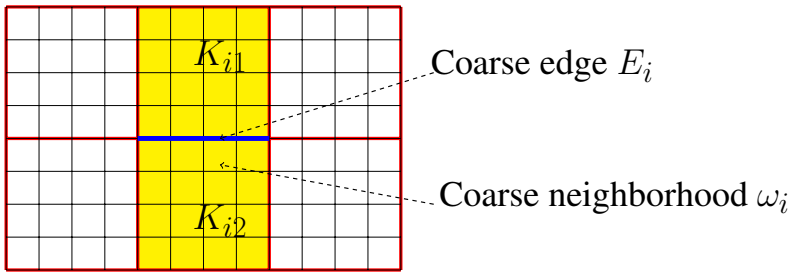

Figure III.1: Illustration of the coarse and fine grids and a coarse neighborhood ω_i subordinated to a coarse edge.

III.2.3 HDG-GMsFEM for elasticity equation

The methods we are interested in seek an approximation to $(u, q, u|_{\mathcal{E}_h})$ by the hybridized discontinuous Galerkin finite element method. For this purpose, using the two-

scale grid defined in the last subsection, we define the following finite element spaces:

$$
\begin{aligned}
\underline{\boldsymbol{V}}_h &:= \{v \in \underline{\boldsymbol{L}}^2(\mathcal{T}_h): \quad v|_K \in \underline{\boldsymbol{V}}(K) \quad \forall\, K \in \mathcal{T}_h\},\\
\boldsymbol{W}_h &:= \{\omega \in \boldsymbol{L}^2(\mathcal{T}_h): \quad \omega|_K \in \boldsymbol{W}(K) \quad \forall\, K \in \mathcal{T}_h\},\\
\boldsymbol{M}_h &:= \{\mu \in L^2(\mathcal{E}_h): \ \text{ for } F \in \mathcal{E}_h^0 \ \ \mu|_F \in \boldsymbol{M}_h(F), \ \text{ and } \ \mu|_{\partial\Omega} = 0\},\\
\boldsymbol{M}_h^0 &:= \{\mu \in L^2(\mathcal{E}_h): \ \text{ for } F \in \mathcal{E}_h^0 \ \ \mu|_F \in \boldsymbol{M}_h(F), \ \text{ and } \ \mu|_{\mathcal{E}_H} = 0\},\\
\boldsymbol{M}_H &:= \{\mu \in L^2(\mathcal{E}_{h,H}): \ \text{ for } F \in \mathcal{E}_H \ \ \mu|_F \in \boldsymbol{M}_H(F), \quad \text{and } \mu|_{\mathcal{E}_h^0 \cup \partial\Omega} = 0\}.\\
\boldsymbol{M}_{h,H} &:= \boldsymbol{M}_h^0 \oplus \boldsymbol{M}_H.
\end{aligned}
$$

Then the multiscale HDG finite element method can be read as: find $(u_h, \underline{\sigma}_h, \widehat{u}_{h,H})$ in the space $\boldsymbol{W}_h \times \underline{\boldsymbol{V}}_h \times \boldsymbol{M}_{h,H}$ that satisfies the following weak problem

$$
\begin{aligned}
(\mathcal{A}\underline{\sigma}_h\,,\,\underline{v})_{\mathcal{T}_h} - (u_h\,,\,\nabla\cdot\underline{v})_{\mathcal{T}_h} + \langle \widehat{u}_{h,H}\,,\,\underline{v}n\rangle_{\partial\mathcal{T}_h} &= 0, && \text{(III.3a)}\\
(\underline{\sigma}_h\,,\,\nabla\omega)_{\mathcal{T}_h} - \langle \widehat{\underline{\sigma}}_{h,H}n\,,\,\omega\rangle_{\partial\mathcal{T}_h} &= -(f\,,\,\omega)_{\mathcal{T}_h}, && \text{(III.3b)}\\
\langle \widehat{\underline{\sigma}}_{h,H}n\,,\,\mu\rangle_{\partial\mathcal{T}_h(T)} &= 0, && \text{(III.3c)}\\
\langle \widehat{u}_{h,H}\,,\,\mu\rangle_{\partial D} &= \langle \widehat{0}\,,\,\mu\rangle_{\partial D}, && \text{(III.3d)}
\end{aligned}
$$

for all $(v, \omega, \mu) \in \underline{\boldsymbol{V}}_h \times \boldsymbol{W}_h \times \boldsymbol{M}_{h,H}$, where

$$
\widehat{\underline{\sigma}}_{h,H}n = \underline{\sigma}_h n + \tau(P_M u_h - \widehat{u}_{h,H}) \quad \text{on } \partial\mathcal{T}_h. \tag{III.3e}
$$

Here, P_M denotes the standard L^2-orthogonal projection from $\boldsymbol{L}^2(\mathcal{E}_h)$ onto $\boldsymbol{M}_h$. We write $(\underline{\eta}\,,\,\underline{\zeta})_{\mathcal{T}_h} := \sum_{i,j=1}^2 (\underline{\eta}_{i,j}\,,\,\underline{\zeta}_{i,j})_{\mathcal{T}_h}$, $(\eta\,,\,\zeta)_{\mathcal{T}_h} := \sum_{i=1}^2 (\eta_i\,,\,\zeta_i)_{\mathcal{T}_h}$, and $(\eta\,,\,\zeta)_{\mathcal{T}_h} := \sum_{K\in\mathcal{T}_h}(\eta,\zeta)_K$, where $(\eta,\zeta)_D$ denotes the integral of $\eta\zeta$ over $D \subset \mathbb{R}^2$. Similarly, we write $\langle \eta\,,\,\zeta\rangle_{\partial\mathcal{T}_h} := \sum_{i=1}^n \langle \eta_i\,,\,\zeta_i\rangle_{\partial\mathcal{T}_h}$ and $\langle \eta\,,\,\zeta\rangle_{\partial\mathcal{T}_h} := \sum_{K\in\mathcal{T}_h}\langle \eta\,,\,\zeta\rangle_{\partial K}$, where $\langle \eta\,,\,\zeta\rangle_D$

denotes the integral of $\eta\zeta$ over $D \subset \mathbb{R}^1$.

On each $K \in \mathcal{T}_h$, the stabilization parameter τ is non-negative constant on each $F \in \partial K$ and we assume that $\tau > 0$ on at least one face $F^* \in \partial K$. By taking particular choices of the local spaces $\underline{\boldsymbol{V}}(K)$, $\boldsymbol{W}(K)$ and $\boldsymbol{M_h}(F)$, and the *linear local stabilization* operator τ, various HDG methods are obtained [72, 32]. Here we use the finite element space introduced in [72] to form space $\underline{\boldsymbol{V}}(K)$, $\boldsymbol{W}(K)$ and $\boldsymbol{M}_h(F)$ for $K \in \mathcal{T}_h$. The focus of this chapter is the construction of multiscale basis to fill $\boldsymbol{M}_H$.

III.2.4 Domain decomposition formulation

The main feature of this method is that it could be implemented by just solving a global system on the coarse edges $\mathcal{E}_H$ together with the solutions of some local problems. To achieve this, we split (III.3c) into two equations by testing separately with $\mu \in \boldsymbol{M}_h^0$ and $\mu \in \boldsymbol{M}_H$ so that

$$\langle \widehat{\underline{\sigma}}_{h,H} n, \mu \rangle_{\partial \mathcal{T}_h} = 0 \ \ \forall \mu \in \boldsymbol{M}_h^0 \quad \text{and} \quad \langle \widehat{\underline{\sigma}}_{h,H} n, \mu \rangle_{\partial K_i} = 0 \ \ \forall \mu \in \boldsymbol{M}_H \ \text{and} \ i = 1, \ldots, N_E. \tag{III.4}$$

On any subdomain T, given the boundary data of $\widehat{u}_{h,H} = \xi_H$ for $\xi_H \in \boldsymbol{M}_H(F), F \in \mathcal{E}_H(T)$, we can solve for $(\underline{\sigma}_h, u_h, \widehat{u}_{h,H})|_T$ by restricting the equations (III.3a)–(III.3c) on this particular subdomain T:

$$(\mathcal{A}\underline{\sigma}_h \, , \, \underline{v})_{\mathcal{T}_h(T)} - (u_h \, , \, \nabla \cdot \underline{v})_{\mathcal{T}_h(T)} + \langle \widehat{u}_{h,H} \, , \, \underline{v} n \rangle_{\partial \mathcal{T}_h(T)} = 0, \tag{III.5}$$

$$(\underline{\sigma}_h \, , \, \nabla \omega)_{\mathcal{T}_h(T)} - \langle \widehat{\underline{\sigma}}_{h,H} n \, , \, \omega \rangle_{\partial \mathcal{T}_h(T)} = -(f \, , \, \omega)_{\mathcal{T}_h(T)}, \tag{III.6}$$

$$\langle \widehat{\underline{\sigma}}_{h,H} n \, , \, \mu \rangle_{\partial \mathcal{T}_h(T)} = 0, \tag{III.7}$$

$$\widehat{u}_{h,H} = \xi_H \quad \text{on } \partial T, \tag{III.8}$$

for all $(w, \underline{v}, \mu) \in \boldsymbol{W}_h|_T \times \underline{\boldsymbol{V}}_h|_T \times \boldsymbol{M}_h^0|_{\mathcal{E}_h^0(T)}$. Here again we have $\widehat{\underline{\sigma}}_{h,H} n = \underline{\sigma}_h n + \tau(P_M u_h - \widehat{u}_{h,H})$ on $\partial\mathcal{T}_h(T)$. In fact the above local system is the regular HDG methods defined on T. From [72] we already know that this system is stable. Hence, this HDG solver defines a global *affine* mapping from $\boldsymbol{M}_H$ to $\boldsymbol{W}_h \times \underline{\boldsymbol{V}}_h \times \boldsymbol{M}_h^0$. The solution can be further split into two parts, namely,

$$(\underline{\sigma}_h, u_h, \widehat{u}_{h,H}) = (\underline{\sigma}_h(f), u_h(f), \widehat{u}_{h,H}(f)) + (\underline{\sigma}_h(\xi_H), u_h(\xi_H), \widehat{u}_{h,H}(\xi_H))$$

where $(\underline{\sigma}_h(f), u_h(f), \widehat{u}_{h,H}(f))$ satisfies

$$\begin{aligned}
(\mathcal{A}\underline{\sigma}_h(f)\,,\,\underline{v})_{\mathcal{T}_h(T)} - (u_h(f)\,,\,\nabla\cdot\underline{v})_{\mathcal{T}_h(T)} + \langle\widehat{u}_{h,H}(f)\,,\,\underline{v}n\rangle_{\partial\mathcal{T}_h(T)} &= 0,\\
(\underline{\sigma}_h(f)\,,\,\nabla\omega)_{\mathcal{T}_h(T)} - \langle\widehat{\underline{\sigma}}_{h,H}(f)n\,,\,\omega\rangle_{\partial\mathcal{T}_h(T)} &= -(f\,,\,\omega)_{\mathcal{T}_h(T)},\\
\langle\widehat{\underline{\sigma}}_{h,H}(f)n\,,\,\mu\rangle_{\partial\mathcal{T}_h(T)} &= 0,\\
\widehat{u}_{h,H}(f) &= 0 \quad \text{on } \partial T,
\end{aligned}$$

for all $(w, \underline{v}, \mu) \in \boldsymbol{W}_h|_T \times \underline{\boldsymbol{V}}_h|_T \times \boldsymbol{M}_h^0|_{\mathcal{E}_h^0(T)}$ and $(\underline{\sigma}_h(\xi_H), u_h(\xi_H), \widehat{u}_{h,H}(\xi_H))$ satisfies

$$\begin{aligned}
(\mathcal{A}\underline{\sigma}_h(\xi_H)\,,\,v)_{\mathcal{T}_h(T)} - (u_h(\xi_H)\,,\,\nabla\cdot v)_{\mathcal{T}_h(T)} + \langle\widehat{u}_{h,H}(\xi_H)\,,\,vn\rangle_{\partial\mathcal{T}_h(T)} &= 0,\\
(\underline{\sigma}_h(\xi_H)\,,\,\nabla\omega)_{\mathcal{T}_h(T)} - \langle\widehat{\underline{\sigma}}_{h,H}(\xi_H)n\,,\,\omega\rangle_{\partial\mathcal{T}_h(T)} &= 0,\\
\langle\widehat{\underline{\sigma}}_{h,H}(\xi_H)n\,,\,\omega\rangle_{\partial\mathcal{T}_h(T)} &= 0,\\
\widehat{u}_{h,H}(\xi_H) &= \xi_H \quad \text{on } \partial T,
\end{aligned}$$

for all $(w, v, \mu) \in \boldsymbol{W}_h|_T \times \underline{\boldsymbol{V}}_h|_T \times \boldsymbol{M}_h^0|_{\mathcal{E}_h^0(T)}$

Then the second equation (III.4) reduces to

$$a(\xi_H, \mu) = l(\mu) \qquad \text{for all } \mu \in \boldsymbol{M}_H, \tag{III.9}$$

where the bilinear form $a(\xi_H, \mu) : \boldsymbol{M}_H \times \boldsymbol{M}_H \to R$ and the linear form $l(\mu) : \boldsymbol{M}_H \to R$ are defined as

$$a(\xi_H, \mu) := -\langle \widehat{\underline{\sigma}}_{h,H}(\xi_H) \cdot n \,,\, \mu \rangle_{\partial \mathcal{T}_H} \quad \text{and} \quad l(\mu) := a(f, \mu) = \langle \widehat{\underline{\sigma}}_{h,H}(f) \cdot n \,,\, \mu \rangle_{\partial \mathcal{T}_H}. \tag{III.10}$$

We note that similar procedure can be applied for other types of boundary conditions. We can apply direct solver to solve the linear system resulting from $a(\cdot, \cdot)$ and $l(\cdot)$. On the other hand, $\boldsymbol{M}_H$ in (III.9) is not accurate enough for problems with high contrast heterogeneous media if it contains only polynomial basis functions. Thus, in the next section, we will discuss the construction of multiscale basis functions.

III.3 Construction of the multiscale space $\boldsymbol{M}_H$

In this section, we propose three different multiscale space $\boldsymbol{M}_H$. We remark that if the media is smooth across the coarse block interface, polynomial space is a good choice for $\boldsymbol{M}_H$. We first clarify some notations about the grids. Suppose E_i is a local coarse edge, let x_{i1} and x_{i2} be the coarse nodes that lies on the two ends of E_i. For each coarse node x_i, we say the union of coarse blocks that include x_i is the coarse neighborhood that associated with x_i. Therefore, for x_{i1} and x_{i2} we have two corresponding coarse neighborhoods Ω_{i1} and Ω_{i2} that associated with them respectively. Figure III.2 shows x_{i1} and its coarse neighborhood Ω_{i1}. We also define ω_i as the coarse neighborhood that subordinated to the coarse edge E_i, which is the union of the two adjacent coarse blocks K_{i1} and K_{i2} that include E_i (see FigureIII.1). We note here that the neighborhood associated with a coarse node and the neighborhood associated with a coarse edge are different, the former

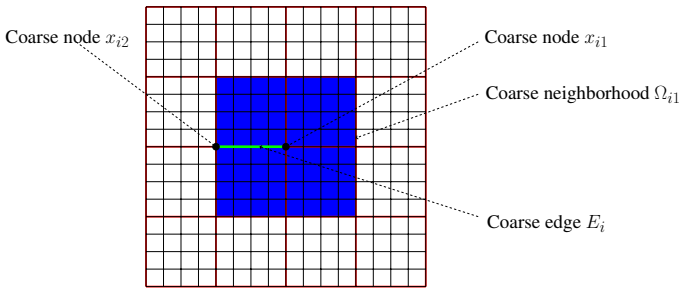

Figure III.2: Illustration of coarse nodes (black dot), a coarse edge (green edge) and a coarse neighborhood (blue block) subordinated to a coarse node.

are consist of 4 coarse blocks while the latter has two coarse blocks in the 2D case we discussed here.

III.3.1 Multiscale Space I

This approach is very close to the method of constructing multiscale basis in continuous Galerkin framework introduced in Section II.3. This is because the edge function comes from a conforming space, which is a subspace of $H_0^1(D)$. Nevertheless, the multiscale space $\boldsymbol{M}_H$ in our case is for u along the coarse-grid edges. So we can just take the trace of all space used in Section II.3 to form the space $\boldsymbol{M}_H$. Next we will show the construction in details:

Step 1: For each coarse neighborhood that associated with a coarse node x_i, we can compute or pre-define a partition of unity function (see II for more details). We denote all the partition of unities as $\{\chi_i\}_{i=1}^{N_v}$.

With the partition of unity functions, we compute $\tilde{\kappa}$ by:

$$\tilde{\kappa} := (\lambda + 2\mu) \sum_{i=1}^{N_v} |\nabla \chi_i|^2.$$

Step 2: On each coarse neighborhood Ω_i, we solve the following homogeneous Neumann eigenvalue problem in the snapshot space $\{\psi^{i,\text{snap}}\}_{k=1}^{M^{i,\text{snap}}}$(fine-scale snapshot or har-

monic extension snapshot):

$$-\nabla \cdot \underline{\sigma}(\phi) = \xi \tilde{\kappa} \phi. \tag{III.11}$$

The above local problem is solved on the fine grid and we order eigenvalues as

$$0 = \xi_1 \leq \xi_2 \leq \cdots \leq \xi_j \leq \cdots .$$

We then choose the first L_i eigenfunctions ϕ_l associated to the smallest L_i eigenvalues. We define

$$\psi_l^i = \sum_{k=1}^{M^{i,\text{snap}}} \phi_{lk} \psi_k^{i,\text{snap}}, \qquad l = 1, 2, \cdots, L_i, \tag{III.12}$$

where ϕ_{lk} is the k-th component of discrete ϕ_l. Then we multiply these functions with partition of unity χ_i, we denote the resulting functions again by ψ_l^i. We apply this process for Ω_{i1} and Ω_{i2} and thus we can obtain two set of functions ψ_l^{i1} and ψ_l^{i2}. Due to the partition of unity function χ_i, these basis are in $H_0^1(D)$.

Then we take the trace of ψ_l^{i1} and ψ_l^{i2} of on the target edge E_i respectively, and combine these two sets of 1D functions, then we obtain local offline space $\boldsymbol{M}_H(E_i)$. Generally, the functions in this set are linearly dependent, therefore we need to perform a *Proper Orthogonal Decomposition* (POD [14]) to remove the dependency, and select the most important modes in order to further reduce the dimension of $\boldsymbol{M}_H(E_i)$. The resulting space $\boldsymbol{M}_H(E_i)$ is the local multiscale basis function space we desired to construct.

Step 3: The global multiscale space $\boldsymbol{M}_H$ now can be defined as:

$$\boldsymbol{M}_H = \oplus_{i=1}^{|\mathcal{E}_H^0|} \boldsymbol{M}_H(E_i).$$

III.3.2 Multiscale Space II

In multiscale space I, for each coarse edge E_i, we have overlap in the construction of the multiscale space $\boldsymbol{M}_H$ since the space is constructed based on coarse nodes. The computational cost maybe very large since the local problem is defined in a neighborhood associated with a coarse node. Here we propose another way to construct the space $\boldsymbol{M}_H$ based on the coarse elements, which makes this approach similar to the constructing multiscale basis functions for discontinuous Galerkin coupling framework described in Section II.3. Comparing with the first approach, the local spectral problem dimension is smaller. We have following steps to obtain the second type of multiscale space.

Step 1: For each coarse edge E_i, we consider its associated two coarse elements K_{i1} and K_{i2} (see Figure III.1). For each coarse element, we solve following spectral problem:

$$\int_{K_i} \big(2\mu\epsilon(u) : \epsilon(v) + \lambda\nabla\cdot u\nabla\cdot v\big)dx = \frac{\xi}{H}\int_{\partial K_i} \langle\lambda + 2\mu\rangle\, u\cdot v\; ds, \tag{III.13}$$

in fine-scale or harmonic extension snapshot space. We then select the eigenfunctions ϕ_k corresponding to smallest L_i eigenvalues and define

$$\psi_l^i = \sum_{k=1}^{M^{i,\text{snap}}} \phi_{lk}\psi_k^{i,\text{snap}}, \qquad l = 1, 2, \cdots, L_i, \tag{III.14}$$

where $\psi_k^{i,\text{snap}}$ is the snapshot.

Therefore we can obtain two set of full domain defined functions $\{\psi_l^{i1}\}_{l=1}^{L_{i1}}$ and $\{\psi_l^{i2}\}_{l=1}^{L_{i2}}$.

Step 2: Take the trace of $\{\psi_l^{i1}\}_{l=1}^{L_{i1}}$ and $\{\psi_l^{i2}\}_{l=1}^{L_{i2}}$ on E_i to generate the local multiscale space on the coarse edges E_i respectively, namely, it can be written as:

$$\boldsymbol{M}_H(E_i) := span\{\psi_1^{i1}|_{E_i}, \psi_2^{i1}|_{E_i}, \ldots, \psi_{L_{i1}}^{i1}|_{E_i},\ \psi_1^{i2}|_{E_i}, \psi_2^{i2}|_{E_i}, \ldots, \psi_{L_{i2}}^{i2}|_{E_i}\}.$$

Due the functions in $\boldsymbol{M}_H(E_i)$ comes from two separate spectral problems, again we need to again apply POD to remove the dependence among these functions and select the most important modes. Then we obtain the local multiscale space $\boldsymbol{M}_H(E_i)$ for the targeted edge E_i.

Step 3: The global multiscale space $\boldsymbol{M}_H$ now can be defined as:

$$\boldsymbol{M}_H = \oplus_{i=1}^{|\mathcal{E}_H^0|} \boldsymbol{M}_H(E_i).$$

III.3.3 Multiscale Space III

The first two approaches involve applying POD because the local basis functions comes from the eigenfunctions of two spectral problems. The third approach we will introduce involves only one spectral problem for each coarse edge E_i. The details are as follows:

Step 1: For each coarse edge E_i, consider a spectral problem in the neighborhood ω_i (see figure III.1). More specifically, we solve following eigenvalue problem:

$$\int_{\omega_i} \big(2\mu\epsilon(u) : \epsilon(v) + \lambda\nabla \cdot u\nabla \cdot v\big)dx = \xi \int_{\partial\omega_i} \langle \lambda + 2\mu \rangle \, u \cdot v \; ds, \tag{III.15}$$

in local fine-scale or harmonic extension snapshot space that is supported on ω_i. We then take the eigenfunctions ϕ_k corresponding to smallest L_i eigenvalues and define

$$\psi_l^i = \sum_{k=1}^{M^{i,\text{snap}}} \phi_{lk} \psi_k^{i,\text{snap}}, \qquad l = 1, 2, \cdots, L_i, \tag{III.16}$$

where $\psi_k^{i,\text{snap}}$ is the snapshot.

Step 2: Take the trace of full domain defined functions $\{\psi_l^i\}_{i=1}^{L_i}$ on E_i to fill $\boldsymbol{M}_H(E_i)$, namely

$$\boldsymbol{M}_H(E_i) := span\{\psi_1^i|_{E_i}, \psi_2^i|_{E_i}, \ldots, \psi_{L_i}^i|_{E_i}\}.$$

Step 3: The global multiscale space $\boldsymbol{M}_H$ now again can be defined as:

$$\boldsymbol{M}_H = \oplus_{i=1}^{|\mathcal{E}_H^0|} \boldsymbol{M}_H(E_i).$$

We remark the second method requires least computational cost since the dominant computation is to solve the eigenvalue problem and the dimension of the spectral problem of the second method is the smallest. The oversampling techniques can be applied to create the snapshot space and offline space, one can also use randomized snapshot when generating snapshot space.

III.4 Numerical results

In this section, we present some representative numerical experiments to verify the performance of HDG-GMsFEM. We compute the multiscale solution $(u_H, \underline{\sigma}_H)$ on coarse grid and study the error with respect to the find-grid reference solution. We focus our study on the convergence of HDG-GMsFEM solution with more basis added to the coarse space with fixed find-grid and coarse-grid size. We will also study the effects of randomized snapshot, oversampling, media contrast and nearly incompressible media.

In all simulations reported below, the computational domain $D = [0, 1]^2$, the fine-scale grid is 100×100, while the coarse-scale grid is 10×10. We will consider two different Young's modulus fields $E(x)$, as depicted in Figure III.3. We note that in the blue region $E(x) = 1$ and in the red region $\kappa = \eta$ ($>> 1$), $\lambda(x) = \frac{\nu}{(1+\nu)(1-2\nu)}E(x)$, $\mu(x) = \frac{1}{2(1+\nu)}E(x)$. As it is shown, these two models contain high permeable inclusions, short and long channels.

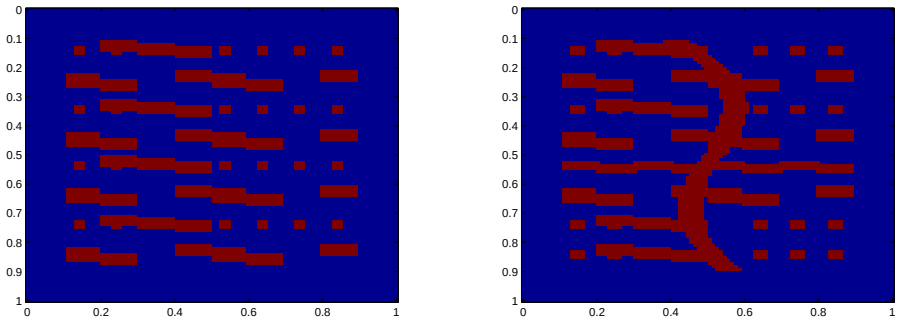

(a) Model a (b) Model b

Figure III.3: Young's modulus $E(x)$

In all simulations, we use constant force and homogeneous Dirichlet boundary conditions. We use constant source and the stabilization parameter $\tau = \frac{(\bar{\lambda}+2\bar{\mu})}{h}$, where h is the fine-grid size. Harmonic extension snapshot is adopted for all tests. We use additional one more fine-grid element if oversampling is applied. The reference solution $(u_h, \underline{\sigma}_h)$ is computed on the fine scale grid by applying the lowest order HDG method introduced in [72]. $\boldsymbol{W}_h$ and $\underline{\boldsymbol{V}}_h$ consist of piece-wise quadratic and piece-wise linear, discontinuous functions on $\mathcal{T}_h$, $\boldsymbol{M}_h^0$ of piece-wise linear, discontinuous function in $\mathcal{E}_h$. We note the dimension of the reference solution is $4|\mathcal{E}_h^0|$, which is 79200. We define the weighted L^2 norm as following

$$||\underline{\sigma}||_{L^2(\mathcal{A},D)} = \sqrt{(\mathcal{A}\underline{\sigma}, \underline{\sigma})_D},$$

to quantify the error of $\underline{\sigma}$ and use classical L^2 norm to quantify the error of u.

In all tables presented below, "Dim" represents the dimension of the coarse system, "N_b" means the number of basis used per coarse edge, we will the same number of basis for all the coarse edges, "ν" is the Poisson ratio.

We first summarize our major observations:

1. The HDG-GMsFEM solution converges fast with more multiscale basis added to each of the three multiscale space introduced,

2. HDG-GMsFEM is very robust with respect to the media contrast,

3. Oversampling can improve the accuracy of the coarse solution, especially for Multiscale Space II,

4. Randomized snapshot is very efficient and is a good alternate for the full snapshot,

5. HDG-GMsFEM is capable of dealing with nearly incompressible material.

III.4.1 Numerical results of Model a

In this subsection, we study the numerical experiments for the model a by applying Multiscale I$-$III. In this numerical tests, we study the error decay behavior by adding different types of multiscale basis functions. The results are presented in Tables III.1$-$III.3. The results of the case $\eta = 10^6$ are report in parentheses. As it is shown the HDG-GMsFEM solution converges to the reference solution (find-grid solution). We observe a fast error decay if as more basis functions are added for all three type of multiscale basis. For example, The relative L^2 error of u_H decreases from 6.7% to 1.0% when multiscale space I is applied without oversampling, while the dimension of the coarse system increase from 1080 to 2160, which is just 1.36% to 2.73% of the degrees of freedom of the fine-scale problem. We also notice that oversampling can help decrease the error although only one find-grid element is added. Oversampling is particular usefully when multiscale space II is applied (see Table III.2), since in this case the local domain to compute the snapshot now covers the support of local basis and thus can remove the boundary effects. We observe that oversampling is not that efficient for Multiscale Space I compared with Multiscale II and III, this is because in this scenario, the local domain of computing snapshot has already covered the target edge. The effects of apply oversampling for

Dim(N_b)	$\frac{\|\underline{\sigma}_h - \underline{\sigma}_H\|_{L^2(\mathcal{A},\Omega)}}{\|\underline{\sigma}_h\|_{L^2(\mathcal{A},\Omega)}}$		$\frac{\|u_h - u_H\|_{L^2(\Omega)}}{\|u_h\|_{L^2(\Omega)}}$	
	No oversampling	Oversampling	No oversampling	Oversampling
1080(3)	0.193(0.199)	0.189(0.195)	0.067(0.071)	0.065(0.069)
1440(4)	0.114(0.123)	0.114(0.131)	0.029(0.033)	0.029(0.035)
1800(5)	0.067(0.070)	0.068(0.078)	0.013(0.014)	0.013(0.016)
2160(6)	0.055(0.069)	0.044(0.051)	0.010(0.015)	0.007(0.009)

Table III.1: Relative errors between the HDG-GMsFEM solution and the fine-scale HDG solution, with Multiscale Space I for Model a, $\eta = 10^4(10^6)$, $\nu = 0.2$.

Dim(N_b)	$\frac{\|\underline{\sigma}_h - \underline{\sigma}_H\|_{L^2(\mathcal{A},\Omega)}}{\|\underline{\sigma}_h\|_{L^2(\mathcal{A},\Omega)}}$		$\frac{\|u_h - u_H\|_{L^2(\Omega)}}{\|u_h\|_{L^2(\Omega)}}$	
	No oversampling	Oversampling	No oversampling	Oversampling
1080(3)	0.210(0.235)	0.162(0.162)	0.076(0.092)	0.048(0.048)
1440(4)	0.159(0.205)	0.086(0.086)	0.046(0.076)	0.017(0.017)
1800(5)	0.124(0.159)	0.056(0.056)	0.030(0.048)	0.009(0.009)
2160(6)	0.093(0.109)	0.034(0.033)	0.019(0.025)	0.005(0.005)

Table III.2: Relative errors between the HDG-GMsFEM solution and the fine-scale HDG solution, with Multiscale Space II for Model a, $\eta = 10^4(10^6)$, $\nu = 0.2$.

HDG-GMsFEM is quite similar to the oversampling results in chapter II. By comparing the results of $\eta = 10^4$ and $\eta = 10^6$, we can see clearly all three Multiscale Spaces are robust against to the media contrast. We show the reference solution and HDG-GMsFEM solutions computed with different number of basis functions in Figures III.4 and III.5. We can observe obvious difference between the HDG-GMsFEM solution with only 2 basis functions per coarse edge and reference solution. If we increase the basis number to 4, we notice, at first glance, the multiscale solution looks similar to the reference solution. However, if we take a closer look, we notice some missing features in inner part of the solution. When we use 6 basis functions per coarse edge, these features can be recovered correctly.

Dim(N_b)	$\frac{\|\underline{\sigma}_h - \underline{\sigma}_H\|_{L^2(\mathcal{A},\Omega)}}{\|\underline{\sigma}_h\|_{L^2(\mathcal{A},\Omega)}}$		$\frac{\|u_h - u_H\|_{L^2(\Omega)}}{\|u_h\|_{L^2(\Omega)}}$	
	No oversampling	Oversampling	No oversampling	Oversampling
1080(3)	0.207(0.207)	0.191(0.190)	0.067(0.067)	0.057(0.057)
1440(4)	0.138(0.133)	0.119(0.115)	0.033(0.032)	0.026(0.025)
1800(5)	0.091(0.109)	0.069(0.070)	0.017(0.023)	0.012(0.012)
2160(6)	0.059(0.070)	0.050(0.056)	0.010(0.012)	0.008(0.009)

Table III.3: Relative errors between the HDG-GMsFEM solution and the fine-scale HDG solution, with Multiscale Space III for Model a, $\eta = 10^4(10^6)$, $\nu = 0.2$.

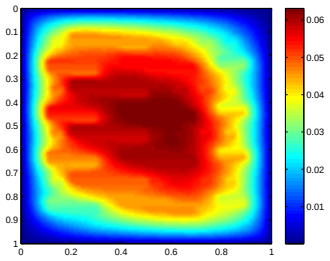

(a) Fine solution of u_1.

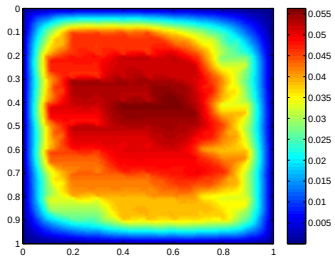

(b) HDG-GMsFEM solution of u_1 with 2 basis.

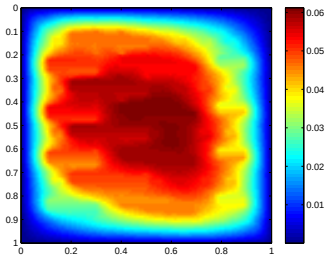

(c) HDG-GMsFEM solution of u_1 with 4 basis.

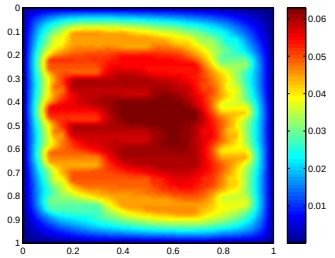

(d) HDG-GMsFEM solution of u_1 with 6 basis.

Figure III.4: Comparison of the HDG-GMsFEM solution and the fine-scale HDG solution (first component of displacement) with Multiscale Space III for model a, $\eta = 10^4$, no oversampling, $\nu = 0.2$.

III.4.2 Numerical results of Model b

Next, we consider the model b and compare to the previous results, see Table III.4−III.6. This model includes a long channel which will bring a long-range effect in the

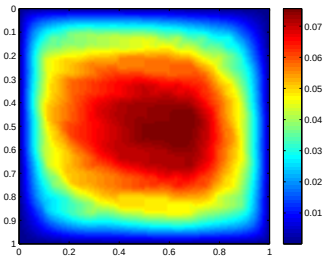

(a) Fine solution of u_2.

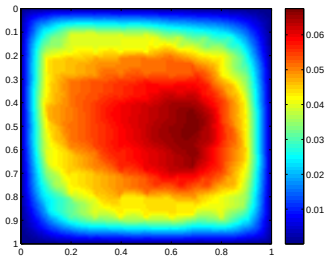

(b) HDG-GMsFEM solution of u_2 with 2 basis.

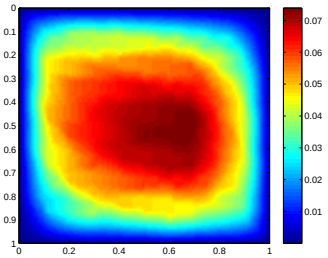

(c) HDG-GMsFEM solution of u_2 with 4 basis.

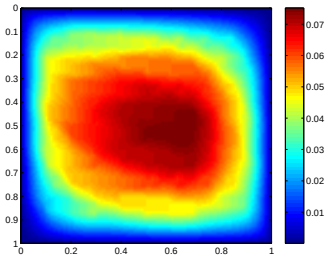

(d) HDG-GMsFEM solution of u_2 with 6 basis.

Figure III.5: Comparison of the HDG-GMsFEM solution and the fine-scale HDG solution (second component of displacement) with Multiscale Space III for Model a, $\eta = 10^4$, no oversampling, $\nu = 0.2$.

solution. Again, we can see that the error decreases as more basis is added. We also notice the robustness of the three types Multiscale basis functions with respect to the contrast. Again, we see that the error is reduced if we apply oversampling technique. In particular, the L^2 error of u decrease from 3.0% to 0.9% if 5 bases from Multiscale Space II are used.

III.4.3 Randomized snapshot

We have already seen that oversampling can help increase the accuracy of HDG-GMsFEM, however applying oversampling will increase the computational cost of offline stage especially in 3D case. This problem can be relieved by using randomized boundary conditions to generate the snapshot space. The main idea of this approach is to use

Dim(N_b)	$\frac{\|\underline{\sigma}_h-\underline{\sigma}_H\|_{L^2(\mathcal{A},\Omega)}}{\|\underline{\sigma}_h\|_{L^2(\mathcal{A},\Omega)}}$		$\frac{\|u_h-u_H\|_{L^2(\Omega)}}{\|u_h\|_{L^2(\Omega)}}$	
	No oversampling	Oversampling	No oversampling	Oversampling
1080(3)	0.112(0.114)	0.112(0.113)	0.024(0.027)	0.024(0.026)
1440(4)	0.074(0.072)	0.076(0.069)	0.013(0.014)	0.014(0.013)
1800(5)	0.041(0.041)	0.037(0.039)	0.006(0.007)	0.006(0.006)
2160(6)	0.027(0.027)	0.025(0.025)	0.004(0.004)	0.004(0.004)

Table III.4: Relative errors between the HDG-GMsFEM solution and the fine-scale HDG solution, with Multiscale Space I for Model b, $\eta = 10^4(10^6)$, $\nu = 0.2$.

Dim(N_b)	$\frac{\|\underline{\sigma}_h-\underline{\sigma}_H\|_{L^2(\mathcal{A},\Omega)}}{\|\underline{\sigma}_h\|_{L^2(\mathcal{A},\Omega)}}$		$\frac{\|u_h-u_H\|_{L^2(\Omega)}}{\|u_h\|_{L^2(\Omega)}}$	
	No oversampling	Oversampling	No oversampling	Oversampling
1080(3)	0.167(0.184)	0.130(0.128)	0.047(0.057)	0.031(0.031)
1440(4)	0.131(0.153)	0.077(0.074)	0.033(0.045)	0.014(0.013)
1800(5)	0.084(0.101)	0.043(0.036)	0.016(0.023)	0.006(0.006)
2160(6)	0.069(0.082)	0.037(0.027)	0.012(0.017)	0.005(0.004)

Table III.5: Relative errors between the HDG-GMsFEM solution and the fine-scale HDG solution, with Multiscale Space II for Model b, $\eta = 10^4(10^6)$, $\nu = 0.2$.

Dim(N_b)	$\frac{\|\underline{\sigma}_h-\underline{\sigma}_H\|_{L^2(\mathcal{A},\Omega)}}{\|\underline{\sigma}_h\|_{L^2(\mathcal{A},\Omega)}}$		$\frac{\|u_h-u_H\|_{L^2(\Omega)}}{\|u_h\|_{L^2(\Omega)}}$	
	No oversampling	Oversampling	No oversampling	Oversampling
1080(3)	0.162(0.161)	0.160(0.167)	0.040(0.040)	0.039(0.043)
1440(4)	0.108(0.114)	0.102(0.102)	0.022(0.025)	0.020(0.020)
1800(5)	0.077(0.081)	0.077(0.080)	0.014(0.015)	0.014(0.015)
2160(6)	0.055(0.061)	0.050(0.045)	0.009(0.011)	0.008(0.007)

Table III.6: Relative errors between the HDG-GMsFEM solution and the fine-scale HDG solution, with Multiscale Space III for Model b, $\eta = 10^4(10^6)$, $\nu = 0.2$.

random boundary conditions when computing harmonic extension snapshots. This will substantially reduce the dimension of the spectral problem defined in snapshot space. For example, in the setting of Multiscale Space III in Tables III.3 and III.6, the dimension of oversampling snapshot is 136. We conduct the same set of numerical experiments with

some random boundary conditions and report the results in Tables III.7 and table III.8. We note that We can see that, in general, using the harmonic extension snapshot space from randomized boundary conditions leads to slightly larger errors. However, the offline computational cost is reduced significantly.

# of random BC / Dim(N_b)	$N_b + 4$	$N_b + 8$	$N_b + 12$	136 (Full snapshot)
1080(3)	0.072	0.073	0.069	0.057
1440(4)	0.039	0.039	0.040	0.026
1800(5)	0.024	0.023	0.021	0.012
2160(6)	0.012	0.011	0.010	0.008

Table III.7: Relative L^2 errors of displacements between the HDG-GMsFEM solution and the fine-scale HDG solution, with Multiscale Space III for Model a, randomized snapshot, $\eta = 10^4$.

# of random BC / Dim(N_b)	$N_b + 4$	$N_b + 8$	$N_b + 12$	136 (Full snapshot)
1080(3)	0041	0.040	0.044	0.039
1440(4)	0.029	0.027	0.027	0.019
1800(5)	0.018	0.018	0.020	0.013
2160(6)	0.014	0.012	0.014	0.008

Table III.8: Relative L^2 errors of displacements between the HDG-GMsFEM solution and the fine-scale HDG solution, with Multiscale Space III for Model b, randomized snapshot, $\eta = 10^4$.

III.4.4 HDG-GMsFEM for the nearly incompressible material

We also test our methods for the nearly incompressible material, the results are reported in Table III.9. We can also observe the convergence behavior of the error with the increase of basis functions. It is clear that our method is robust with respect to the Poisson ratio ν.

Dim(N_b)	Model a		Model b	
	ν=0.49999	ν=0.499999	ν=0.49999	ν=0.499999
1080(3)	0.019	0.007	0.023	0.010
1440(4)	0.005	0.002	0.010	0.004
1800(5)	0.003	0.001	0.006	0.003
2160(6)	0.002	0.001	0.005	0.002

Table III.9: Relative L^2 errors between the HDG-GMsFEM solution and the fine-scale HDG solution, with Multiscale Space III for Model a and model b, oversampling is applied, $\eta = 10^4$.

III.5 Concluding remarks

We design a multiscale model reduction method using HDG-GMsFEM for first-order formulation of elasticity equations in heterogeneous media. We introduce three methods of constructing multiscale basis function. We study the numerical performance of these methods comprehensively with two highly heterogeneous model. The results show these methods are robust and efficient in providing an accurate coarse-grid solution even for the nearly incompressible media.

IV. GENERALIZED MULTISCALE FINITE ELEMENT METHODS FOR THE HELMHOLTZ EQUATION IN VARIABLE DENSITY MEDIA *

IV.1 Introduction

Efficient Helmholtz equation solver is vitally important for many geophysical applications. For instance, frequency-domain full-waveform inversion relies on solving the Helmholtz equations for obtaining wavefield in the frequency domain [71, 81, 19]. The computation cost of the frequency-domain full-waveform inversion almost totally relies on the computational cost of the Helmholtz solver. Conventional numerical methods for solving the Helmholtz equation include finite-difference methods (FDM) [75, 70, 68, 24, 25, 60, 61], finite-element methods (FEM) [48], and generalized finite-element method (GFEM) [10, 64], etc.

FDM is widely used in geophysics community because of its efficiency and simplicity, yet it is only applicable on structured mesh. FEM is more suitable to handle unstructured mesh as well as complicated topography. The conventional FDM and FEM for Helmholtz equation share a common disadvantage that the computational complexity and cost of solving the linear system associated with Helmholtz equation will be prohibitively large for models that contain larger number of grids, especially for large 3D models [70]. Moreover, current oil and gas exploration tends to investigate finer and finer details of target reservoirs, and to characterize smaller and smaller geological heterogeneities that are probably smaller than the wavelength of seismic wavefield. In these cases, one needs very finely discretized model, and since the computational time and memory cost are directly proportional to the grid number in FDM or FEM, the computational cost will increase

*Part of this chapter is reprinted with permission from "Fast solver for Helmholtz equation using multiscale basis functions" by Fu, Shubin and Gao, Kai, 2015. SEG Technical Program Expanded Abstracts 2015, pp. 3688-3693. Copyright [2017] by SEG.

accordingly. GFEM can alleviate this difficulty by using coarser mesh, however it is not suitable for solving Helmholtz equation in media with high velocity contrasts or variable mass density due to the fact that the basis function in GFEM is product of the partition of unity and polynomial or trigonometric functions. The basis function therefore contains no information of the heterogeneous media, which makes GFEM effective and accurate only for homogeneous media.

Some methods focus on reducing the computational complexity and storage by exploring and optimizing the internal structure of the coefficient matrix in Helmholtz equation's discrete system. For example, [82] developed a structured parallel multifrontal direct Helmholtz solver based on the equation's Hierarchically Semi-Separable (HSS) structure.

Another direction to reduce the computational cost is to adopt the multiscale method. For the application of multiscale method to solve the wave equation we refer [75, 57, 39, 42, 28]. All these methods show some advantages over conventional FDM and FEM in terms of computational cost. The generalized multiscale finite-element method (GMsFEM) [42, 28] has proved to be an efficient method in solving wave equations in time domain. We now extend the GMsFEM to solve Helmholtz equation. The key part of our method is constructing multiscale basis functions for each coarse neighborhood on the coarsely discretized mesh. We first solve an appropriately designed local eigenvalue problem for each coarse neighborhood, and select the eigenvectors corresponding to several smallest eigenvalues. We then multiply these eigenvectors with multiscale partition of unity to construct the final coarse approximation space for Helmholtz equation. These multiscale basis functions contain information of the heterogeneous model, and this makes them more suitable and accurate than the polynomial or trigonometric functions to solve Helmholtz equation on the coarse mesh. In this chapter, we first briefly review the continuous Galerkin formulation of finite-element method for solving Helmholtz equation. Then we explain the methodology of how to construct multiscale basis functions,

and incorporate such multiscale basis functions into the fully discrete system associated with Helmholtz equation. Finally, we present an example to demonstrate the accuracy and efficiency of our method.

IV.1.1 Helmholtz equation and the continuous Galerkin (CG) formulation

We consider the following Helmholtz equation for heterogeneous acoustic media with variable mass density in the space domain D:

$$-\frac{\omega^2}{\rho c^2}p - \nabla \cdot \left(\frac{1}{\rho}\nabla p\right) = f, \tag{IV.1}$$

where $p = p(\mathbf{x}, \omega)$ is the pressure wavefield in the frequency-space domain, ω is the angular frequency, $c = c(\mathbf{x})$ is the wave propagation velocity of the medium, $\rho = \rho(\mathbf{x})$ is the mass density of the medium, and $f = f(\mathbf{x}, \omega)$ is the external force term. Both $c(\mathbf{x})$ and $\rho(\mathbf{x})$ can contain high-contrast variations in space. Conventionally, the Helmholtz equation (IV.1) is solved by assuming constant mass density for simplicity. However, subsurface mass density can vary sharply in space in realistic geological settings, and therefore the assumption of heterogeneous $\rho(\mathbf{x})$ is one of the important considerations when we develop the GMsFEM-based Helmholtz equation solver to embrace a wider range of geophysical applications.

To appropriately represent the subsurface media with discrete meshes, we denote $\mathcal{T}_H$ as a coarse partition of the computational domain D. We call $\mathcal{T}_H$ the coarse grid and H the size of the coarse grid. Elements of $\mathcal{T}_H$ are called coarse grid blocks (see Figure IV.1). The set of all coarse grid nodes is denoted by $\mathcal{P}_H$, N_c is the total number of coarse nodes. $\mathcal{T}_h$ as a refinement of $\mathcal{T}_H$. Each of these K_i may contain many finer elements of $\mathcal{T}_h$.

Let V_0^h be a finite element space defined on $\mathcal{T}_h$. Then the fine-grid solution of Helmholtz

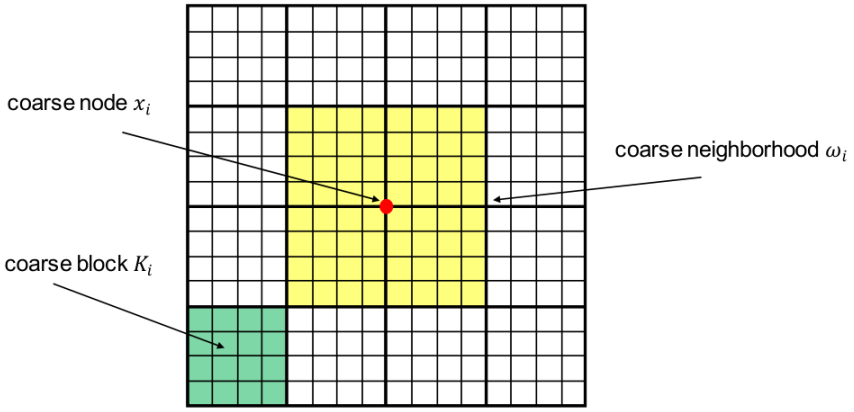

Figure IV.1: Illustration of a coarse node (red dot), a coarse block (green block) and a coarse neighborhood (yellow block).

equation IV.1 can be obtained as

$$a(p_h, v) = (f, v), \quad \forall v \in V_0^h, \tag{IV.2}$$

where

$$a(p, v) = \int_D -\frac{\omega^2}{\rho c^2} pv d\mathbf{x} + \frac{1}{\rho} \nabla p \cdot \nabla v d\mathbf{x}, \quad (f, v) = \int_D f v d\mathbf{x}. \tag{IV.3}$$

Let V_0^H be a finite-dimensional approximation space where the coarse-grid solution lives, then solving Helmholtz equation 1 on $\mathcal{T}_H$ can be stated as: find $p_H \in V_0^H$ such that

$$a(p_H, v) = (f, v), \quad \forall v \in V_0^H, \tag{IV.4}$$

We call the solution to Helmholtz equation on $\mathcal{T}_h$ the conventional CG-FEM solution, while that on $\mathcal{T}_H$ the GFEM solution if the basis functions on $\mathcal{T}_H$ are conventional polynomial basis functions, and the CG-GMsFEM solution if the basis functions are multiscale basis functions, which we will solve below.

IV.1.2 Multiscale basis functions

The most important ingredient of our GMsFEM-based Helmholtz equation solver is the multiscale basis functions. To obtain appropriate multiscale basis functions to form the space V_0^H, for each coarse node $\mathbf{x}_i \in \mathcal{P}_H$, we define the coarse neighborhood ω_i by:

$$\omega_i = \bigcup \{K_j \ : \ K_j \subset \mathcal{T}^H, \ x_i \in K_j\}.$$

That is, ω_i is the union of all coarse grid blocks K_j having the vertex $\mathbf{x}_i$ (see Figure IV.1). To construct the local multiscale basis for the coarse neighborhood ω_i, we need a partition of unity function χ_i [64]. One choice is the piecewise bi-linear hat function ϕ_i on the coarse grid that has value 1 at the coarse node $\mathbf{x}_i$ and 0 at all other coarse nodes. Another choice is the multiscale partition of unity χ_i which is defined in the following way. Let K_j be a coarse grid block including $\mathbf{x}_i$, then the restriction of χ_i in K_j is the solution of following equation

$$-\nabla \cdot \left(\frac{1}{\rho}\nabla u\right) = 0, \qquad \text{in } K_j \tag{IV.5}$$

$$u = \phi_i, \qquad \text{on } \partial K_j. \tag{IV.6}$$

Inspired by the appendix of [33], we consider the following eigenvalue problem in the coarse neighborhood ω_i:

$$-\nabla \cdot \left(\frac{\chi_i^2}{\rho}\nabla \varphi\right) = \lambda \frac{\chi_i^2}{\tilde{\rho}}\varphi, \tag{IV.7}$$

with zero Neumann boundary condition

$$\frac{1}{\rho}\frac{\partial \varphi}{\partial \mathbf{n}} = 0, \tag{IV.8}$$

where $\mathbf{n}$ is the outward-pointing normal vector of K, and

$$\frac{1}{\tilde{\rho}} = \sum_{i=1}^{Nc} \frac{1}{\rho} |\nabla \chi_i|^2. \tag{IV.9}$$

The discrete form of equation (IV.7) is a finite-dimensional eigenvalue problem which can be written as

$$\mathbf{S}\varphi = \lambda \mathbf{M}\varphi, \tag{IV.10}$$

where λ is the eigenvalue. $\mathbf{S}$ and $\mathbf{M}$ are the stiffness and mass matrices corresponding with the coarse neighborhood ω_i, respectively, which can be written as

$$\mathbf{S}_{\mathbf{m},\mathbf{n}} = \int_{\omega_i} \frac{\chi_i^2}{\rho} \nabla \xi_n \cdot \nabla \zeta_m d\mathbf{x}, \tag{IV.11}$$

$$\mathbf{M}_{\mathbf{m},\mathbf{n}} = \int_{\omega_i} \frac{\chi_i^2}{\tilde{\rho}} \xi_n \zeta_m d\mathbf{x}, \tag{IV.12}$$

where ξ_n and ζ_m are fine-scale finite element basis functions (e.g., piecewise linear functions)

By solving equation (IV.10), we can obtain a series of eigenvalues and eigenvectors for each coarse neighborhood ω_i ($i = 1, 2, \cdots, N_c$). For each of these coarse neighborhoods, we first order the eigenvalues in an ascending way, i.e.,

$$\lambda_1^i \leq \lambda_2^i \leq \cdots \leq \lambda_j^i \leq \cdots . \tag{IV.13}$$

Then we select the first L_i eigenvectors φ_i^j ($j = 1, 2, \cdots, L_i$) corresponding to the smallest L_i eigenvalues. Note these eigenfunctions are not globally continuous, therefore we multiply φ_i^j with the partition of unity $\{\chi_i\}_{i=1}^N$. Here we use the second type of partition of unity function which include local medium properties $\rho(\mathbf{x})$ within the coarse neighborhood ω_i. Using eigenfunctions and multiscale partition of unity is the most im-

portant feature of our method. In contrast, FEM and GFEM use only polynomial basis functions, which are only determined by the order of the polynomials. These predefined basis functions are invariant under different local medium properties, and therefore cannot effectively capture the fine details of the investigated heterogeneous media.

With these eigenfunctions, we now define the coarse mesh approximation space as

$$V_0^H = \text{span}\{\Phi_j^i | 1 \leq i \leq N, 1 \leq j \leq L_i\}, \tag{IV.14}$$

where $\Phi_i^j = \varphi_i^j \chi_i$.

IV.1.3 Discrete Helmholtz equation system

The aforementioned multiscale basis functions enable us to obtain the discrete system for the Helmholtz equation in the coarse space V_H^0 as

$$\mathbf{AP} = \mathbf{F}, \tag{IV.15}$$

where for each coarse neighborhood ω_i, the local matrix $\mathbf{A}_i$ is

$$\mathbf{A}_i = \sum_{k,l} \int_{\omega_i} \left(-\frac{\omega^2}{\rho c^2} \Phi_i^k \Phi_i^l + \frac{1}{\rho} \nabla \Phi_i^k \cdot \nabla \Phi_i^l \right) d\mathbf{x}, \tag{IV.16}$$

while the RHS is the force term, and has the form

$$\mathbf{F}_i = \sum_k \int_{\omega_i} f \Phi_i^k d\mathbf{x}. \tag{IV.17}$$

Meanwhile, $\mathbf{P}$ is the solution of the Helmholtz equation on $\mathcal{T}^H$.

In practical implementation, we don't assemble the matrices $\mathbf{A}$ and vector $\mathbf{F}$ directly. One can use the representation of multiscale basis functions via fine-scale basis functions

to obtain $\mathbf{A}$ and $\mathbf{F}$. Assume the i-th basis Φ_i in space V_0^H can be written as

$$\Phi_i = \sum_j d_{ij}\phi_j^f$$

where d_{ij} is the coefficient and ϕ_j^f is the piecewise linear basis functions for V_0^h. Then, we have

$$\begin{aligned}\mathbf{A}_{i,j} &= \int_D -\frac{\omega^2}{\rho c^2}\Phi_i\Phi_j d\mathbf{x} + \frac{1}{\rho}\nabla\Phi_i\cdot\nabla\Phi_j d\mathbf{x} \\ &= \sum_{m,n} d_{mi}\int_D -\frac{\omega^2}{\rho c^2}\phi_m^f\phi_n^f d\mathbf{x} + \frac{1}{\rho}\nabla\phi_m^f\cdot\nabla\phi_n^f d\mathbf{x} d_{jn}\end{aligned} \tag{IV.18}$$

Denoting the matrix for the fine-scale problem by $\mathbf{A}^f = (a_{mn}^f)$, $a_{mn}^f = a(\phi_m^f, \phi_n^f)$ then we have

$$\mathbf{A} = \mathbf{D}\mathbf{A}^f\mathbf{D}^{\mathrm{T}}$$

Similarly, $\mathbf{F} = \mathbf{D}\mathbf{F}^f$, where $\mathbf{F}^f = (F_i^f)$, $F_i^f = (f, \phi_i^f)$. Therefore, we just need to assemble fine-scale matrix $\mathbf{A}$ and vector $\mathbf{F}$, and form the basis representation matrix $\mathbf{D}$ in which each row stores a discrete multiscale function Φ_i.

Equation (IV.15) can serve as a general discrete form for the Helmholtz equation. The dimension of $\mathbf{H}$, $N_{\mathbf{H}}$, is a factor that directly affects the computation efficiency of the Helmholtz equation solver. Although $\mathbf{A}$ can be sparse, a large $N_{\mathbf{H}}$ can significantly increase the complexity and therefore increase the computation memory/time. With our multiscale Helmholtz equation solver, $N_{\mathbf{D}} = \sum_i^N L_i$, which can be much smaller than the corresponding size of the system that is constructed directly on $\mathcal{T}^h$, especially when $\mathcal{T}^H$ is adequately coarse, i.e., $N_{\mathbf{H}}$ is very small. Solving equation (IV.15) is the therefore much more efficient than solving the corresponding system on $\mathcal{T}^h$. Our multiscale Helmholtz solver can also be constructed in a space-adaptive way: The number of the

multiscale basis functions can vary in different coarse neighborhood ω_i. This is because the spatial accuracy of a Helmholtz solver is determined by the number of grid points to represent the wavelength, which is eventually determined by the medium properties (c in our formulation). If a neighborhood ω_i has higher c, fewer number of multiscale basis functions (smaller L_i) can be used, and larger L_i vice versa. In this way, we can construct space-adaptive multiscale basis function space that can still achieve high accuracy. After obtaining $\mathbf{D}$, we can project it onto the $\mathcal{T}^h$ by using the solved multiscale basis functions Φ_i^j, which is a process that costs trivially small computational time.

IV.1.4 Perfectly Matched Layers for the multiscale Helmholtz equation solver

Absorptions of outgoing wavefields at computational domain boundary is important many applications. There are several mature methods to achieve this goal, for example, the one-way wave equation methods, damping boundary conditions, and Perfectly Matched Layers (PML) [13, 45]. PML has been proved to be very effective and efficient for various wavefield propagation problems because of its superior absorption effect. We apply the PML to our multiscale Helmholtz equation solver.

To simplify the discussion of implementing PML, we assume the computational domain $D = (0, 1)^2$ without loss of generality. The methodology can be easily extended to three dimensional case and irregular domain with trivial modifications.

We define

$$f(x) = \begin{cases} \dfrac{C}{\xi}\left(\dfrac{x-\xi}{\xi}\right)^2, & x \in [0, \xi], \\ 0, & x \in [\xi, 1-\xi], \\ \dfrac{C}{\xi}\left(\dfrac{x-1+\xi}{\xi}\right)^2, & x \in [1-\xi, 1], \end{cases} \tag{IV.19}$$

and

$$g_1(x_1) = \left(1 + i\frac{f(x_1)}{\omega}\right)^{-1}, \tag{IV.20}$$

$$g_2(x_2) = \left(1 + i\frac{f(x_2)}{\omega}\right)^{-1}, \tag{IV.21}$$

where x_1 and x_2 represents the space variables. In equation (IV.19), ξ is the thickness of the PML, and is typically equal to one wavelength. C is an appropriate positive constant independent of the frequency ω.

Then the Helmholtz equation IV.1 can be written as

$$\left(-\frac{\omega^2}{\rho c^2 g_1 g_2}p - \frac{\partial}{\partial x_1}\left(\frac{g_1}{g_2}\frac{1}{\rho}\frac{\partial}{\partial x_1}\right) - \frac{\partial}{\partial x_2}\left(\frac{g_2}{g_1}\frac{1}{\rho}\frac{\partial}{\partial x_2}\right)\right)p = f$$

The weak formulation of this equation can be formulated through finding $p_H \in V_0^H$ such that

$$\int_D -\frac{\omega^2}{\rho c^2 g_1 g_2}p_H w_H d\mathbf{x} + \int_D \frac{g_1}{g_2}\frac{1}{\rho}\frac{\partial p_H}{\partial x_1}\frac{\partial w_H}{\partial x_1}w_H d\mathbf{x} + \int_D \frac{g_2}{g_1}\frac{1}{\rho}\frac{\partial p_H}{\partial x_2}\frac{\partial w_H}{\partial x_2}w_H d\mathbf{x} = \int_D f w_H d\mathbf{x}, \tag{IV.22}$$

$\forall w_h \in V_0^H$. One can then compute the corresponding matrix $\mathbf{H}$ and $\mathbf{S}$.

IV.2 Results

We present two numerical examples to demonstrate the performance of our new multi-scale Helmholtz equation solver. In both of these two examples, we compute the reference solutions using the standard first-order continuous Galerkin finite-element method on the fine mesh. We investigate three types of coarse-scale solutions: Solutions titled GFEM is the the coarse-grid solution using the product of polynomial functions and partition of unity as basis functions; Solution titled GMsFEM is the coarse-grid solution using the product of eigenfunctions and partition of unity as basis functions; Solution titled adaptive

GMsFEM is the GMsFEM solution with non-uniform number of multiscale basis function in each coarse neighborhood, and the number of multiscale basis function is determined based on the relative velocity values of the coarse blocks.

To quantitatively compare the accuracy of coarse-scale solutions, we define the relative L^2-norm error of a coarse-scale solution (with GFEM, GMsFEM or adaptive GMsFEM) with respect to the reference solution as $\varepsilon = ||p - p_0||_2/||p_0||_2$, where p is the solution computed on the coarse mesh and p_0 is the reference solution computed on the fine mesh.

We solve the discrete system using the linear solver available in the commercial numerical software MATLAB. Our code is currently in its prototypical stage and therefore does not contain any parallelism optimizations. Further implementation may include using compiled languages such as C/C++ or Fortran with parallelism and optimizations to improve efficiency.

IV.2.1 Smooth heterogeneous model

In the first example, we use a smooth heterogeneous model shown in Figure IV.2. The velocity c of the model increase linearly from the top to the bottom, and we set two velocity anomalies in the model: one with higher velocity value and the other with lower velocity value. The density model ρ is set based on the Gardener's relation [44] as $\rho = 0.31c^{0.25} \times 1000$, with unit kg/m^3. The model is 5000 m in both the horizontal and vertical directions, and is composed of 1000×1000 rectangular fine elements, with element size 5 m in both directions. A point source is placed at $(500, 500)$ m of the model. We investigate the accuracy and efficiency of the GFEM and GMsFEM using two different coarse meshes, named Mesh 1 and Mesh 2, respectively. Mesh 1 is composed of 50×50 coarse elements, and Mesh 2 is composed of 100×100 coarse elements. The size of the coarse element is therefore 100 m in Mesh 1 and 50 m in Mesh 2. We investigate two source frequencies, 15 and 20 Hz, for this model.

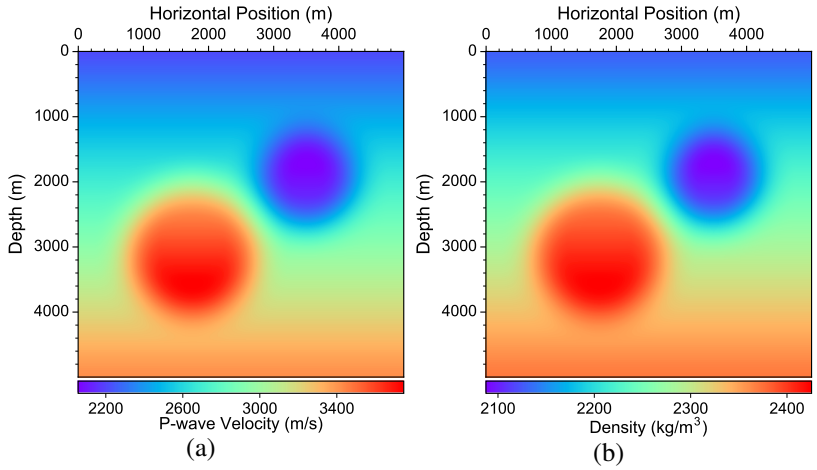

Figure IV.2: (a) P-wave velocity of a smooth heterogeneous model, and (b) the density model computed from the Gardner's relation.

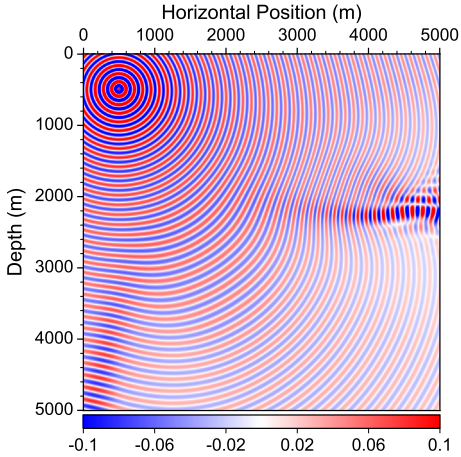

Figure IV.3: The reference fine-scale FEM solution of the Helmhotlz equation in the smooth heterogeneous model.

The reference fine-scale FEM solution with 20 Hz source frequency is shown in Figure IV.3. The wavefield caustics near the right boundary of the model is caused by the low-velocity heterogeneity at the right half of the model. The high-velocity heterogeneity on the left half of the model also causes obvious wavefield distortion.

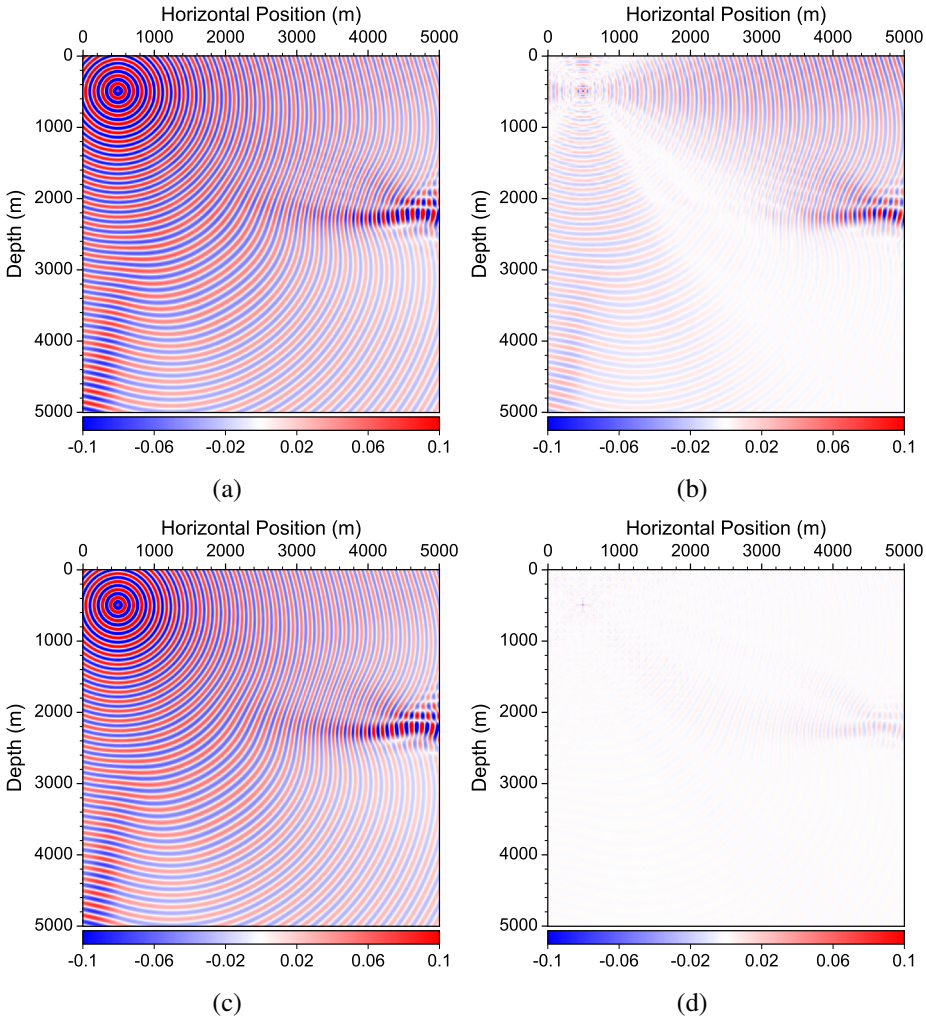

Figure IV.4: (a) Coarse-scale solution computed using the GFEM with $N_b = 16$, and (b) the absolute amplitude difference between the coarse-scale GFEM solution and the reference fine-scale FEM solution; (c) Coarse-scale solution computed using the GMsFEM with $N_b = 16$, and (d) the absolute amplitude difference between the coarse-scale GMsFEM solution and the reference fine-scale FEM solution.

The coarse-scale solutions are computed using the aforementioned polynomial-basis-based GFEM solver and multiscale-basis-based GMsFEM solver with different numbers of basis functions. For this test, we set the number of polynomial or multiscale basis functions to 4, 9 or 16. Figure IV.4a shows the coarse-scale solution p_{GFEM} with 20 Hz source frequency on Mesh 1 computed using the GFEM with 16 polynomial basis functions, and

Solution type	15 Hz				20 Hz			
	N_b	N	T (s)	ε	N_b	N	T (s)	ε
FEM reference	/	1168561	34.5	/	/	1168561	34.8	/
GFEM	4	12100	0.5	1.385	4	12100	0.5	1.506
GFEM	9	27225	16.1	0.798	9	27225	16.6	1.517
GFEM	16	48400	109.0	0.062	16	48400	109.1	0.580
GMsFEM	4	12100	0.4	1.149	4	12100	0.5	1.836
GMsFEM	9	27225	2.7	0.060	9	27225	3.1	0.344
GMsFEM	16	48400	13.7	0.010	16	48400	11.9	0.064

Table IV.1: A comparison of the number of basis functions N_b, the total number of discrete system unknowns N, the computational time T and the relative L_2-norm error ε for GFEM and GMsFEM coarse-mesh solutions in a smooth heterogeneous model on Mesh 1. The fine mesh size is 5 m in both directions and the coarse mesh size is 100 m in both directions.

Solution type	15 Hz				20 Hz			
	N_b	N	T (s)	ε	N_b	N	T (s)	ε
FEM reference	/	1168561	34.5	/	/	1168561	34.8	/
GFEM	4	47524	2.8	0.660	4	47524	3.0	1.433
GFEM	9	106929	108.1	0.020	9	106929	109.3	0.134
GMsFEM	4	47524	3.3	0.286	4	47524	3.0	1.017
GMsFEM	6	71286	7.3	0.013	6	71286	7.3	0.061
GMsFEM	9	106929	19.1	0.005	9	106929	19.0	0.014

Table IV.2: A comparison between the reference fine-mesh solution and the GFEM and GMsFEM coarse-mesh solutions in a smooth heterogeneous model on Mesh 2. The fine mesh size is 5 m in both directions and the coarse mesh size is 50 m in both directions. N_b, N, T and ε are explained in Table IV.1.

Figure IV.4b shows the difference between p_{GFEM} and the reference fine-scale solution p_0. In contrast, Figure IV.4c show the coarse-scale solution p_{GMsFEM} with 20 Hz source frequency on Mesh 1 computed using our new GMsFEM with 16 multiscale basis functions, and Figure IV.4d shows the difference between p_{GMsFEM} and the reference fine-scale solution p_0.

The two coarse-scale solutions use exactly the same number of degrees of freedom,

yet it is obvious that our new GMsFEM-based solver is significantly more accurate than the GFEM-based solver. The errors ε of these two coarse-scale solutions are 58% and 6.4% for the GFEM-based solver and GMsFEM-based solver, respectively. Meanwhile, the computational time for obtaining the reference fine-scale solution is 34.8 s, and the computational time for obtaining the GFEM and GMsFEM solutions are 109.1 and 11.9 s, respectively.

For completeness, we summarize the parameter settings, degrees of freedom, computational time and accuracy of the fine-scale reference FEM solution and the coarse-scale GFEM and GMsFEM solutions for Mesh 1 and Mesh 2 in Tables IV.1 and IV.2, respectively.

Both GFEM-based and GMsFEM-based solvers use much fewer degrees of freedom N compared to the conventional FEM, and the value of N is determined jointly by the number of elements and the number of basis functions. On both Mesh 1 and Mesh 2, the relative error of the coarse-scale solutions decreases using more basis functions, but the computation time also increases correspondingly. We find that our GMsFEM can generate much more accurate solutions using the same number of basis functions compared with the GFEM. For instance, the L_2-norm error of the GFEM solution on Mesh 1 is 6.2% using 16 multiscale basis functions with a 15 Hz source frequency, and 58% with a 20 Hz source frequency. In contrast, the error of our new GMsFEM solution with the same number of multiscale basis functions at 15 Hz is only 1%, and 6.4% at 20 Hz, showing a clear advantage of our new GMsFEM over the GFEM. For the solutions on Mesh 2 summarized in Table IV.2, we can obtain similar conclusions.

We also note that our GMsFEM can significantly reduce the computational time for solving the Helmholtz equation compared to the traditional FEM. Table IV.1 shows that with 16 multiscale basis functions for Mesh 1, our new GMsFEM-based Helmholtz equation solver uses only 13.7 s CPU time compared with 34.5 s of that using the traditional

FEM, a reduction of about 60%. On Mesh 2, the time savings of our GMsFEM are also fairly obvious, and the time reduction is about 45%.

An interesting result we find through the statistics in both Tables IV.1 and IV.2 is that for GFEM, using more basis functions may result in prohibitively long computational time. For instance, on Mesh 1, the elapsed CPU time of GFEM with 16 basis functions at 15 Hz is 109 s, a value that is significantly longer than that of the traditional FEM (34.5 s). We find similarly large T values at 20 Hz on Mesh 1. 15 Hz and 20 Hz GFEM solutions with 9 basis functions on Mesh 2 suffer from similar problem. This phenomena is caused by the ill-conditioned coefficient matrix of the GFEM-based solver. Our GMsFEM-based solver in contrast does not generate such ill-conditioned matrix, hence we find a significant reduction in both degrees of freedom and computational time.

This result indicate that as a reduced-order method, GFEM can reduce the number of unknowns of the discrete system; however, it may introduce non-trivial additional computation cost to the solver because of the resulting ill-conditioned coefficient matrix, and finally becomes a fairly inefficient Helmholtz equation solver. In contrast, our GMsFEM-based Helmholtz equation solver can both reduce the number of unknowns and the total computational time, serving as a memory- and time-efficient Helmholtz equation solver.

IV.2.2 Complex heterogeneous model

In the second example, we validate our new GMsFEM-based Helmholtz equation solver using the Marmousi model. Figures IV.5(a) and IV.5(b) show the P-wave velocity c and density ρ of the Marmousi model, respectively. Both the velocity and the density models contain strong heterogeneities. The model is 10 km in horizontal direction and 2 km in depth, and contains $n_z \times n_x = 400 \times 2000$ fine elements. We set two types of coarse mesh: Mesh 1 contains $N_z \times N_x = 20 \times 100$ coarse elements and Mesh 2 contains $N_z \times N_x = 40 \times 200$ coarse elements. The source is placed at 0.2 km in depth and 5 km

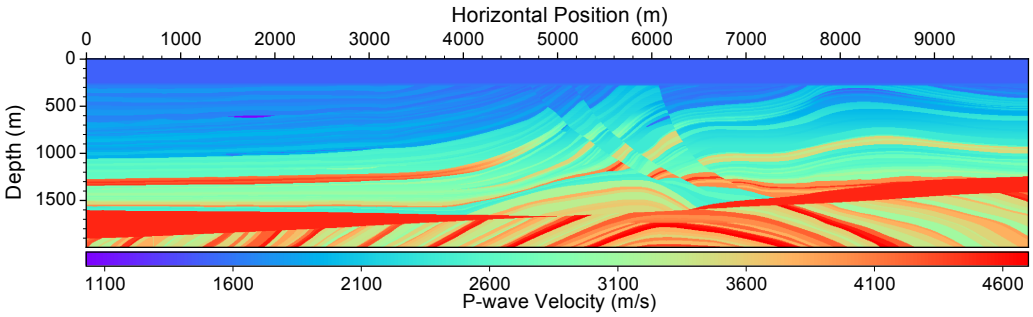

(a)

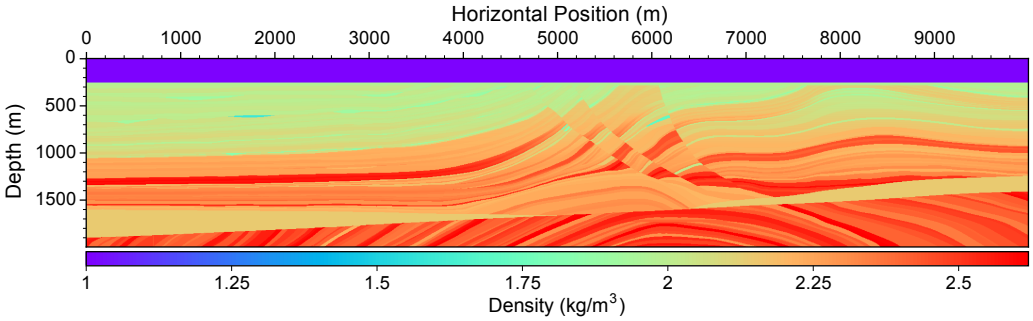

(b)

Figure IV.5: (a) P-wave velocity and (b) density of the Marmousi model.

in the horizontal direction. Same as the first example, we consider two source frequencies, 15 Hz and 20 Hz, to investigate the accuracy of the coarse-scale solutions.

Figure IV.6 shows the fine-scale reference FEM solution to the Helmholtz equation for the Marmousi model. The wavefield is fairly complicated due to the complex reflectors and heterogeneities in the Marmousi model.

We compute the coarse-scale solutions using the aforementioned GFEM- and GMsFEM-based Helmholtz solvers, and we show the solutions on Mesh 2 for visual comparison. Figures IV.7a and IV.7c shows the coarse-scale GFEM solutions on Mesh 2 at 15 Hz using 4 and 9 basis functions, respectively. The differences between the fine-scale reference solution and the GFEM solutions with 4 and 9 basis functions are shown in Figures IV.7b and IV.7d, respectively. In this highly heterogeneous model, GFEM with 4 basis functions

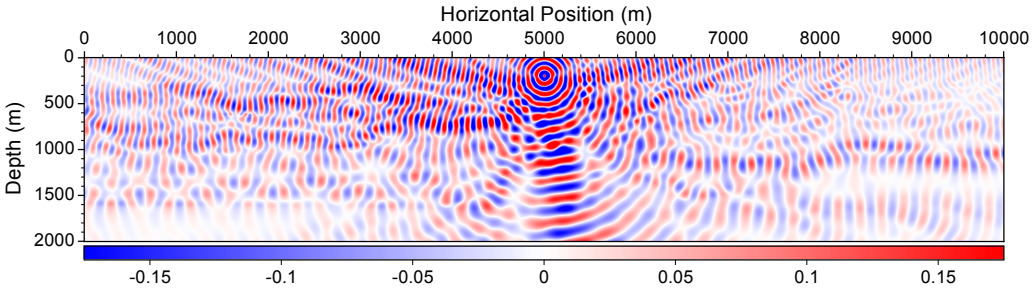

(a) Fine-scale reference solution

Figure IV.6: Fine-scale reference FEM solution of the Helmholtz equation for the Marmousi model. The source frequency is 15 Hz.

is rather inaccurate. Even with 9 basis functions, the error of GFEM-based solver is rather obvious, especially in the shallow part of the model as shown in Figure IV.7d.

In contrast, Figures IV.8a and IV.8c show the the GMsFEM-based solutions with 4 and 9 multiscale basis functions, respectively. Figures IV.8b and IV.8d show the differences between the reference solution and the GMsFEM solutions using 4 and 9 multiscale basis functions, respectively. Compared with those in Figure IV.7, our GMsFEM solutions are more accurate with the same number of degrees of freedom. The GMsFEM solution with 4 multiscale basis functions is not sufficiently accurate (with 81.9% relative error), but the GMsFEM solution with 9 basis functions deviates from the reference solution with only 4.2% relative error, compared with 27.6% of GFEM.

Similar with the first example, we give a complete comparison between the fine-scale reference FEM solution and the coarse-scale GFEM and GMsFEM solutions for the Marmousi model discretized with Mesh 1 and Mesh 2 in Tables IV.3 and IV.4, respectively.

We obtain similar conclusions as for the first example. The computation of the reference fine-scale FEM solutions takes about 34 s. On Mesh 1, both GFEM- and GMsFEM-based Helmholtz equation solvers can significantly reduce the computation time using 4, 9 or 16 basis functions. However, because of the strong heterogeneities, neither GFEM nor

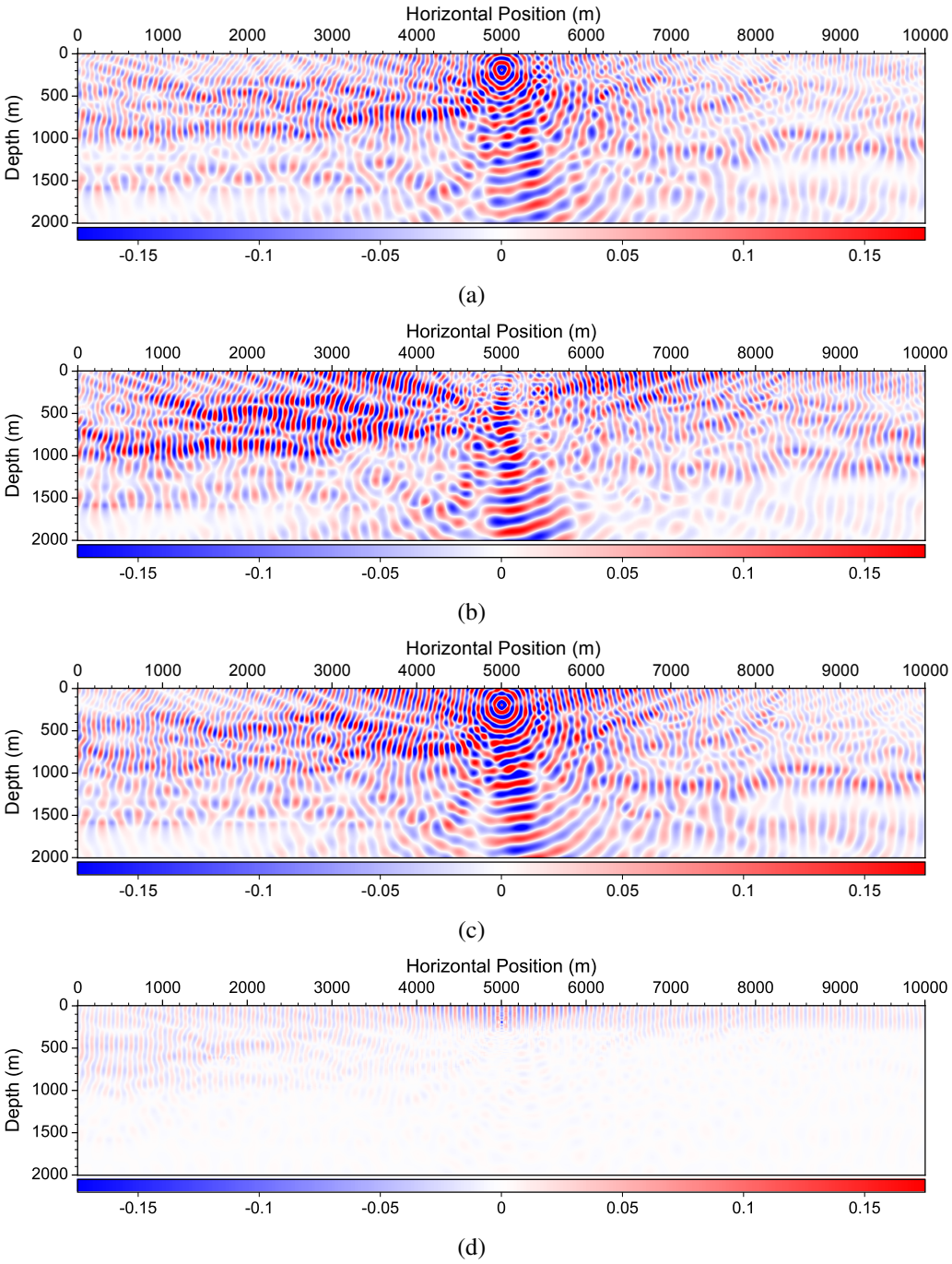

Figure IV.7: GFEM solutions to the Helmholtz equation on Mesh 2. The source frequency is 15 Hz. (a) GFEM solution with 4 polynomial basis functions, the relative error is 112.5%, and (b) the absolute difference between (a) and the reference solution; (c) GFEM solution with 9 polynomial basis functions, the relative error is 27.6%, and (d) the absolute difference between (c) and the reference solution.

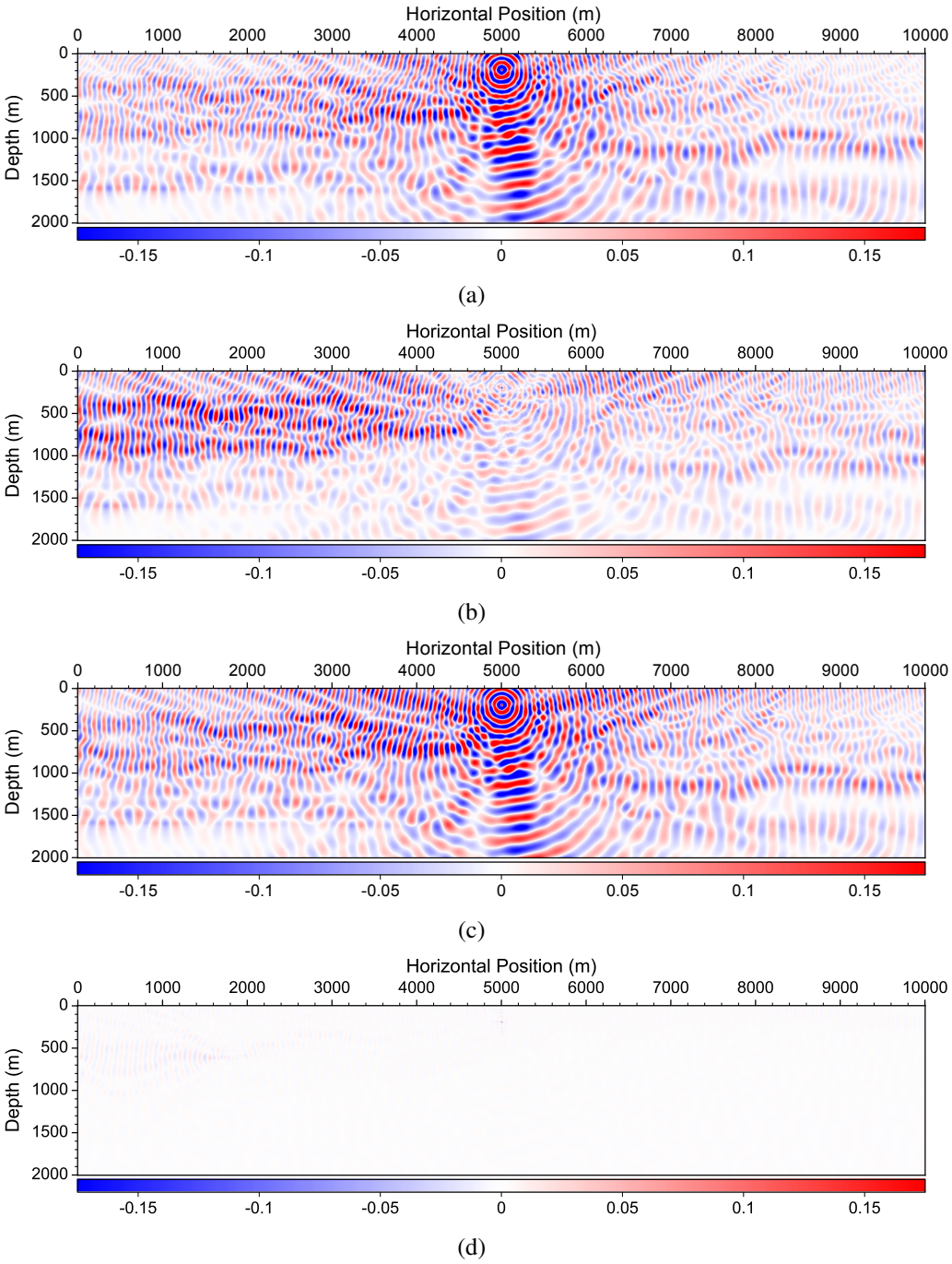

Figure IV.8: GMsFEM solutions to the Helmholtz equation Mesh 2. The source frequency is 15 Hz. (a) GMsFEM solution with 4 polynomial basis functions, the relative error is 81.9%, and (b) the absolute difference between (a) and the reference solution; (c) GMsFEM solution with 9 multiscale basis functions, the relative error is 4.2%, and (d) the absolute difference between (c) and the reference solution.

Solution type	15 Hz				20 Hz			
	N_b	N	T (s)	ε	N_b	N	T (s)	ε
FEM reference	/	1105041	34.4	/	/	1105041	35.5	/
GFEM	4	11556	0.4	1.681	4	11556	0.3	1.544
GFEM	9	26001	2.6	1.299	9	26001	2.4	1.607
GFEM	16	46224	17.8	0.940	16	46224	19.5	1.382
GMsFEM	4	11556	0.4	2.099	4	11556	0.4	1.269
GMsFEM	9	26001	2.2	1.166	9	26001	2.6	1.331
GMsFEM	16	46224	7.9	0.381	16	46224	9.1	0.926
Adaptive GMsFEM	10.0	28923	3.6	0.426	10.0	28923	4.0	1.133
Adaptive GMsFEM	15.9	45990	9.9	0.089	15.9	45990	10.4	0.439

Table IV.3: A comparison of the fine-scale FEM solution and the coarse-scale GFEM and GMsFEM solutions on Mesh 1 of the Marmousi model. N_b, N, T and ε are explained in Table IV.1. Mesh 1 contains $N_z \times N_x = 20 \times 100$ coarse elements.

GMsFEM produces sufficiently accurate results, even with 16 multiscale basis functions: the error of the GFEM-based solution is about 94% for 15 Hz source, while the error of the GMsFEM-based solution is about 38.1%, both are too far away from the reference solution. For 20 Hz source, the errors are even larger. Because the accuracy of the solution with either GFEM or GMsFEM is directly determined by the number of basis functions used for the solution, we infer that the insufficient accuracy of the coarse-scale solutions is probably caused by the insufficient number of basis functions for coarse elements with low velocity values.

To produce more accurate solutions using our GMsFEM-based solver, we assign different numbers of multiscale basis functions to different coarse blocks based on the velocity values in these coarse elements. The number of basis functions selected in each neighborhood (Figure IV.9b) is inverse proportional to the harmonic average velocity of the neighborhood (Figure IV.9a). Results in Table IV.3 show that the adaptive GMsFEM-based solutions are far more accurate that those of the rudimentary GMsFEM with fixed number of basis functions in all coarse blocks. For 15 Hz source, the error of the adap-

Solution type	15 Hz				20 Hz			
	N_b	N	T (s)	ε	N_b	N	T (s)	ε
FEM reference	/	1105041	34.4	/	/	1105041	35.5	/
GFEM	4	45156	1.9	1.125	4	45156	2.0	1.551
GFEM	9	101601	15.4	0.276	9	101601	14.1	1.283
GMsFEM	4	45156	2.0	0.819	4	45156	2.1	1.254
GMsFEM	9	101601	12.6	0.042	9	101601	12.5	0.259
Adaptive GMsFEM	5.2	58401	4.7	0.107	5.2	58401	4.6	0.331
Adaptive GMsFEM	8.4	94567	14.2	0.021	8.4	94567	13.3	0.159

Table IV.4: A comparison of the fine-scale FEM solution and the coarse-scale GFEM and GMsFEM solutions on Mesh 2 of the Marmousi model. N_b, N, T and ε are explained in Table IV.1. Non-integer value for N_b represents the average value of basis functions number per coarse neighborhood. Mesh 2 contains $N_z \times N_x = 40 \times 200$ coarse elements.

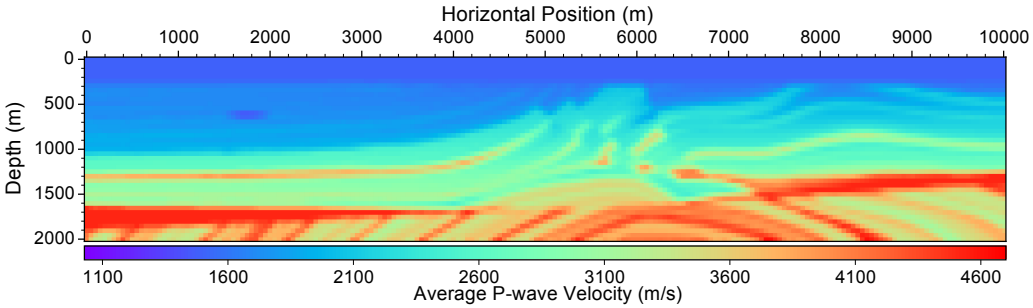

(a)

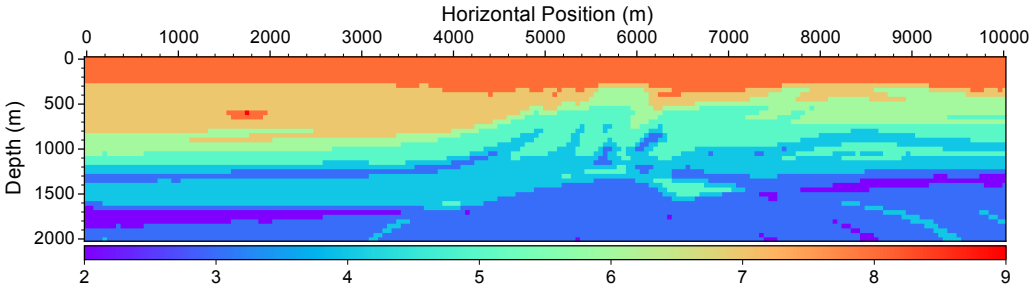

(b)

Figure IV.9: (a) Average velocity values in each coarse element of Mesh 2, and (b) the distribution of number of multiscale basis functions used for each coarse element on Mesh 2. The maximum number of multiscale basis functions is 9. The number of basis functions are computed based on the average velocity values in (a). Large-velocity blocks use fewer basis functions, and more basis functions if lower-velocity.

tive GMsFEM solution with average 15.9 multiscale basis functions is only about 8.9%, compared with 38.1% of the GMsFEM-based solution with 16 fixed number of multiscale basis functions. For 20 Hz source solutions, none of GFEM, GMsFEM and adaptive GMsFEM solutions is sufficiently accurate, but our adaptive GMsFEM provides the most accurate solution. Obviously, more multiscale basis functions should be used to improve the accuracy.

We obtain similar conclusions for Mesh 2 with those on Mesh 1 by comparing the FEM, GFEM, GMsFEM and adaptive GMsFEM solutions shown in Table IV.4. It is obvious that the our new GMsFEM-based solver can approximate the reference solution with much higher accuracy compared with the GFEM-based solver. Table IV.3 and Table IV.4 also indicate that using similar number of degrees of freedom and computational time, the adaptive GMsFEM that uses different numbers of multiscale basis functions in different coarse blocks can be more accurate than the GMsFEM that uses a fixed number of multiscale basis functions in every coarse block.

IV.3 Concluding remarks

We develop a GMsFEM for Helmholtz equation by using multiscale basis functions. We construct the basis function space by selecting the eigenfunctions corresponding to several smallest eigenvalues obtained from local eigenvalue problem. With these basis functions, we can greatly reduce the dimension of the coefficient matrix for Helmholtz equation. We show by two examples with a homogeneous model and Marmousi model that our method can greatly reduce the dimension of the system and computational time with very small error. Future work includes extending our method to 3D and elastic Helmholtz equations.

V. REVERSE TIME MIGRATION BASED ON GENERALIZED MULTISCALE FINITE ELEMENT FORWARD MODELING *

V.1 Introduction

Wave equation imaging and inversion methods offer strong potential for providing detailed, accurate insights into subsurface structure. By avoiding the limits of algorithms based on asymptotic ray theory, such approaches are able to utilize complex, multiple arrivals from the seismic wavefield to generate solutions [52]. Reverse time migration (RTM) has been developed as a wave equation approach to improve seismic imaging in areas of complex structure [12, 62, 86, 15, 77, 56]. In addition to exploration tasks, it has found applications in larger scale crustal imaging [74].

RTM relies on full waveform modeling of both the recorded wavefield and the seismic waves generated by the source, so the solution can be computationally expensive, especially when applying conventional finite difference methods. Recent work has proposed several approaches to accelerate modeling to reduce computational cost. For example, in [74] Fomel proposed a wavefield extrapolation based on a lowrank approximation of a space-wavenumber matrix symbol that estimates a small set of locations and wavenumbers that provide a reliable solution. Another important method is that of Nunes and Minkoff [65], who apply subgrid upscaling to accelerate wave equation solutions by carrying out part of the computation on a coarse grid that incorporates the influence of heterogeneity present on a detailed, fine grid model [57, 78, 79]. Both of these general approaches can be considered as forms of model reduction.

We apply a different multiscale method as a computational engine for RTM. This al-

*This chapter is reprinted with permission from "Fast solver for Helmholtz equation using multiscale basis functions" by Gibson Jr, Richard L., and Shubin Fu, 2015. SEG Technical Program Expanded Abstracts 2015, pp. 4137-4142. Copyright [2017] by SEG.

gorithm, the generalized multiscale finite element method (GMsFEM), is similar to the operator-based approach of Korostyshevskaya and Minkoff [57]. While traditional finite element schemes will apply, for example, arbitrary polynomial bases, the main idea of GMsFEM [36, 26] is to instead use a fine scale grid to solve for basis functions that are in turn used to solve the wave equation on a coarse grid defined on the same model domain. These bases are determined by solving physically based spectral problems and therefore capture the influence of fine-scale heterogeneity. Selecting only the most dominant modes from these spectral problems leads to a reduced-order approximation of the solution without sacrificing the accuracy. In contrast to the operator-based upscaling approach [78], which requires solutions on the fine-grid at each time step, another key advantage of GMsFEM is that the computation of basis functions is done only once for any proposed earth model. This creates tremendous advantages for RTM, where solutions must be computed not only for a large number of sources and receivers, but also potentially to sample many proposed velocity models.

In this chapter, we will first review the GMsFEM algorithm for acoustic media to help explain its implementation and how it can lead to significant reductions in computational cost. We then show for the first time imaging results obtained when using GMsFEM for RTM with a simple test model and show that not only can the GMsFEM generate accurate migration images, but it can be used straightforwardly to generate approximate solutions that are obtained rapidly but are still accurate enough to identify optimal velocity models.

V.2 Method

Our goal is to implement a new multiscale reverse time migration algorithm using the acoustic wave equation

$$\frac{1}{\kappa}\frac{\partial^2 u}{\partial t^2} = \nabla \cdot (\frac{1}{\rho}\nabla u) + f \tag{V.1}$$

where ρ is the density and κ is bulk modulus. We implement RTM in a conventional way, by first numerically simulating forward propagation of the acoustic wavefield from the source to the subsurface space. We then time reverse the data recorded at receivers, and back propagated that recorded wavefield into the image space. The migration output is simply the crosscorrelation of these two wavefields at each image point. Our primary emphasis is to explore the application of GMsFEM to achieve more rapid results, and further developments could examine more complex image conditions [58].

In summary, the GMsFEM approach we use has several key conceptual points:

1. The model domain Ω has a fine grid with potentially complex, high contrast heterogeneity, and a coarse grid is superposed on that mesh

2. In an *offline stage*, basis functions are computed for each coarse mesh cell once for a velocity model

3. In an *online stage*, a discontinuous Galerkin algorithm applies the basis functions to simulate propagation on the coarse grid.

There are significant savings in CPU time, both because of the model reduction achieved by solving the wave equation on a coarsened mesh and because the bases are only computed in the offline stage. For RTM, this means they are only computed one time for the velocity model of interest; the same bases are used for all sources and for backpropagation of all data. This is especially important for large problems, and the offline cost becomes a negligible part of the computational effort. In addition, if the velocity model is updated in some portion of the model, the bases need only be recomputed in that region.

Below we summarize the most important aspects of the GMsFEM for acoustic waves [26], noting that we have also implemented the algorithm for elastic, anisotropic media [43].

V.2.1 Discontinuous Galerkin solution: online stage

Though the final algorithm will carry out the offline stage first, we begin the discussion of the method by outlining the discontinuous Galerkin algorithm used for the online stage on the coarse grid to help motivate the need for basis functions. We discretize Ω into a set of coarse grid blocks and then divide each block into a finer grid (Figure V.1). Let $\mathcal{T}_H$ be the set of all coarse grid blocks, and $\mathcal{E}_H$ will be all edges of interior coarse elements. Then there are N coarse grid blocks, and the number of fine grid nodes on the boundary of each coarse cell is n_p. For each interior coarse grid edge $e \in \mathcal{E}_H$, the average of some quantity v on e is $\{v\}_e = \frac{v^+ + v^-}{2}$, and the discontinuity of some u is $[u]_e = u^+ - u^-$, where $u^\pm = u|_{K^\pm}$. K^- and K^+ are the two coarse grid blocks sharing the common coarse edge e. We assume that the normal vector on e is pointing from K^+ to K^-. In addition, for the coarse edge e that lies on the boundary $\partial\Omega$, we define $\{v\}_e = v$ and $[u]_e = u$ assuming the unit normal vector on e is pointing outside the domain.

We will apply the symmetric Interior Penalty Discontinuous Galerkin (IPDG) method [46] to develop a discretized solution. Let $V_H = \{\phi_i\}_{i=1}^{N_b}$ be a finite dimensional function space that is made up of basis functions $\phi_i(x)$ that are continuous inside each coarse grid block but are in general discontinuous across coarse grid edges globally. Then, the IPDG method is: find $u_H \in V_H$ such that

$$\int_\Omega \frac{1}{\kappa} \frac{\partial u_H}{\partial t^2} v + a_{DG}(u_H, v) = \int_\Omega f\, v, \qquad \forall\, v \in V_H, \tag{V.2}$$

where the bilinear form $a_{DG}(u,v)$ is defined by

$$\begin{aligned} a_{DG}(u,v) &= \sum_{K\in\mathcal{T}^H}\int_K \frac{1}{\rho}\nabla u\cdot\nabla v + \sum_{e\in\mathcal{E}^H}\Big(-\int_e \{\frac{1}{\rho}\nabla u\cdot n\}_e\,[v]_e \\ &\quad -\int_e \{\frac{1}{\rho}\nabla v\cdot n\}_e\,[u]_e + \frac{\gamma}{h}\int_e \frac{1}{\rho}[u]_e\,[v]_e\Big) \end{aligned}$$

where $\gamma > 0$ is a penalty parameter and n denotes the unit normal vector on e. Expressing u_H by $u_H(x,z,t) = \sum_{i=1}^{N_b} d_i(t)\phi_i(x)$, then equation (V.2) in matrix form is

$$M\frac{d^2U}{dt^2} + KU = F \tag{V.3}$$

where the mass matrix M, stiffness matrix K and the right hand side vector F are

$$M_{ij} = \int_\Omega \frac{1}{\kappa}\phi_j\,\phi_i, \quad K_{ij} = a_{DG}(\phi_j,\phi_i), \quad F_i = \int_\Omega f\,\phi_i. \tag{V.4}$$

U is a vector defined by $U = (d_i(t))$. Let $\Delta t > 0$ be the time step size and let $U^n = (d_i(t_n))$. We use the classic second order central finite difference method for the time discretization. The fully discretized problem is to find U^{n+1} such that

$$M\frac{U^{n+1} - 2U^n + U^{n-1}}{\Delta t^2} + KU^n = F^n. \tag{V.5}$$

V.2.2 Computation of basis functions: offline stage

The online stage utilizes the discretized solution V.5, but it requires the calculation first of the basis functions that form the basis space V_H. We decompose the space $V_H(K)$ into two orthogonal components, $V_H(K) = V_H^1(K) + V_H^2(K)$. The first, $V_H^1(K)$, is determined

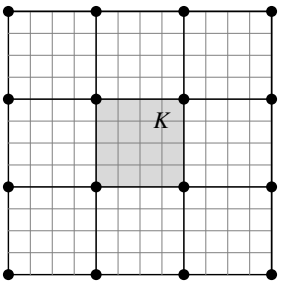

Figure V.1: A sketch of the mesh, where K is an example of coarse grid block, and the thin lines show the fine mesh blocks.

as follows. For a given fine grid node x_i on the boundary of K, we first solve

$$\nabla \cdot (\rho^{-1} \nabla w_{i,K}) = 0 \tag{V.6}$$

with the Dirichlet boundary condition $w_{i,K}(x_i) = \delta_{i,j}$ on ∂K . Let

$$\widetilde{V}_H^1(K) = \text{span}\{w_{1,K}, \cdots, w_{n_p,K}\}.$$

Not all of these functions are required, and we will use a local spectral problem to identify the most important. This spectral problem is

$$\frac{1}{h} \int_{\partial K} q_\mu v = \mu \int_K \frac{1}{\rho} \nabla q_\mu \cdot \nabla v, \qquad \forall\, v \in \widetilde{V}_H^1(K). \tag{V.7}$$

We sort the eigenvalues μ in decreasing order, namely, $\mu_1 \geq \mu_2 \cdots$ and the corresponding eigenfunctions are denoted by q_i. The most dominant mode is represented by the eigenfunctions with large eigenvalue. We select the first L_i eigenfunctions so that the sum of the corresponding eigenvalues is a large percentage of the total energy E, which is the sum of all eigenvalues. The space $V_H^1(K)$ is then spanned by the functions $q_{i,j}$, $i = 1, 2, \cdots, L_i, j = 1, 2, \cdots, N$. Because these functions are computed by variations in

boundary conditions, they are referred to as *boundary basis functions*.

The space $V_H^2(K)$ is designed to capture the interior modes of each coarse grid block from the solution of the eigenvalue problem $z_\lambda = -\lambda\nabla\cdot(\rho^{-1}\nabla z_\lambda)$ with zero Dirichlet boundary condition. As before, we order the eigenvalues and choose the most dominant modes to construct multiscale basis functions; those determined from this approach are *interior basis functions*.

The cost of GMsFEM is $O(n_b^2 N^2)$, where n_b is the number of basis selected on each coarse block, while the cost of FEM on fine gird is $O(N_f)$, where N_f is the total elements of the fine grid. We can see that if n_b is small, GMsFEM can be much faster than FEM.

V.3 RTM example results

We use a simple heterogeneous model to test the RTM with GMsFEM (Figure V.2). The model, which includes two high contrast, thin layers with an anticline-like structure and a thin, horizontal layer, is comparatively simple to make it easy to identify artifacts and potential errors in migration images. It is 2000 m horizontally and vertically, and the coarse grid has 50×50 cells that are 40 m on each side. The fine grid has square cells that are 4 m in size and is 500×500. The background velocity and density are 2500 m/s and 2400 kg/m^3, while the velocity and density for the anticline layers are 2650 m/s and 2500 kg/m^3, and the velocity and density of the thin horizontal layer are 3000 m/s and 3000 kg/m^3. We computed synthetic seismograms using a Ricker wavelet with central frequency 30 Hz. Therefore, there are only two coarse grid elements per wavelength at the central frequency and the minimum wavelength is the same as the coarse cell dimension. The full set of synthetic seismograms used 51 sources on the upper surface, located from x=0 m to x=2000 m at equal increments in distance. The results were computed for 101 receivers equally spaced on the upper surface. The synthetic data were calculated using a first order FEM method on the fine grid, and the direct waves were muted prior to migration. The

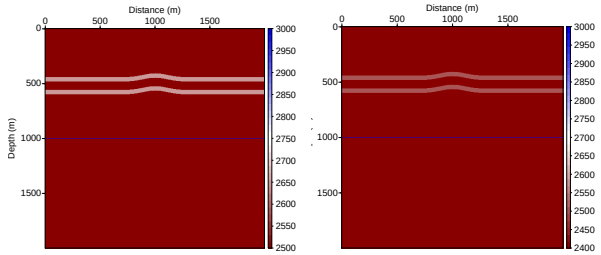

(a) Velocity (m/s) (b) Density (kg/m^3)

Figure V.2: Earth model used to test RTM results.

RTM image was then generated for the entire model domain.

We first test the influence of the number of basis functions on RTM images using GMsFEM. Utilizing a smaller number of bases will normally produce less accurate (more approximate) results, but computation time will decrease too. A comparison of the RTM images computed with the reference FEM solution on the fine grid with those from GMsFEM using 8, 12 and 16 total basis functions illustrates these tradeoffs (Figure **??**). In each case, we apply equal numbers of boundary and interior bases. This first test applied a homogeneous migration velocity model with the correct background velocity, 2500 m/s. A visual comparison suggests that the image result with 16 basis functions is essentially the same as the reference image (Figures V.3a, V.3d). The image for 8 basis functions (Figures V.3b) has oscillations suggesting dispersion errors. Measuring the difference between multiscale and fine-scale images using the $L2$ norm, the results for 8, 12 and 16 bases are 45.2%, 11.6% and 4.7%, respectively. The small discrepancy for 16 basis functions confirms the accuracy of that result. Computation times decreased by 80.1%, 64.2% and 38.3% for these same numbers of bases; here the time ratio does include the offline cost as well as the online simulation time. These times can be further reduced for GMsFEM-RTM if bases were computed in a parallel manner; since each coarse cell is independent for the offline stage, it is embarrassingly parallel.

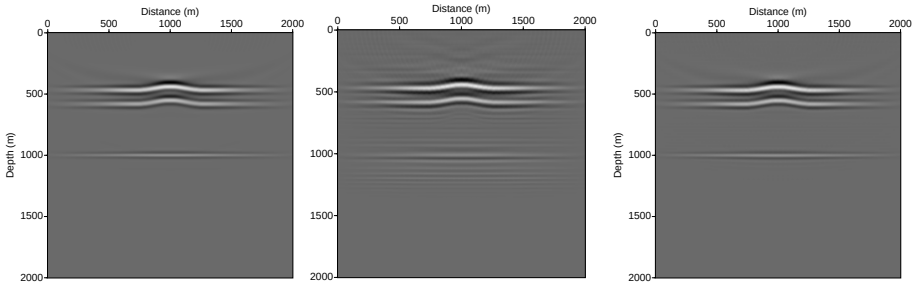

(a) RTM result with FEM on fine grid

(b) RTM result with GMsFEM using 8 bases

(c) RTM result with GMsFEM using 12 bases

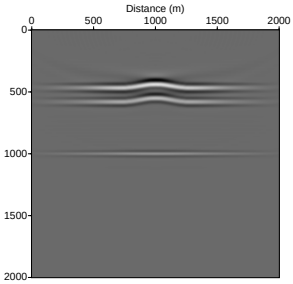

(d) RTM result with GMsFEM using 16 bases

Figure V.3: Comparision of RTM results from the fine grid solution and from GMsFEM with different numbers bases when using a homogeneous migration velocity equal to the background velocity in Figure V.2, 2500 m/s.

As a point of comparison, we also show examples of GMsFEM-RTM images when the migration velocity model includes that two thin anticline layers (Figure V.4). In this case, the results are very similar to those obtained with the homogeneous velocity model (Figure V.3). A close examination does show that there are some subtle artifacts present when the more detailed velocity model is applied, especially near the upper surface of the image space. This is not surprising, since it is known that including high contrast features in the velocity model can create such artifacts with RTM [58].

These previous results help to demonstrate the potential savings in computational cost if we employ GMsFEM as the computational engine in the migration work flow. However,

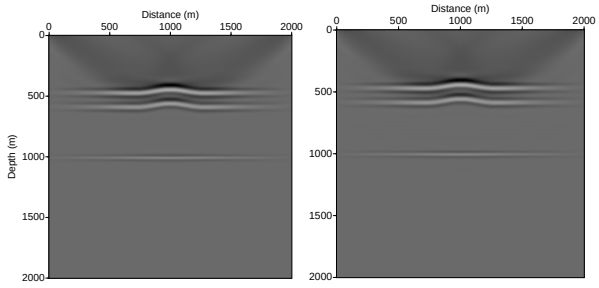

(a) RTM result with FEM on fine grid

(b) RTM result with GMsFEM with 16 bases

Figure V.4: Comparison of RTM results from the reference, fine-grid FEM and the GMsFEM-RTM using 16 bases. The RTM utilized a velocity that included the two shallow, anticline layers (Figure V.2).

this work flow will often include the task of completing migrations with a range of velocity models to select an optimal migration velocity field. In this case, a primary goal may be to rapidly generate trial results for many models, many of which will be inadequate for quality migrations. While applying GMsFEM-RTM with a low number of bases will include some errors such as those seen in Figure V.3b, the results do show that the images still produce a correct overall structural image with a significant decrease in CPU time. This suggests that computing a set of images for a range of trial velocities with a small number of bases may be an effective means of selecting migration velocities. To demonstrate this, we present the migration images generated with only 8 basis functions but for two cases, one with a velocity field that is too slow (2000 m/s) and one that is too fast (3000 m/s). Figures V.5 and V.6 compare these GMsFEM results to the corresponding fine-grid reference results. While the artifacts in the GMsFEM result are evident, the general spatial structure of the features in the images are still correct and would allow a selection of the optimal velocity model.

The tradeoff in computational speed and accuracy in these images can be controlled by varying the number of bases. Once the velocity model is determined, increasing the num-

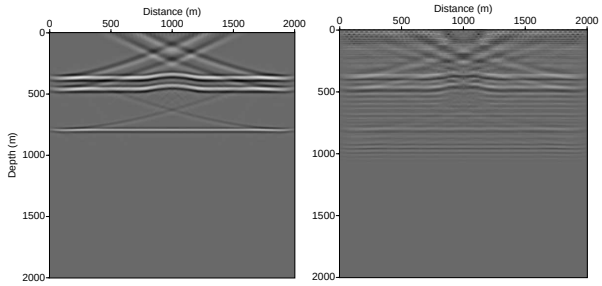

(a) RTM result with FEM on fine grid

(b) RTM result with GMsFEM with 8 bases

Figure V.5: Comparison of RTM results with FEM and GMsFEM with 8 bases using a migration velocity equal to 2000 m/s (the correct value is 2500 m/s).

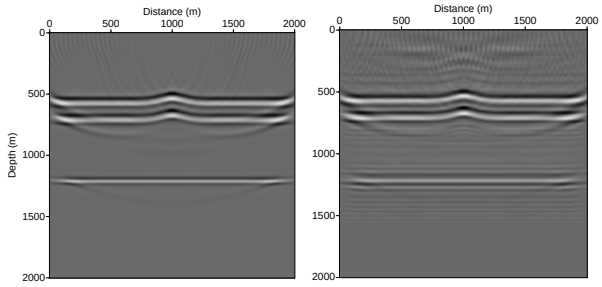

(a) RTM result with FEM on fine grid

(b) RTM result with GMsFEM with 8 bases

Figure V.6: Comparison of RTM results with FEM and GMsFEM with 8 bases using a migration velocity equal to 3000 m/s (the correct value is 2500 m/s).

ber of bases for later results will allow more reliable estimation of not only the general structural image, but also more subtle variations in amplitude or geometry that are indicative of stratigraphic features. In addition, it is possible to apply spatial adaptivity in the basis function computations. Specifically, tests using the elastic GMsFEM show that normally fewer bases can be used when average velocity in a coarse cell is larger [43]. This is consistent with the results above that show larger dispersion errors when the number of bases begins to be too small. Applying the larger number of basis functions only where

required by lower velocities, and smaller wavelengths, will help to gain computational speed in imaging.

V.4 Concluding remarks

The GMsFEM algorithm for acoustic wave propagation utilizes basis functions computed from materials properties specified on a fine, heterogeneous model grid to simulate propagation on a coarse grid. We show the first results of applying this method to RTM, and the examples demonstrate how the selection of basis functions can be tuned to obtain faster, though somewhat less accurate migration images. Increasing the number of bases reduces artifacts with an increase in computational cost, but the results are still obtained more rapidly than with a comparable computation applied on the original fine grid. In addition, utilizing a small number of bases can help to rapidly test a number of velocity models to optimize the migration model prior to computing more detailed migration images, thereby producing a significant savings in the total time required for the migration work flow.

VI. CONCLUSIONS

In this dissertation, we study some applications of the GMsFEM. We now summarize each component.

In Chapter II, the GMsFEM for the second-order formulation of the static linear elasticity equation in in high contrast media is investigated. We consider continuous Galerkin and discontinuous Galerkin coupling methods. For both methods, we systemically study the main ingredients of the GMsFEM. We introduce the construction of snapshot space, offline space and oversampling. We also provide convergence analysis for both coupling techniques. Numerical results are presented to verify the efficiency of our method.

In Chapter III, we study the HDG-GMsFEM for the first-order formulation of the static linear elasticity equation in in high contrast media. We discuss three methods of constructing the edge-based multiscale basis. We demonstrated the efficiency and robustness these methods with two highly heterogeneous model. The oversampling and randomized snapshot techniques are also considered. In addition, the applications of our method for the nearly incompressible media are shown.

In Chapter IV, the GMsFEM for the helmholtz in variable density media is introduced. We systemically study the performance of the GMsFEM in terms of computational cost with a homogeneous and heterogeneous model. We show the advantages of using spectral basis functions instead of polynomials. Adaptive GMsFEM based on the velocity distribution is adopted in numerical experiments, which further reduce the coarse system.

In Chapter V, we consider a more practical application of GMsFEM. We apply the GMsFEM for the reverse time migration, a very popular method of seismic imaging. The numerical examples demonstrate how the selection of basis functions can be tuned to obtain faster, though somewhat less accurate migration images. In addition, utilizing a small

number of bases can help to rapidly test a number of velocity models to optimize the migration model prior to computing more detailed migration images, thereby producing a significant savings in the total time required for the migration work flow.

REFERENCES

[1] Assyr Abdulle. Analysis of a heterogeneous multiscale FEM for problems in elasticity. *Mathematical Models and Methods in Applied Sciences*, 16(04):615–635, 2006.

[2] Assyr Abdulle and Marcus J Grote. Finite element heterogeneous multiscale method for the wave equation. *Multiscale Modeling & Simulation*, 9(2):766–792, 2011.

[3] Grégoire Allaire and Robert Brizzi. A multiscale finite element method for numerical homogenization. *Multiscale Modeling & Simulation*, 4(3):790–812, 2005.

[4] Rodolfo Araya, Christopher Harder, Diego Paredes, and Frédéric Valentin. Multiscale hybrid-mixed method. *SIAM Journal on Numerical Analysis*, 51(6):3505–3531, 2013.

[5] Todd Arbogast. Analysis of a two-scale, locally conservative subgrid upscaling for elliptic problems. *SIAM Journal on Numerical Analysis*, 42(2):576–598, 2004.

[6] Todd Arbogast, Gergina Pencheva, Mary F Wheeler, and Ivan Yotov. A multiscale mortar mixed finite element method. *Multiscale Modeling & Simulation*, 6(1):319–346, 2007.

[7] Douglas Arnold, Richard Falk, and Ragnar Winther. Mixed finite element methods for linear elasticity with weakly imposed symmetry. *Mathematics of Computation*, 76(260):1699–1723, 2007.

[8] Douglas N Arnold, Franco Brezzi, and Jim Douglas. PEERS: a new mixed finite element for plane elasticity. *Japan Journal of Applied Mathematics*, 1(2):347–367, 1984.

[9] I. Babuška and J. M. Melenk. The partition of unity method. *Int. J. Numer. Meth. Engrg.*, 40:727–758, 1997.

[10] Ivo Babuška, Frank Ihlenburg, Ellen T Paik, and Stefan A Sauter. A generalized finite element method for solving the Helmholtz equation in two dimensions with minimal pollution. *Computer methods in applied mechanics and engineering*, 128(3-4):325–359, 1995.

[11] Ivo Babuška and Manil Suri. On locking and robustness in the finite element method. *SIAM Journal on Numerical Analysis*, 29(5):1261–1293, 1992.

[12] Edip Baysal, Dan D Kosloff, and John WC Sherwood. Reverse time migration. *Geophysics*, 48(11):1514–1524, 1983.

[13] Jean-Pierre Berenger. A perfectly matched layer for the absorption of electromagnetic waves. *Journal of computational physics*, 114(2):185–200, 1994.

[14] Gal Berkooz, Philip Holmes, and John L Lumley. The proper orthogonal decomposition in the analysis of turbulent flows. *Annual review of fluid mechanics*, 25(1):539–575, 1993.

[15] Biondo Biondi and Guojian Shan. Prestack imaging of overturned reflections by reverse time migration. In *SEG Technical Program Expanded Abstracts 2002*, pages 1284–1287. Society of Exploration Geophysicists, 2002.

[16] Christopher E Brennen. *Fundamentals of multiphase flow*. Cambridge university press, 2005.

[17] Susanne Brenner and Ridgway Scott. *The mathematical theory of finite element methods*, volume 15. Springer Science & Business Media, 2007.

[18] Susanne C Brenner and Li-Yeng Sung. Linear finite element methods for planar linear elasticity. *Mathematics of Computation*, 59(200):321–338, 1992.

[19] Romain Brossier, Stéphane Operto, and Jean Virieux. Seismic imaging of complex onshore structures by 2D elastic frequency-domain full-waveform inversion. *Geophysics*, 74(6):WCC105–WCC118, 2009.

[20] Marco Buck, Oleg Iliev, and Heiko Andrä. Multiscale finite element coarse spaces for the application to linear elasticity. *Central European Journal of Mathematics*, 11(4):680–701, 2013.

[21] Victor M Calo, Eric T Chung, Yalchin Efendiev, and Wing Tat Leung. Multiscale stabilization for convection-dominated diffusion in heterogeneous media. *Computer Methods in Applied Mechanics and Engineering*, 304:359–377, 2016.

[22] Li-Qun Cao. Iterated two-scale asymptotic method and numerical algorithm for the elastic structures of composite materials. *Computer methods in applied mechanics and engineering*, 194(27):2899–2926, 2005.

[23] Z. Chen and T.Y. Hou. A mixed multiscale finite element method for elliptic problems with oscillating coefficients. *Mathematics of Computation*, 72:541–576, 2002.

[24] Zhongying Chen, Tingting Wu, and Hongqi Yang. An optimal 25-point finite difference scheme for the Helmholtz equation with PML. *Journal of Computational and Applied Mathematics*, 236(6):1240–1258, 2011.

[25] Chunlei Chu and Paul L Stoffa. An implicit finite-difference operator for the Helmholtz equation. *Geophysics*, 77(4):T97–T107, 2012.

[26] Eric T Chung, Yalchin Efendiev, and Shubin Fu. Generalized multiscale finite element method for elasticity equations. *GEM-International Journal on Geomathematics*, 5(2):225–254, 2014.

[27] Eric T Chung, Yalchin Efendiev, and Chak Shing Lee. Mixed generalized multiscale finite element methods and applications. *Multiscale Modeling & Simulation*,

13(1):338–366, 2015.

[28] Eric T Chung, Yalchin Efendiev, and Wing Tat Leung. Generalized multiscale finite element methods for wave propagation in heterogeneous media. *Multiscale Modeling & Simulation*, 12(4):1691–1721, 2014.

[29] Eric T Chung, Yalchin Efendiev, Wing Tat Leung, and Shuai Ye. Generalized multiscale finite element methods for space-time heterogeneous parabolic equations. *arXiv preprint arXiv:1605.07634*, 2016.

[30] Eric T Chung, Yalchin Efendiev, Guanglian Li, and Maria Vasilyeva. Generalized multiscale finite element methods for problems in perforated heterogeneous domains. *Applicable Analysis*, pages 1–26, 2015.

[31] Bernardo Cockburn, Jayadeep Gopalakrishnan, and Raytcho Lazarov. Unified hybridization of discontinuous Galerkin, mixed, and continuous Galerkin methods for second order elliptic problems. *SIAM Journal on Numerical Analysis*, 47(2):1319–1365, 2009.

[32] Bernardo Cockburn and Ke Shi. Superconvergent HDG methods for linear elasticity with weakly symmetric stresses. *IMA Journal of Numerical Analysis*, 33(3):747–770, 2013.

[33] Y. Efendiev, J. Galvis, and X.H. Wu. Multiscale finite element methods for high-contrast problems using local spectral basis functions. *Journal of Computational Physics*, 230:937–955, 2011.

[34] Y. Efendiev and A. Pankov. Numerical homogenization and correctors for nonlinear elliptic equations. *SIAM J. Appl. Math.*, 65(1):43–68, 2004.

[35] Y. Efendiev and A. Pankov. On homogenization of almost periodic nonlinear parabolic operators. *Int. J. Evol. Equ.*, 1(3):203–209, 2005.

[36] Yalchin Efendiev, Juan Galvis, and Thomas Y Hou. Generalized multiscale finite element methods (GMsFEM). *Journal of Computational Physics*, 251:116–135, 2013.

[37] Yalchin Efendiev and Thomas Y Hou. *Multiscale finite element methods: theory and applications*, volume 4. Springer Science & Business Media, 2009.

[38] Yalchin Efendiev, Raytcho Lazarov, Minam Moon, and Ke Shi. A spectral multiscale hybridizable discontinuous Galerkin method for second order elliptic problems. *Computer Methods in Applied Mechanics and Engineering*, 292:243–256, 2015.

[39] Björn Engquist, Henrik Holst, and Olof Runborg. Multiscale methods for wave propagation in heterogeneous media over long time. In *Numerical analysis of multiscale computations*, pages 167–186. Springer, 2012.

[40] Richard S Falk. Nonconforming finite element methods for the equations of linear elasticity. *Mathematics of Computation*, 57(196):529–550, 1991.

[41] Gilles A Francfort and François Murat. Homogenization and optimal bounds in linear elasticity. *Archive for Rational Mechanics and Analysis*, 94(4):307–334, 1986.

[42] Shubin Fu, Yalchin Efendiev, Kai Gao, and R Gibson. Multiscale modeling of acoustic wave propagation in 2D heterogeneous media using local spectral basis functions. In *SEG Technical Program Expanded Abstracts*, volume 2013, pages 3553–3558, 2013.

[43] Kai Gao, Shubin Fu, Richard L Gibson, Eric T Chung, and Yalchin Efendiev. Generalized multiscale finite-element method (GMsFEM) for elastic wave propagation in heterogeneous, anisotropic media. *Journal of Computational Physics*, 295:161–188, 2015.

[44] GHF Gardner, LW Gardner, and AR Gregory. Formation velocity and densitythe diagnostic basics for stratigraphic traps. *Geophysics*, 39(6):770–780, 1974.

[45] Stephen D Gedney. An anisotropic perfectly matched layer-absorbing medium for the truncation of fdtd lattices. *IEEE transactions on Antennas and Propagation*, 44(12):1630–1639, 1996.

[46] Marcus J Grote and Dominik Schötzau. Optimal error estimates for the fully discrete interior penalty DG method for the wave equation. *Journal of Scientific Computing*, 40(1):257–272, 2009.

[47] Johnny Guzmán. A unified analysis of several mixed methods for elasticity with weak stress symmetry. *Journal of Scientific Computing*, 44(2):156–169, 2010.

[48] Isaac Harari and Thomas JR Hughes. Galerkin/least-squares finite element methods for the reduced wave equation with non-reflecting boundary conditions in unbounded domains. *Computer methods in applied mechanics and engineering*, 98(3):411–454, 1992.

[49] Christopher Harder, Diego Paredes, and Frédéric Valentin. A family of multiscale hybrid-mixed finite element methods for the Darcy equation with rough coefficients. *Journal of Computational Physics*, 245:107–130, 2013.

[50] Jun Hu. A new family of efficient conforming mixed finite elements on both rectangular and cuboid meshes for linear elasticity in the symmetric formulation. *SIAM Journal on Numerical Analysis*, 53(3):1438–1463, 2015.

[51] Jun Hu, Hongying Man, and Shangyou Zhang. A simple conforming mixed finite element for linear elasticity on rectangular grids in any space dimension. *Journal of Scientific Computing*, 58(2):367–379, 2014.

[52] Yunsong Huang and Gerard T Schuster. Resolution limits for wave equation imaging. *Journal of Applied Geophysics*, 107:137–148, 2014.

[53] Thomas JR Hughes, Gonzalo R Feijóo, Luca Mazzei, and Jean-Baptiste Quincy. The variational multiscale methoda paradigm for computational mechanics. *Computer methods in applied mechanics and engineering*, 166(1-2):3–24, 1998.

[54] O. Iliev, R. Lazarov, and J. Willems. Variational multiscale finite element method for flows in highly porous media. *Multiscale Modeling & Simulation*, 9.4:1350–1372, 2011.

[55] P Jenny, SH Lee, and HA Tchelepi. Multi-scale finite-volume method for elliptic problems in subsurface flow simulation. *Journal of Computational Physics*, 187(1):47–67, 2003.

[56] Hu Jin and George A McMechan. Removing smearing-effect artifacts in angle-domain common-image gathers from reverse time migration. *Geophysics*, 80(3):U13–U24, 2015.

[57] Oksana Korostyshevskaya and Susan E Minkoff. A matrix analysis of operator-based upscaling for the wave equation. *SIAM Journal on Numerical Analysis*, 44(2):586–612, 2006.

[58] Faqi Liu, Guanquan Zhang, Scott A Morton, and Jacques P Leveille. An effective imaging condition for reverse-time migration using wavefield decomposition. *Geophysics*, 76(1):S29–S39, 2011.

[59] Xiao-Qi Liu, Li-Qun Cao, and Qi-Ding Zhu. Multiscale algorithm with high accuracy for the elastic equations in three-dimensional honeycomb structures. *Journal of computational and applied mathematics*, 233(4):905–921, 2009.

[60] Yang Liu. An optimal 5-point scheme for frequency-domain scalar wave equation. *Journal of Applied Geophysics*, 108:19–24, 2014.

[61] Zhao-lun Liu, Peng Song, Jin-shan Li, Jing Li, and Xiao-bo Zhang. An optimized implicit finite-difference scheme for the two-dimensional Helmholtz equation. *Geophysical Journal International*, 202(3):1805–1826, 2015.

[62] GA M cMECHAN. Migration by extrapolation of time-dependent boundary values. *Geophysical Prospecting*, 31(3):413–420, 1983.

[63] Mikko Manninen, Veikko Taivassalo, Sirpa Kallio, et al. On the mixture model for multiphase flow, 1996.

[64] Jens M Melenk and Ivo Babuška. The partition of unity finite element method: basic theory and applications. *Computer methods in applied mechanics and engineering*, 139(1-4):289–314, 1996.

[65] Vitor Nunes and Susan E Minkoff*. Imaging via subgrid upscaling and reverse time migration. In *SEG Technical Program Expanded Abstracts 2014*, pages 4008–4013. Society of Exploration Geophysicists, 2014.

[66] JT Oden and HJ Brauchli. On the calculation of consistent stress distributions in finite element approximations. *International Journal for Numerical Methods in Engineering*, 3(3):317–325, 1971.

[67] Olga Arsen'evna Oleinik, AS Shamaev, and GA Yosifian. *Mathematical problems in elasticity and homogenization*, volume 2. Elsevier, 2009.

[68] Stéphane Operto, Jean Virieux, Alessandra Ribodetti, and John E Anderson. Finite-difference frequency-domain modeling of viscoacoustic wave propagation in 2D tilted transversely isotropic (TTI) media. *Geophysics*, 74(5):T75–T95, 2009.

[69] Houman Owhadi and Lei Zhang. Localized bases for finite-dimensional homogenization approximations with nonseparated scales and high contrast. *Multiscale Modeling & Simulation*, 9(4):1373–1398, 2011.

[70] R-E Plessix. A Helmholtz iterative solver for 3D seismic-imaging problems. *Geophysics*, 72(5):SM185–SM194, 2007.

[71] R Gerhard Pratt, Changsoo Shin, and GJ Hick. Gauss–Newton and full Newton methods in frequency–space seismic waveform inversion. *Geophysical Journal International*, 133(2):341–362, 1998.

[72] Weifeng Qiu, Jiguang Shen, and Ke Shi. An HDG method for linear elasticity with strong symmetric stresses. *arXiv preprint arXiv:1312.1407*, 2013.

[73] Jörg Schröder. A numerical two-scale homogenization scheme: the FE2-method. In *Plasticity and Beyond*, pages 1–64. Springer, 2014.

[74] Xuefeng Shang, Maarten V Hoop, and Robert D Hilst. Beyond receiver functions: Passive source reverse time migration and inverse scattering of converted waves. *Geophysical Research Letters*, 39(15), 2012.

[75] Ido Singer and Eli Turkel. High-order finite difference methods for the Helmholtz equation. *Computer Methods in Applied Mechanics and Engineering*, 163(1-4):343–358, 1998.

[76] Rolf Stenberg. A family of mixed finite elements for the elasticity problem. *Numerische Mathematik*, 53(5):513–538, 1988.

[77] William W Symes. Reverse time migration with optimal checkpointing. *Geophysics*, 72(5):SM213–SM221, 2007.

[78] Tetyana Vdovina, Susan E Minkoff, and Sean ML Griffith. A two–scale solution algorithm for the elastic wave equation. *SIAM Journal on Scientific Computing*, 31(5):3356–3386, 2009.

[79] Tetyana Vdovina, Susan E Minkoff, and Oksana Korostyshevskaya. Operator upscaling for the acoustic wave equation. *Multiscale Modeling & Simulation*, 4(4):1305–1338, 2005.

[80] Pham Chi Vinh and Do Xuan Tung. Homogenized equations of the linear elasticity theory in two-dimensional domains with interfaces highly oscillating between two circles. *Acta mechanica*, 218(3-4):333–348, 2011.

[81] Jean Virieux and Stéphane Operto. An overview of full-waveform inversion in exploration geophysics. *Geophysics*, 74(6):WCC1–WCC26, 2009.

[82] Shen Wang, Maarten V de Hoop, and Jianlin Xia. On 3D modeling of seismic wave propagation via a structured parallel multifrontal direct Helmholtz solver. *Geophysical Prospecting*, 59(5):857–873, 2011.

[83] E Weinan, Bjorn Engquist, Xiantao Li, Weiqing Ren, and Eric Vanden-Eijnden. Heterogeneous multiscale methods: a review. *Commun. Comput. Phys*, 2(3):367–450, 2007.

[84] M.F. Wheeler, T. Wildey, and I. Yotov. A multiscale preconditioner for stochastic mortar mixed finite elements. *Comput. Methods Appl. Mech. Engrg.*, 200(9-12):1251–1262, 2011.

[85] M.F. Wheeler, G. Xue, and I. Yotov. A multiscale mortar multipoint flux mixed finite element method. *ESAIM Math. Model. Numer. Anal.*, 46(4):759–796, 2012.

[86] ND Whitmore. Iterative depth migration by backward time propagation. In *SEG Technical Program Expanded Abstracts 1983*, pages 382–385. Society of Exploration Geophysicists, 1983.

[87] X.H. Wu, Y. Efendiev, and T.Y. Hou. Analysis of upscaling absolute permeability. *Discrete and Continuous Dynamical Systems, Series B.*, 2:158–204, 2002.